博士論文

Spatio-temporal analysis of flooding on global scale using microwave remote sensing

（マイクロ波リモートセンシングを用いた
グローバルな洪水の時空間解析）

李 曦

37-137176

A dissertation submitted in partial fulfillment
of the requirements for the degree of

Doctor of Engineering

Department of Civil Engineering
Graduate School of Engineering
The University of Tokyo
Tokyo, Japan
September, 2016

Spatio-temporal analysis of flooding on global scale using microwave remote sensing

(マイクロ波リモートセンシングを用いた

グローバルな洪水の時空間解析）

Examination Committee

Associate Professor Wataru Takeuchi

Professor Taikan Oki

Professor HiroakiFurumai

Associate Professor Kei Yoshimura

Associate Professor Akiyuki Kawasaki

李 曦

Ph.D thesis submitted to

Department of Civil Engineering, The University of Tokyo

Abstract

（論文の内容の要旨）

Spatio-temporal analysis of flooding on global scale using microwave remote sensing

(マイクロ波リモートセンシングを用いた

グローバルな洪水の時空間解析）

李曦

Global warming combined with human activities has caused flooding to become the most frequent and devastating natural disaster. The total number of floods worldwide has more than tripled over the last 15 years. Moreover, for the issue of global warming, it is documented that the average temperatures worldwide has risen since the end of the 19th century. In order to discuss and learn about flooding issue, at least 30 years of data should be traced back based on scientific view of global warming. Additionally, in order to meet the needs of government and enterprises, making use of large historical database of Land Surface Water Coverage (LSWC) will be a valuable, economical and necessary way to obtain accurate information and estimate flooding. Among different kinds of sensors, AMSR-E, which belongs to passive microwave remote sensing, can provide long time series of daily global coverage data. PALSAR, which belongs to active microwave remote sensing, has high spatial resolution without cloud interruption. They are in trade off relationship.

In order to better understand the flooding from this large historical database, land cover change and precipitation are incorporated and analyzed. Land cover change is known to influence both surface water hydrology and soil properties. Rainfall also

seriously influences open water and soil moisture and thus plays an important role in flooding researches. Making clear the relationship among LSWC, precipitation and land cover change not only for a certain watershed or a single region but also for the global range is of great significance.

The purpose of this study is to conduct more precise calibration of AMSR-E by PALSAR. Secondly, to build nearly 30 years of LSWC database by SSMI, AMSR-E, WindSAT and AMSR2 and to estimate the historical tendency of land surface water coverage of each river basin. Thirdly, to analysis the effects of land cover change and rainfall on the global LSWC during 1987-2015 derived from passive microwave remote sensing.

Firstly, the incidence angle effect to the backscattering for PALSAR ScanSAR mode was investigated. It was found that the change of incidence angle brought backscattering variation in PALSAR ScanSAR images. However, the standard deviation of σ^0 (dB) against incidence angle of ascending and descending scenes in Australia and Colombia were0.36 and 0.56, smaller than 1dB.Within small range of incidence angle, the effect of incidence angle is within the acceptableσ^0 (dB) variation of PALSAR in this study. Then, spatial correspondence was discussed between AMER-E NDFI/NDPI LSWC and PALSAR LSWC. There was a good agreement among them. At the same time, it was also found in AMSR-E image, there is some blur at the edge of inundated area because of the different spatial resolution and mechanism of PALSAR and AMSR-E. By applying the least squares method. It was found that the determination coefficient reached more than 0.8, the exponential regression curve could precisely represent the scatter points and the RMSE of NDFI is smaller than that of NDPI. AMSR-E NDFI showed a better performance than AMSR-E NDPI on land surface water coverage estimation. Using more precise AMSR-E calibration by PALSAR, the availability and potential of AMSR-E LSWC for large scale flooding detection was indicated.

Secondly, taking into account population density of the world, 68 major river basins were delineated continent wise all over the world using HYDRO1k data. LSWC derived from SSMI, AMSR-E, WindSAT, AMSR2 was mapped and cross calibration among them in the alternate process of sensors was conducted for all the 68 river basins by making a linear regression model. Based on 68 calibration equations, the original database was modified so that getting the cross-calibrated LSWC database. By conducting temporal analysis using cross-calibrated database. It was found that the LSWC during the flooding in specific year significantly exceeds the average and the LSWC value of latest 15 years was found greater than the value of latest 30 years. It was indicated a growth trend in LSWC during last 30 years. Finally, the histogram and cumulative distribution function of each pixel was made by integrating nearly 30 years of LSWC database. It was found that from wetland, forest, agriculture, to barren land, with the increase of aridity, the probability with high LSWC in one year decreases. Moreover, cumulative distribution functions (CDF) of all pixels in global area were created to estimate the cumulative distribution of each LSWC value in global scale.

Thirdly, after integrating nearly 30 years of global LSWC daily data, the daily change of water area corresponding to monthly change of precipitation from the year 1981 to 2014 in each river basin was computed and plotted. It was found the surface water area change pattern basically coincided with rainfall pattern, showing a seasonal variation characteristic in each year. What’s more, based on the least squares fitting the annual average change of water area in each river basin was computed which showed an increasing trend. In all 68 basins, most of them showed obvious growth trend. In general, river basins of almost no water area change accounted for only 18%, the small growth trend basin accounted for 34%, the large growth trend basin accounted for 48%.

Moreover, STL time series analysis was carried out to make clear the long-term trend relationship between precipitation and LSWC, it was found that the seasonal trend between each other was very coincide but the long-term trend of them was not identical, LSWC almost presented increasing trend whereas precipitation had no significant trend. In addition, the interactive correlation coefficients of long-term trend between precipitation and LSWC in Mekong river was smaller than 0.6. There is no significant correlation between long-term trend in LSWC and precipitation. Rainfall was indicated not the only factor that brings about the change in LSWC.

In addition, by calculating 4 kinds of land cover change including cropland, forest, urban and water body in each river basin, it was found that the change in urban area was very strong in many river basin, especially in Yangtze basin and Huang he basin in China from 2000 to 2012, changed from 0.08% to 0.83% and from 0.17% to 2.21%. Due to global warming, the Himalayan snowmelt increased year by year, causing water in Brahmaputra river increased significantly. Besides, there was no clear trend feature in forest cover change. In addition, the proportion of cropland increased significantly, especially Ganges basin increased by 40%, grew to nearly 70%. Meanwhile, it was found the cropland presented consistent growth situation along with LSWC. The correlation coefficients between cropland and LSWC change was more than 0.85. It is expected that the widespread expansion of cropland might bring about LSWC increasing.

Finally, by detecting the anomaly of LSWC the potential floods can be detected. Anomaly map of each year was made and the monthly flooding development was extracted during nearly last 30 years in global scale, which showed a great increasing trend on frequency since last 15 years especially in nearly 5 years.

Acknowledgement

My study at the University of Tokyo will soon come to an end and I'd like to express my sincere appreciation to all those who have offered me invaluable help during three years of my PhD study in Japan.

I felt it was a lucky and precious experience for studying in Takeuchi laboratory. I really want to express my deepest gratitude to my supervisor, Associate Professor Wataru Takeuchi for his constant guidance，valuable advice and strong support to finish my PhD study. Under his guidance, I was fortunate to attend many international remote sensing conferences, let me get a really wide range of knowledge about remote sensing and enrich my experience.

I also would like to express my heartfelt gratitude to Professor Taikan Oki, Professor Hiroaki Furumai, Associate Professor Kei Yoshimura and Associate Professor Akiyuki Kawasaki for their time, valuable comments and suggestions to improve my research.

My gratitude also goes to all members in Takeuchi laboratory. All the people in Takeuchi laboratory contributed to an extremely nice laboratory atmosphere, which make me comfortable and enjoyable during three years' study. The precious and brilliant memories will stay in my heart for lifetime. Thanks to my tutor Mr. Hiromi Jonai for helping me a lot in administrative aspects during my first step of life in Japan. Special thanks to Ms. Sod and Ms. Haemi Park, who shared a lot of their stories and experiences during their ph,D life. I am also grateful to Ms. Yoko Yoshimura, the secretary of Takeuchi laboratory, for her friendly support in handling many aspects during the course of my study. Special thanks to Mr. Soni, Mr. Korn and Mr. Prakhar who helped me a lot about processing and analysis method. Thanks to other lab members: Ms. Nakazono, Mr. Naoki Katayama, Mr. Sho Tsunoda, Ms. Tita. Thanks to my friends Ms. Liu, Ms. LU, Mr. Kuwada, Mr. Faizan, Mr. Qi, Mr. Chen, Mr. Zhang who gave me their help and time for helping me overcome difficulties during these three years and special thanks to Japanese idol group ARASHI who gives me a lot of energy. I also express my sincere gratitude to all members not list above. I wish all the best for the bright life for them.

I'm thankful to my host family, Kubota grandfather, for caring me as my family and giving me a lot of chance to enjoy Japan. I am also thankful to FSO, Civil Engineering for giving me support and suggestions to make my life easier in Japan.

I sincerely acknowledge the Ministry of Education, culture, Sports, Science &Technology (MEXT) scholarship for providing the financial assistance for my three years study in Japan.

Finally, I'd like to express my gratitude thanks to my family for their loving considerations and great confidence during my whole course of study.

September 2016
The University of Tokyo

Contents

List of Figure

List of Table

Chapter1. Introduction

1.1 Background

In recent years, climate changes and human activities have influenced the water cycle and caused increasing of natural disasters (Milly et al., 2002; Mori, S., Takeuchi, 2009; Pall et al., 2011). Among all kinds of natural hazards in the worldwide flood is probably most devastating, widespread and frequent. It was not only a threat to human life, but also resulted in enormous economic losses (Singh et al., 2013). According to statistics by WHO, nowadays, the global loss caused by the floods accounted for 40% among all of the natural disasters, the deaths caused by the floods accounted for 55%. And, floods are increasing in number, especially over the last 15 years. The total number of floods globally has more than tripled in the last 15 years (Land Commodities Research, Slayback et al., 2012). Recent decades have brought more heavy summer rainfall events along with increased likelihood of devastating floods. While no single storm or flood can be attributed directly to global warming, changing climate conditions are at least partly responsible for past trends because warmer air can hold more moisture. The most pessimistic global climate projections predict an increase in the frequency of high-impact floods over the coming decades as a result of climate change (Kleinen and Petschel-Held, 2007).

Huang et al., (2012) conducted study about hydrological response to climate warming in the upper feather river watershed which showed hydrologic sensitivity to climate warming includes small changes in annual stream flow and actual evapotranspiration, significant changes in stream flow timing and increased frequency and magnitude in extreme flows. For California at the end of the twenty-first century was projected to experience warming by 1.5–4.5 degrees (Cayan et al., 2008). Das et al., (2013)(Das et al., 2013) analyzed increases in flood magnitudes in California under warming climates. They found by end of century, discharges from the Northern Sierra Nevada with 50-year return periods increase by 30–90% depending on climate model, compared to historical values. Corresponding flood flows from the Southern Sierra increase by 50–100%. Madsen et al., (2014) made review of trend analysis and climate change projections of extreme precipitation and floods in Europe from which we could know that climate projections indicated a general increase in extreme precipitation under a future climate, which was consistent with the observed trends. The review also showed that only few countries have developed guidelines that incorporate a consideration of climate change impacts. Apurv et al., (2015)(Apurv et al., 2015) have discussed impact of climate change on floods in the Brahmaputra basin using CMIP5 decadal predictions and derived the flood behavior in the future based on changes in the characteristics of wet rainfall spells in 2010–2020, which suggested an increase in the number of spells with higher rainfall and longer duration which can lead to increase in peak flood and the total flood volume.

For the issue of global warming, it has documented the rise in average temperatures worldwide since the late 1800s, instrumental temperature records had also shown a robust multi-decadal long-term trend of global warming since the end of the 19th century. NASA Earth Observatory documented the anomaly of temperature kept growing since 1980 (NASA Earth Observatory). It was considered that in order to discuss and learn about flooding change, it should be traced back at least 30 years ago based on scientific view of global warming. Moreover, in order to meet the needs of government for appropriate land use planning and enterprises for business continuity planning (BCP) making use of large historical database and learning from data will be an available, economic and necessary way to master the accurate information and development trend of flooding in the global scale which based on viewpoint of retrieval of historical similar patterns to perform instance-based flood analysis and forecasting.

Schmocker-Fackel and Naef, (2010) carried out analysis about changes in flood frequency in Switzerland since 1850 in order to answer have flood frequencies changed over the last 150 years in Switzerland and is the high frequency observed recently a nation-wide phenomenon. They suggested that since 1900 periods with many floods in northern Switzerland have corresponded to periods with few floods in southern Switzerland and vice versa. The differences also suggested that changes in large-scale atmospheric circulation might be responsible for the fluctuations in flood frequency. Sippel et al. (1998) developed a predictive relationship and reconstruct regional inundation patterns in the floodplain of the Amazon River main stem over the past 94 years of stage records. Hallegatte et al. (2013) provided a quantification of present and future flood losses in the 136 largest coastal cities. They put forward that average global flood losses in 2005 are estimated to be approximately US$6 billion per year, increasing to US$52 billion by 2050 with projected socio-economic change alone. Mallakpour and Villarini (2015) examined the changing nature of flooding from 1962 to 2011 happened in the central United States using observational records of 774 stream gauge stations. They found that these changes in flood hydrology result from changes in both seasonal rainfall and temperature across this region. Gizaw and Gan, (2016) developed RFFA model based on SVR to estimate regional flood frequency for two study areas located in Canada under historical and future climate. Toonen (2015) carried out flood frequency analysis and discussion of non-stationarity of the Lower Rhine flooding regime from 1350 to 2011 by using discharge data, water level measurements and historical records.

Land cover change is known to influence both surface water hydrology and soil hydraulic properties by altering the hydrological characteristics of the land surface and modifying the patterns and rates of water flow (Savary et al., 2009). In addition, rainfall also seriously influences open water and soil moisture and thus plays an important role in flooding researches. Climate change has the potential to intensify the hydrological cycle, leading to more intense precipitation with associated changes in the intensity, frequency and severity of flood (Apurv et al., 2015)(Apurv et al., 2015). Ohana-Levi et al. (2015) had modeled the effects of land cover change on rainfall runoff relationships in a Semiarid, Eastern Mediterranean watershed, which was found a strong relationship between vegetation cover and the runoff volume. Moreover, the land cover changes with most pronounced effects on runoff volumes were related to urbanization and vegetation removal. Panahi et al. (2010) discussed the effect of land use/cover changes on the floods of the Madarsu basin of northeastern Iran, which was found that the discharge rate of 2003 flood was about 10 times larger than that of the 1964 flood, since the direct effect of the land use/cover change from the stable forests and rangelands to the unstable agricultural lands on the both soil moisture retention capacity and run off rate. Ferrazzoli et al. (2010) carried out analysis of the effect of rain and flooding events on AMSR-E Signatures of La Plata Basin, Argentina, which has been found that the amount of the effect and the correlation between variables are dependent on the properties of the areas surrounding the stations. Hydrological response to land cover change and human activities in arid regions using a geographic information system and remote sensing has been discussed by Mahmoud and Alazba (2015) which has been indicated that changes in land cover are predicted to result in an annual increase in irrigated cropland and dramatic decline in forest area in the study area over the next few decades.

1.2 Microwave remote sensing

Microwave remote sensing had been largely used to detect and monitor extreme flooding because of the capability of the microwave signal to penetrate through clouds (Temimi et al., 2007). Large-scale flood patterns can be quickly revealed (Zheng et al., 2008). However, since flood events are dynamic processes, the daily and long time series of data are required. The International charter, which plays an important role in flooding research because of its quick response to flood event only provides basic information and satellite images at a certain time detected by satellite like Landsat, SPOT, SAR etc. as data of Charter Activation. Among different kinds of sensors, passive microwave remote sensing like AMSR-E can provide daily global cover data for its high temporal resolution (Temimi et al., 2007) which has been successfully utilized for flood monitoring and soil moisture estimation (Chakraborty et al., 2011) . A multi-temporal analysis of AMSR-E data for flood and discharge monitoring during the 2008 flood in Iowa was conducted by Temimi et al. (2011), demonstrating the importance passive microwave can play in monitoring flooding and wetness conditions and estimating key hydrological parameters. However, the AMSR-E instrument has been successfully accumulating the data from May 4, 2002 to Oct 4, 2011. AMSR2, which was launched in May 18, 2012 designed to continue the AMSR-E observations (Imaoka et al., 2010). Moreover, SSMI, WindSAT, with the same high temporal resolution like AMSR-E and AMSR2, can be used to connect AMSR-E and AMSR2 in building long-term database for flooding detection. Many studies on passive microwave remote sensing for flooding and soil wetness monitoring in a certain river basin have been carried out. Singh et al. (2013) used microwave passive remote sensing to monitor flooding in Brahmaputra basin, India. The performance of different parameters such as PI, F_{WS} and WL was investigated at different bands of the

AMSR-Echannel. Determination of inundation area in the amazon river floodplain using the SMMR 37CHz Polarization Difference was conducted by Sippel et al. (1994), which was found the seasonal changes in inundation area over a 7-year period determined using line mixing models correlate well with changes in river stage. Temimi et al. (2011) carried out a multi-temporal analysis of AMSR-E data for flood and discharge monitoring during the 2008 flood in Iowa. It is demonstrated that passive microwave can play in monitoring flooding and wetness conditions and estimating key hydrologic parameters. Paloscia et al. (2006) conducted soil moisture estimates from AMSR-E brightness temperatures by using a dual-frequency algorithm. The soil moisture estimated by the algorithm from AMSR-E data and the SMC measured on the ground were in good agreement with each other in two sites, Italy and Iowa. In addition, the effect of rain and flooding events on AMSR-E signatures of La Plata basin, Argentina was done by Ferrazzoli et al. (2010). Chakraborty et al. (2011) used passive microwave signatures to detect and monitor flooding events in the Sundarban Delta. Watts et al. (2012) conducted a study of surface water inundation changes within the Arctic-Boreal Region and concluded that the AMSR-E fractional open water record corresponds strongly with regional wet/dry cycles inferred from basin discharge records. Watts (2012) used satellite microwave remote sensing to contrast surface water inundation changes within the Arctic–Boreal region. Moreover, Njoku et al. (2003), Njoku and Chan (2006) discussed vegetation and surface roughness effects on AMSR-E land observation which was found global signals of time-varying vegetation water content derived from AMSR-E are consistent with time-varying biomass estimates obtained by optical/infrared remote sensing techniques.

Takeuchi and Gonzalez (2009) predicted daily land surface water coverage by blending MODIS and AMSR-E and found that the algorithm accurately predicted daily LSWC of AMSR-E. Moreover, studies on LSWC estimation with

AMSR-E combined with MODIS have already been carried out (Takeuchi, W., Komori, D., Oki, T. and Yasuoka, 2006; Mori, S. and Takeuchi, 2009), however MODIS can be affected by clouds and cannot detect large scale flooding (Evans et al., 2010)(Evans et al., 2010) because it conducts optical remote sensing. PALSAR, an active microwave sensor influenced by incidence angle, surface roughness and electrical conduction, provides high spatial resolution and is suitable to correspond to large scale flooding without cloud interruption (Alexakis et al., 2012 ; Arnesen et al., 2013) can be used to compensate with passive microwave sensor. Anh and Dinh (2008) monitored flooding using ALOS/PALSAR imagery, which had shown the possibility to apply ALOS/PALSAR data for flood mapping and monitoring. An evaluation of the PALSAR backscatter was carried out by Lucas et al. (2010), which was about above ground biomass relationship in Queensland, Australia in order to make clear impacts of surface moisture condition and vegetation structure. It was concluded that PALSAR data acquired when surface moisture and rainfall are minimal allow better estimation of the AGB of woody vegetation and that retrieval algorithms ideally need to consider differences in surface moisture conditions and vegetation structure. Moreover, Mishra et al. (2011) conducted land cover classification of PALSAR images by knowledge based decision tree classifier and supervised classifiers based on SAR observables. Hoan et al. (2013) made tropical forest mapping using a combination of optical and microwave data of ALOS, it was found that when the ALOS/PALSAR masks were used in combination with the ALOS/AVNIR-2 classification, the overall accuracy increased to 88% with higher than 90% accuracy for the main forest classes. Zhang et al. (2014) also used ALOS/PALSAR to map paddy rice in southeast China, which showed a relatively high rice mapping accuracy. Therefore, to overcome the weakness of MODIS, which was commonly used, PALSAR was an outstanding tool to conduct more precise calibration to compensate passive microwave remote sensing for flooding detection. In recent decades, there are few studies on flooding detection on global scale by combing a plurality of passive microwave radiometer using daily long-term historical database and utilized active microwave remote sensing to compensate with passive microwave remote sensing. What's more, most of flooding studies focused on one region or one watershed, there were few studies covering a global range and providing macroscopic understanding and grasp of the development trend of flooding on global scale in a macroscopic view.

1.3 Objective of this study

- To conduct more precise calibration of AMSR-E by PALSAR
- To build nearly 30 years of LSWC database by SSMI, AMSR-E, WindSAT and AMSR2.
- To estimate the probability and trend of land surface water coverage on global scale in order to understand historical tendency of land surface water coverage in each river basin.
- To analysis the effects of land cover change and rainfall on the global LSWC during 1987-2015 derived from passive microwave remote sensing.

The framework was showed in Figure 1.1.

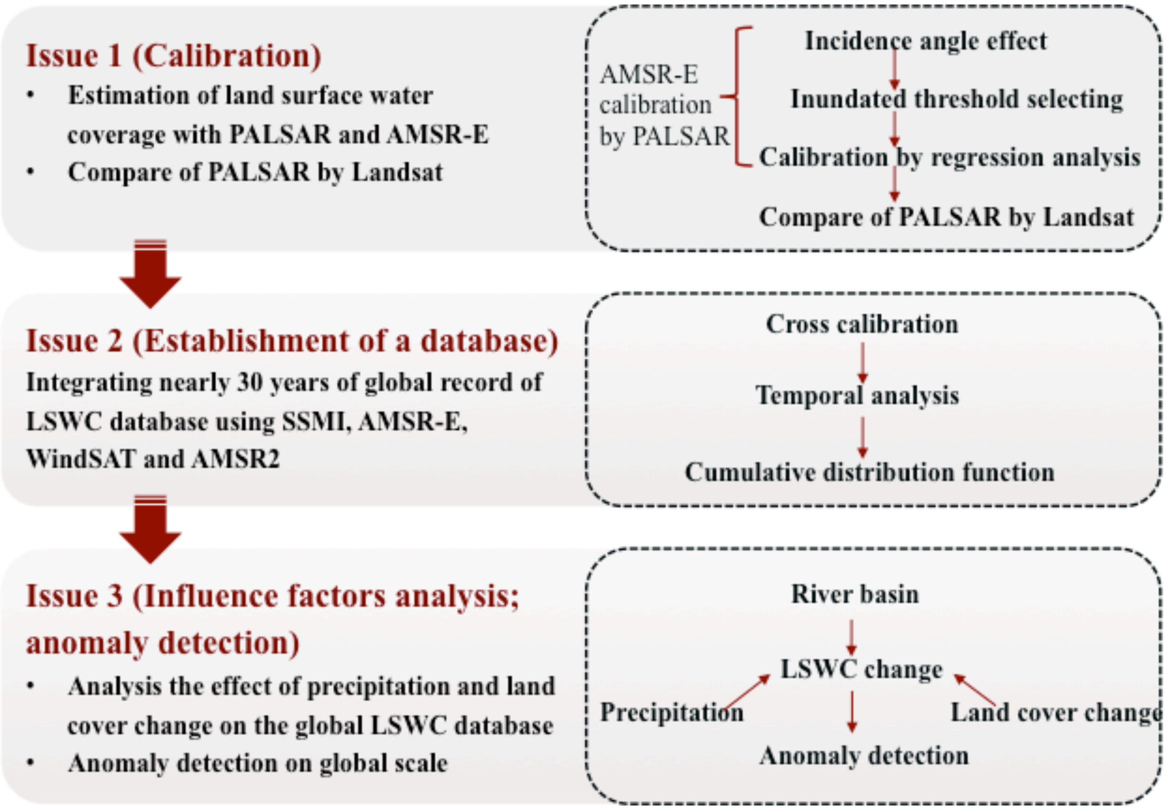

Figure 1.1Framework in this study

1.4 Originality of this study

✧ Making clear of incidence angle effect to the backscattering of PALSAR in this study.

✧ Conducting more precise calibration of AMSR-E with PALSAR by making a function of index NDPI and NDFI with physical quantity-LSWC derived from PALSAR.

✧ Using SSMI, AMSR-E, WindSAT and AMSR2 to create a nearly 30 years of LSWC database and conduct cross calibration of every two sensors in the alternate process of sensors.

✧ Combining river basin dataset, precipitation and land cover change dataset to explore the relationship with water area in each river basin study units on global scale and making trend of global water area map in order to understand historical tendency of land surface water coverage in each river basin.

Chapter2. Flood event detection using AMSR-E data with International charter

2.1 Datasets and methods

2.1.1 Flood events selected from International charter

AMSR-E data, with spatial resolution of 10 kilometers and temporal resolution of 0.5 day were used to map NDFI/NDPI LSWC for flooding detection. 12 flood events happened in worldwide (Figure 2.1) were selected as research object from the International charter. Resource of base map is a global land surface water coverage distribution map derived from AMSR-E. Table 2.1 shows the basic information of them.

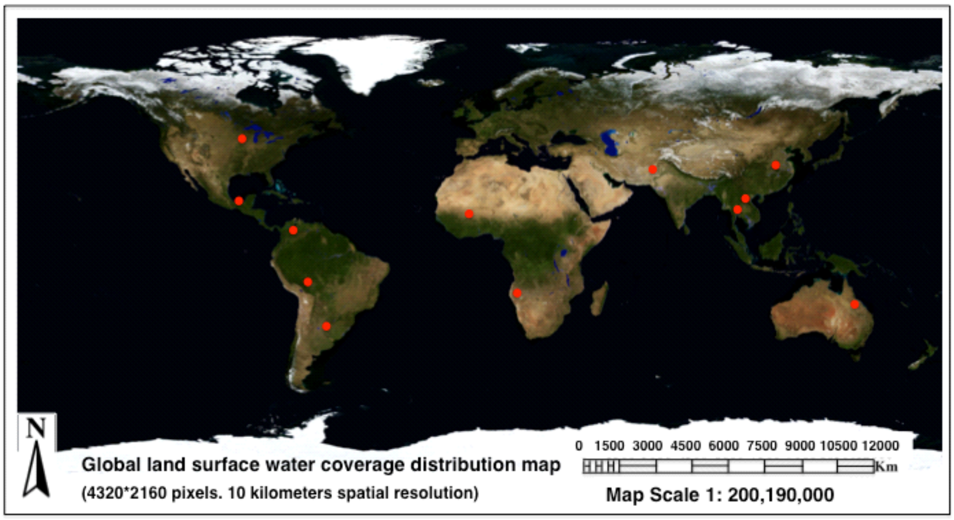

Figure 2.1Distribution of 12 flood events occurred in the worldwide selected from International charter

Table 2.1Basic information of 12 selected flood events

Country	Location of Event	Date of Charter Activation	Representative position	
			Latitude	**Longitude**
Argentina	Santa Fe and Entre Rios provinces	2007-03-30	31.2S	60.6W
China	Anhui province (Huai River basin)	2007-07-13	32.5N	115.8E
Senegal	Kaolack	2007-09-15	16.1N	13.8W
Mexico	Tabasco	2007-11-02	18.2N	92.5W
Bolivia	Moxos, Beni and Marban provinces	2008-01-25	14.6S	65.1W
USA	Iowa	2008-06-12	42.5N	93.2W
Vietnam	North and Central provinces (Red River Delta Region)	2008-11-05	20.9N	105.8E
Pakistan	North West Pakistan	2010-08-02	28.2N	69.4E
Australia	Queensland	2011-01-03	27.3S	151.3E
Namibia	Northern Namibia	2011-04-01	18.2S	15.7E
Colombia	Bolivar province	2011-05-22	8.3N	73.9W
Thailand	Central Thailand	2011-10-17	14.9N	100.3E

2.1.2 Land surface water coverage (LSWC) distribution mapping of AMSR-E

After carrying out a series of pre-processing including radiance calibration, geometric correction and spatial mosaic, AMSR-E daily mosaics are used to compute normalized difference frequent index (NDFI) and normalized difference polarization index (NDPI). When atmospheric transmission is near to 1, we can obtain NDFI, NDPI as follows ((Mori, S., Takeuchi, 2009, Takeuchi and Gonzalez, 2009).

$$NDFI = \frac{TB_{18.7V} - TB_{23.8V}}{TB_{18.7V} + TB_{23.8V}} \quad (3)$$

where $TB_{18.7V}$ and $TB_{23.8V}$ are the brightness temperature of vertical (V) polarization at 18.7GHz and 23.8GHz.

$$\mathrm{NDPI} = \frac{\mathrm{TB_V} - \mathrm{TB_h}}{\mathrm{TB_V} + \mathrm{TB_h}} (4)$$

where $\mathrm{TB_V}$ is the brightness temperature of vertical polarization at 36.5 GHz. $\mathrm{TB_h}$ is the brightness temperature of horizontal polarization at 36.5 GHz.

2.1.3 Anomaly detection

The anomaly was extracted by debugging the absolute and relative errors in two steps using MATLAB. The formula is as follows:

$\mathrm{LSWC_i} – \mathrm{LSWC_{Averagei}} > \mathrm{criteria1}$ (1)

$(\mathrm{LSWC_i} – \mathrm{LSWC_{Averagei}})/\mathrm{LSWC_{Averagei}} > \mathrm{criteria2}$ (2)

where i=1~366

If result satisfied the formula (1), then went into the second step followed the formula (2).

2.1.4 Image similarity calculation

Histogram

A histogram is a graphical representation of the distribution of data. It is an estimate of the probability distribution of a continuous variable. Histograms are used to plot the density of data, and often for density estimation.

In discrete form, on behalf of discrete gray levels by r_k, there is the following formula (Pearson 1895)

$$P_r(r_k) = \frac{n_k}{n} \quad 0 \le r_k \le 1 \;\; k = 0,1,2,\dots l-1 \qquad (2)$$

where: n_k is number of pixels in the image appears as a gray level r_k, n is the total number of image pixels, and n_k/n is the frequency.

Bhattacharyya distance

The Bhattacharyya distance measures the similarity of two discrete or continuous probability distributions. It is often used to determine the relative closeness of the two samples or separability between classes in classification being considered (Bhattacharyya, A. 1943). For histogram similarity calculation, BD obtained the best effect.

For discrete probability distributions p and q over the same domain X, it is defined as:

$$D_B(p,q) = -\ln\big(BC(p,q)\big) \qquad (3)$$

where: $\mathrm{BC}(\mathrm{p},\mathrm{q}) = \sum_{\mathrm{x}\in\mathrm{X}} \sqrt{\mathrm{p}(\mathrm{x})\mathrm{q}(\mathrm{x})}$ (4) is the Bhattacharyya coefficient.

where: $\mathrm{D_B}(\mathrm{p},\mathrm{q})$ is the Bhattacharyya distance between p and q distributions, p,q are two different distributions.

2.2 Flood events detection by AMSR-E

According to the principle that the higher AMSR-E LSWC values will be associated to a relative increase of both water area and soil moisture, I have calculated the LSWC to indicate the water level. I calculated the average of LSWC from 2002 to 2011 in the flood area and did the comparison with the selected specific year by drawing a dotted line figure. Figure 2.3 shows daily changes of LSWC in Anhui province in China (32.5N, 115.8E). The blue line represents the average value of LSWC in 2002-2011. The red line represents the LSWC in 2007. According to the result in 2007, we can find from 0 to 180 days of year LSWC were basically consistent with the average value of LSWC. Besides, LSWC value in 2007 started to increase significantly from 190 days of year, greatly exceeded the average, then decreased significantly after 213 days of year and maintaining a consistent with average value again after.

Figure 2.2 shows monthly changes of LSWC at flood areas in China in 2007. Brighter area indicates high abundance of water coverage at that pixel. We can see that it showed the same trend as the red line in Figure 2.3.With the idea and method above, the same study was conducted for the other flood events, which were selected from International Charter. The daily changes of LSWC were shown as Figure 2.4.

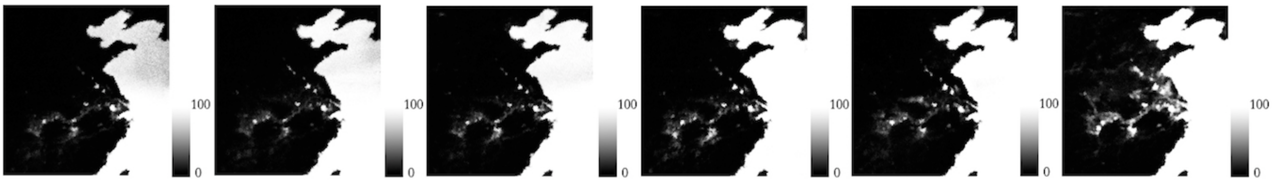

(a) Jan (b) Feb (c) Mar (d) Apr (e) May (f) Jun

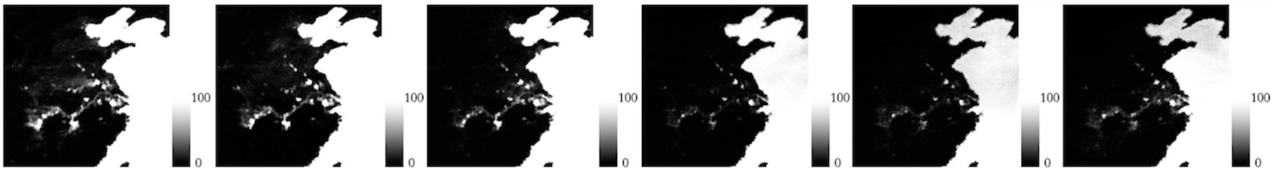

(g) Jul (h) Aug (i) Sep (j) Oct (k) Nov (l) Dec

Figure 2.2 Monthly changes of LSWC in Anhui province in China (32.5N, 115.8E) in 2007. Brighter area indicates high abundance of water coverage at that pixel

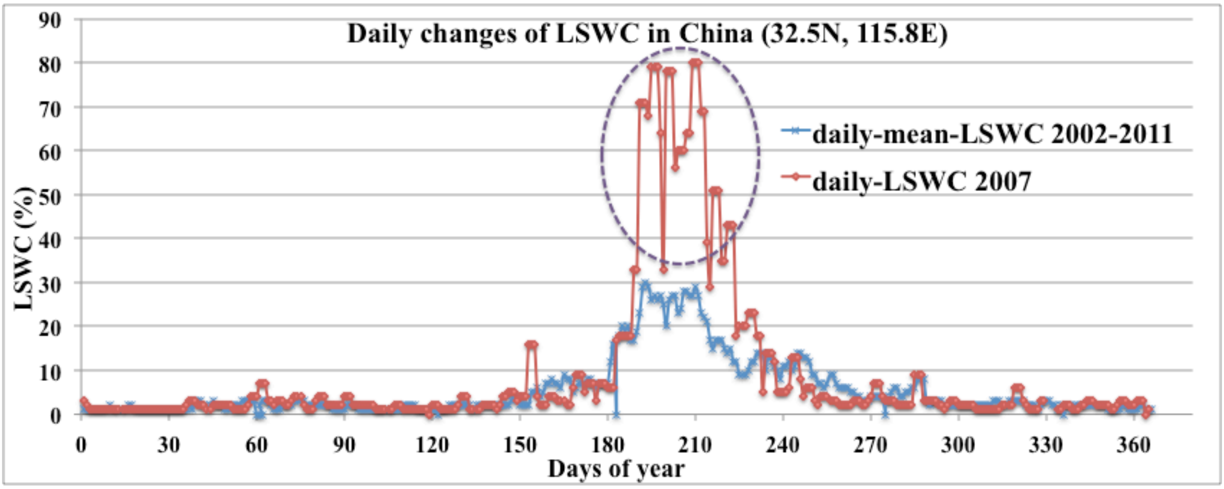

Figure 2.3 Daily changes of LSWC in China (32.5N, 115.8E) in 2007

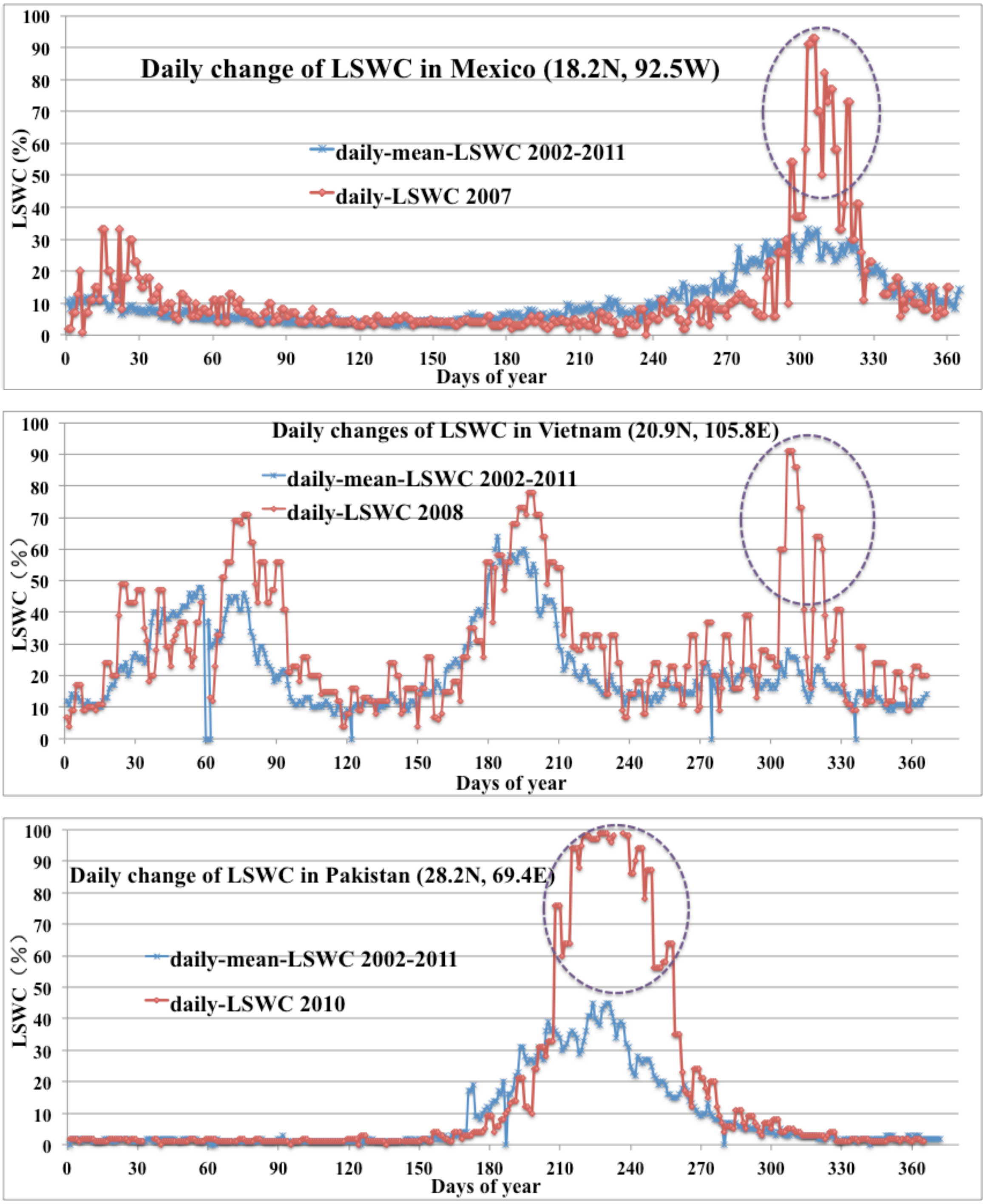

Figure 2.4Comparison of daily changes of mean LSWC with LSWC in certain year

2.3 Anomaly detection compared with International charter

We compared between the anomaly extracted by AMSR-E and actual flood period by International Charter by debugging the absolute and relative error. Table 2.2 shows the anomaly detected under the criterion of the absolute error of 20, the relative error of 100 percent. According to the Table 2.2 we could find that the detected anomalies by debugging basically coincided with the actual period of flooding. Combined with Figure 2.4we can better visually compare the detected anomalies with the actual flood period. The floods in Pakistan as an example for analysis, the anomaly is 210-260 (DOY), which were calculated from the LSWC data, on the other hand, the actual period of flood is around Aug. 19, 2010. It showed a good identity with each other.

Table 2.2 Comparison of the period of real flood events and anomaly detection from AMSR-E

Country	**Actual flood period by International Charter**	**Anomaly extracted by AMSR-E**
China	~2007/07/19~	07/10-07/17,07/19-08/1
Pakistan	~2010/08/19~	07/29-09/17
Vietnam	~2008/11/5~	03/30,07/1,10/26-11/5
Thailand	~2011/09/30~	05/17-06/4,09/17-09/30
Mexico	~2007/11/3~	01/24,10/27-12/6
USA	~2008/06/13~	06/5-06/13
Australia	~2011/01/9~	01/6-01/14,03/18-03/21
Namibia	~2011/04/5~	03/20-05/1
Senegal	~2007/09/18~	08/31-09/23
Bolivia	~2008/02/9~	02/8-05/3
Argentina	~2007/03/30~	03/28-03/31
Colombia	~2011/05/23~	03/29-03/31,04/14-07/5,07/26-07/28

(absolute error: 20%; relative error: 100%)

2.4 Image similarity calculation

In order to visually see the daily change of land surface water coverage, I built a LSWC database of one pixel in Huai River in China and mapped the continuous daily LSWC from 2002 to 2011. Among a total 3330 images, I used images in January in 2007, which belong to dry season and images in July, which belong to rainy season to show the result. The result is showed as Figure 2.5 and Figure 2.6 respectively. In which we could clearly see the big difference of LSWC between dry season and rainy season. Moreover, in addition to the specific water area such as rivers and lakes, the water area expanded significantly in July, the amount of water in rivers and lakes also increased significantly. According to the research results above, there was indeed a flood happening around July 19 in 2007.

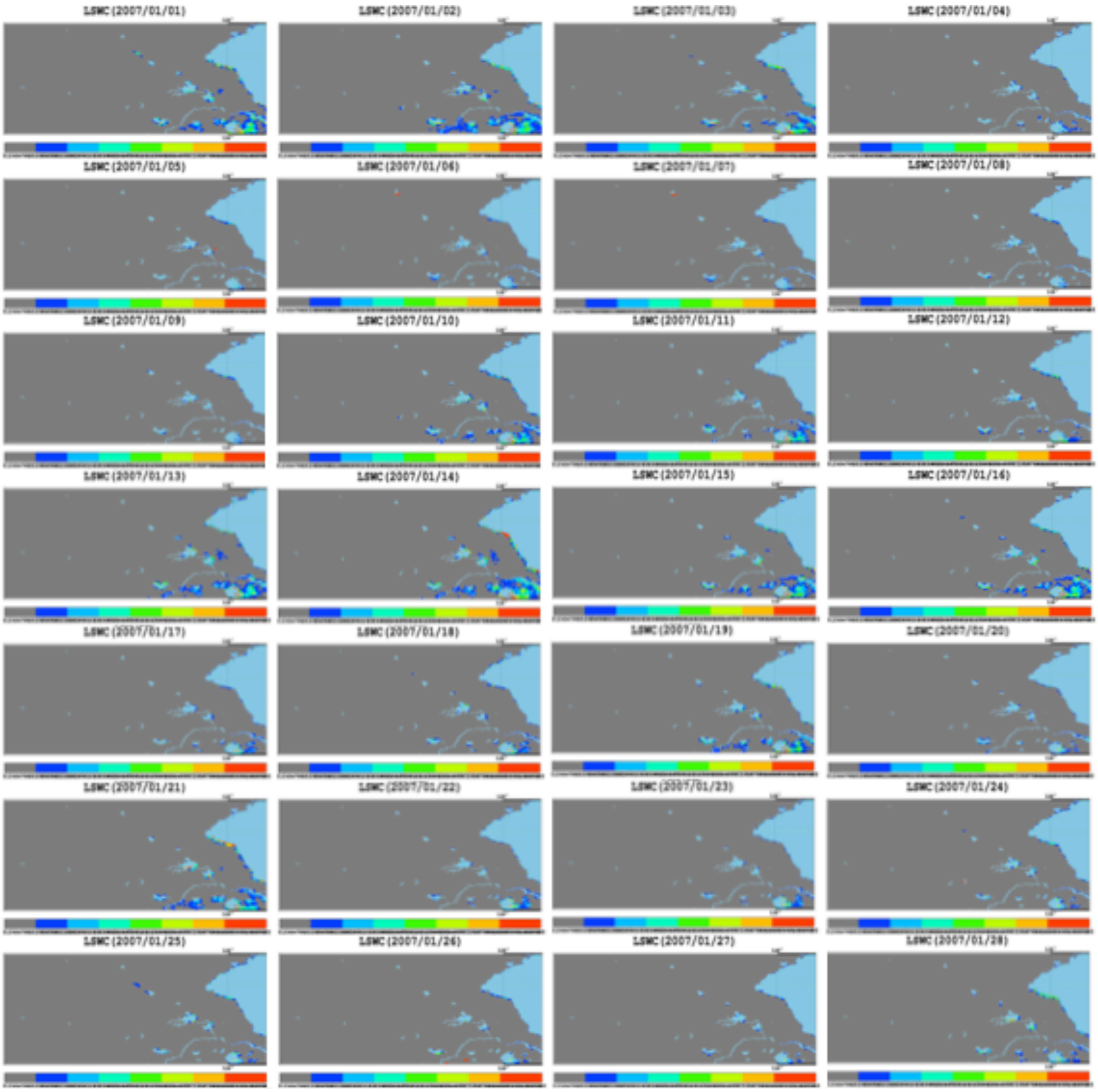

Figure 2.5 Daily LSWC map in Dry season (Jan. 2007) in Huai River Basin

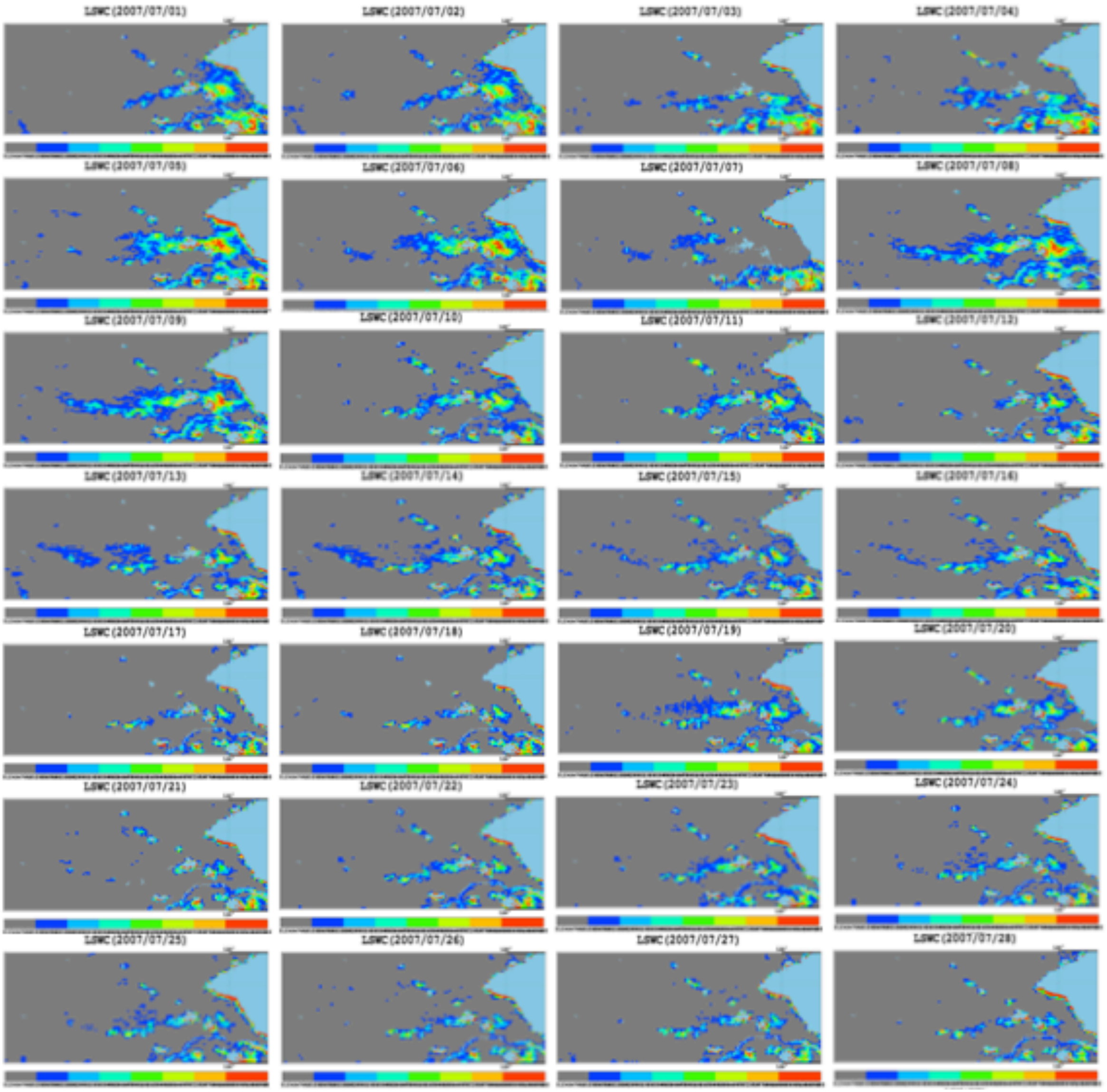

Figure 2.6 Daily LSWC map in Rainy season (Jul. 2007) in Huai River Basin

Firstly, the LSWC image of an objective day in peak of flooding was treat as a reference the other days were threat as a target. After calculating the Bhattacharyya distance between the reference and each target, the value can be ranked out and all the historical images from highest to lowest of LSWC can be lined up. The smaller the distance the better they match.

The flooding happened in Huai river, China in 2007 was used as a case to analysis. The LSWC image in 2007/07/19 was threat as a reference. After calculating the distance between reference and task, we can get the ranking result as Table 2.3 shows. From which we knew that the image of 2003/07/18 was the most similar with the reference, 2007/07/19. We could also see from Figure 2.7, two images were very similar. So we could conclude that the flooding happened around 2007/07/19 might be the same pattern with the flooding happened around 2003/07/18. We could get some useful knowledge and regularities according to the historical information and development of flooding happened in July 2003.

Table 2.3Ranking result of image similarity calculation

Date list	**Similarity**	**Rank**	**Date list**	**Similarity**	**Rank**	**Date list**	**Similarity**	**Rank**
20030718	0.986173	1	20110720	0.980722	11	20050609	0.977885	21
20070716	0.985977	2	20050712	0.980637	12	20100418	0.977743	22
20030715	0.98325	3	20070713	0.980468	13	20030722	0.977543	23
20090616	0.983151	4	20110719	0.980265	14	20100613	0.977541	24
20030717	0.982222	5	20030721	0.979767	15	20090617	0.977408	25
20070715	0.981469	6	20050707	0.979642	16	20050930	0.977162	26
20070710	0.981099	7	20030421	0.979502	17	20060710	0.977039	27
20050711	0.981075	8	20020630	0.978822	18	20070629	0.97702	28
20030720	0.980838	9	20020704	0.978149	19	20090613	0.976988	29
20030331	0.980794	10	20050928	0.977937	20	…	…	…

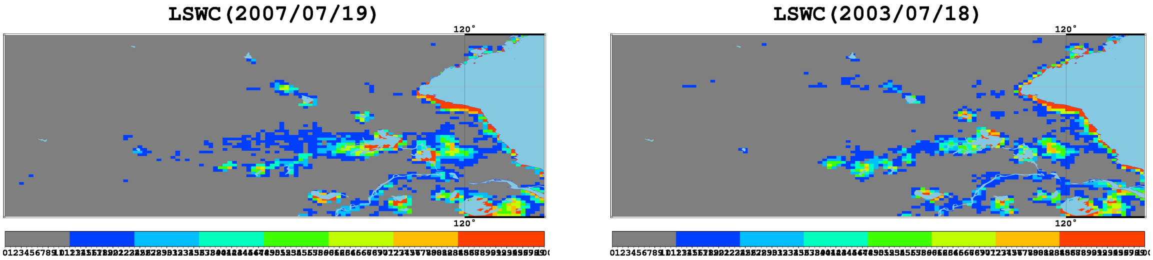

Figure 2.7 Comparison of LSWC map between standard (2007/07/19) and target (2003/07/18) in Huai River Basin

2.5 Discussion and Conclusion

In this part, we demonstrated the potential of AMSR-E for flood detection on global scale. The LSWC was mapped and the daily LSWC database derived from AMSR-E in time series from 2002 to 2011was built. What's more, International charter was utilized as an information platform to get flooding information. The anomaly was extracted which showed a good identity with the actual flood events. Finally, image similarity calculation was proved to be an effective method to dig up regularities and information of flooding from large collection of LSWC images. Therefore, it is indicated the potential and superiority of long-term global LSWC database to make clear the flooding pattern and trend.

Chapter3. Estimation of land surface water coverage with PALSAR and AMSR-E for large scale flooding detection

3.1 Datasets and methods

3.1.1 PALSAR ScanSAR mode data

PALSAR ScanSAR mode data, with a spatial resolution of 100 meters, were used to map LSWC and conduct calibration to AMSR-E. The detailed description of 4 scenes of PALSAR ScanSAR used in this study is showed in

Table 3.2 is detailed description of 4 scenes of PALSAR ScanSAR.

After carrying out Lee filter for the PALSAR ScanSAR image, we calculated backscattering coefficient of digital number as formula (1) shown.

$$\sigma_{1.5}^{0} = 10 \times log_{10}(DN^2) + CF \qquad (1)$$

where: DN: digital number of the amplitude image, CF: calibration factor

Firstly, a vector of an arbitrary polyline in ascending, descending PALSAR scene was created respectively. Then, the incidence angle corresponding to location of each pixel of polyline in the scene was calculated by altitude, observation swath and range of incidence angle of PALSAR. So the spatial profile of polyline with incidence angle against σ0 (dB) was drawn. The technical specification of PALSAR data used in this study was shown in Table 3.1. Finally, only water area was extracted to calculate Min, Max, average and standard deviation of σ0 (dB) corresponding to different incidence angles in order to find the relationship between incidence angle and backscattering.

Table 3.1Technical specification of PALSAR ScanSAR mode

PALSAR	**Mode**	**Polarization**	**Altitude**	**Incident angle**
	ScanSAR	HH	691.65km	18.0 to 43.3 deg.
	Range Resolution	**Recurrent cycle**	**Observation Swath**	**Radiometric accuracy**
	100m	46 days	250 to 350km	1dB (within scene)

Table 3.2 Detailed description of 4 scenes of PALSAR ScanSAR

Location	**Observation data**	**Polarization**	**Orbit**	**Spatial resolution**	**Scene Centre**	
					Latitude	**Longitude**
Mexico	2007/11/03	HH	Descending	100m	18.1N	91.0W
Vietnam	2008/11/05	HH	Descending	100m	20.8N	106.0E
Australia	2011/01/09	HH	Ascending	100m	27.8S	151.6E
Colombia	2011/04/01	HH	Descending	100m	8.2N	74.2W

3.1.2 Otsu's method

Otsu's method can automatically perform clustering-based image thresholding, which is according to viewpoint of minimizing the weighted sum of within-class variances of the foreground and background pixels in order to establish an optimum threshold (Sezgin and Sankur, 2004). Recalling that minimization of within class variances is equal to the maximization of between-class scatter (Liao et al., 2001).

$$\sigma_{\omega}^{2}(t) = \omega_{1}(t)\sigma_{1}^{2}(t) + \omega_{2}(t)\sigma_{2}^{2}(t) \qquad (2)$$

where: Weights ω_i: the probabilities of the two classes separated by a threshold;t: Threshold; σ_i^2: Variances of these classes

In this study, the histogram of backscattering coefficient of each PALSAR ScanSAR scene was built. Each histogram was treated as an input and was put into MATLAB to calculate inundated threshold.

3.1.3 Calibration of AMSR-E with PALSAR by regression analysis

After masking out inundated area of PALSAR image and aggregating image into the same spatial resolution of AMSR-E, which is 10km,some region of interests (ROI) were built and spatial registration for PALSAR and AMSR-E was also conducted. Then, a calibration function of index NDFI, NDPI corresponding to PALSAR LSWC was derived by applying least squares method in MATLAB in order to express the relationship between AMSR-E and PALSAR. It was shown as an exponential function (5).

$$\mathrm{F}(x) = \alpha * exp(b * X) \qquad (5)$$

where: F(x)—PALSAR LSWC; X—NDFI, NDPI

3.1.4 Compare of PALSAR by Landsat

The Landsat L4-5 TM, which has spatial resolution of 30m was used to compare with PALSAR. McFeeters first proposed the Normalized Difference Water Index (NDWI) in 1996 to detect surface waters in wetland environments so that the measurement of surface water extent was allowed (Mcfeeters, 2013). Although the index was created for using with Landsat Multispectral Scanner (MSS) image data, it has been successfully used with other sensor systems in different kinds of applications where the evaluation of extent of open water is needed (Chowdary et al., 2008, EPA 2005, Murray et al., 2012, Panigrahy et al., 2012, USGS 2013). The NDWI is calculated as Equation (6):

$$NDWI = \frac{Band2 - Band4}{Band2 + Band4} (6)$$

where Band 2 is the green light reflectance and Band 4 is the near-infrared (NIR) reflectance

The NDWI product is dimensionless and varies between -1 to +1. Mcfeeters (2013) asserted that values of NDWI greater than zero are assumed to represent water surfaces, whereas values less than, or equal to zero are assumed to be non-water surfaces.

3.2 Incidence angle effects to backscattering of PALSAR

Figure 3.1 shows vector of arbitrary polyline made respectively from ascending and descending PALSAR scene. From which we extracted sections A, B, C of polyline crossed through water areas from scene a and sections A, B, C, D, E from scene b and made spatial profile to show the relationship between incidence angle and σ0 (dB) of each scene as Figure 3.2 and Figure 3.3 shows.

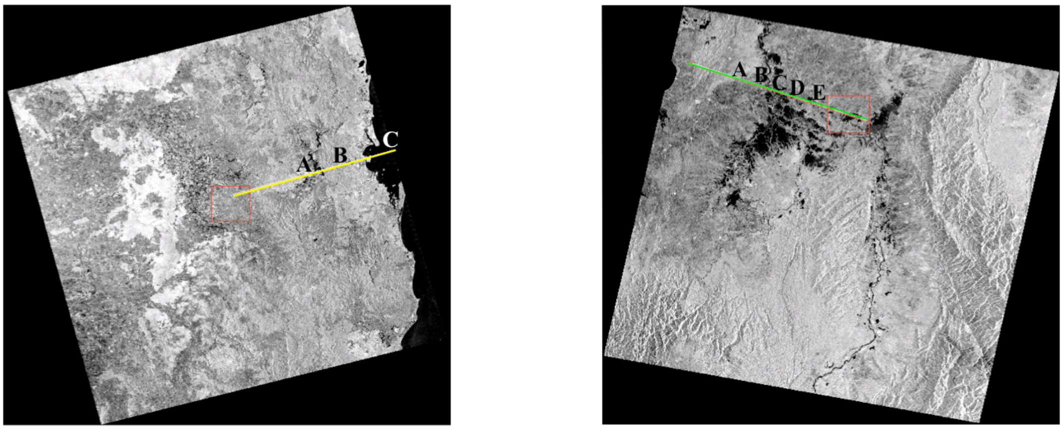

a. Australia (2011/01/09) Ascending

b. Colombia (2011/04/01) Descending

Figure 3.1Arbitrary polyline in two scenes of PALSAR ScanSAR mode

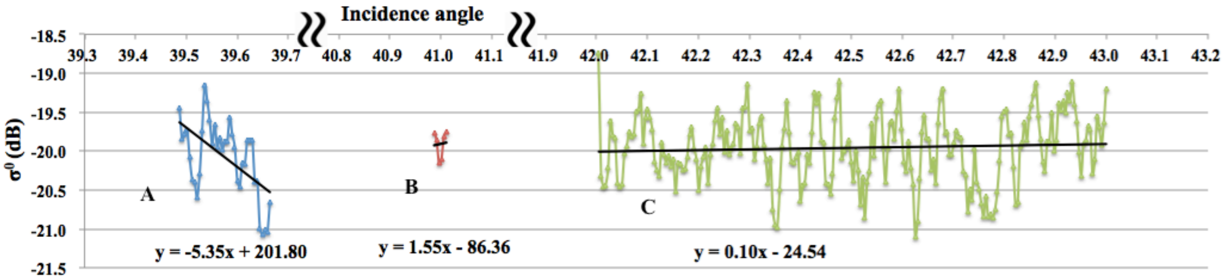

Figure 3.2Spatial profile of extracted section A, B, C of water area in ascending scene in Australia

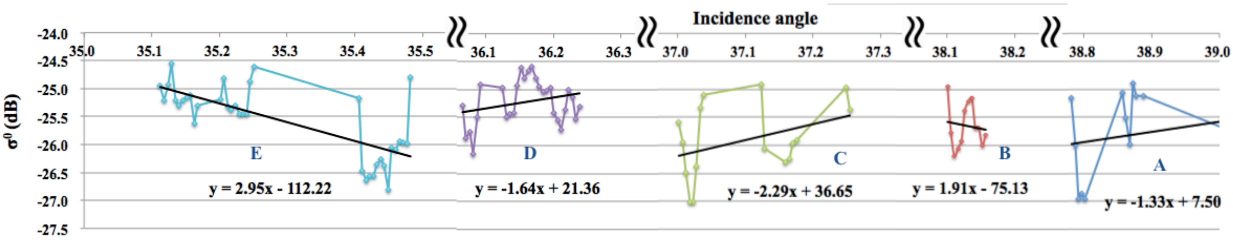

Figure 3.3Spatial profile of extracted section A, B, C, D, E of water area in descending scene in Colombia

From Figure 3.2 and Figure 3.3 it can be seen that the range of incidence angle based on two arbitrary polylines is 4 degree and 5 degree respectively. In each water area, σ0 (dB) presents some variation. However, make a general survey of all water areas in each scene, backscattering shows rather constant along with incidence angle. It presents relative similar behavior in their average sigma and their variability.

Table 3.3 Statistic result of different water area in two senses

	Water area	**Incidence angle(°)**	**σ^0(dB) Max**	**σ^0(dB) Min**	**σ^0(dB) Average**	**Stdev.**
Australia (2011/01/09) Ascending	Area A	39.6	-19.2	-21.1	-20.0	0.48
	Area B	41.0	-19.8	-20.2	-19.9	0.18
	Area C	42.5	-18.7	-21.1	-20.0	0.43
	Average		**-19.2**	**-20.8**	**-20.0**	**0.36**
Colombia	Area A	38.9	-24.9	-27.0	-25.8	0.72

(2011/04/01)	Area B	38.1	-25.0	-26.2	-25.7	0.39
Descending	Area C	37.1	-24.9	-27.0	-25.9	0.66
	Area D	36.2	-24.6	-26.2	-25.2	0.40
	Area E	35.3	-24.6	-26.8	-25.6	0.63
	Average		**-24.8**	**-26.6**	**-25.6**	**0.56**

Table 3.3shows statistic result of different water area in two senses, from the average σ0 (dB) value of water area A, B, C in Australia and water area A, B, C, D, E in Colombia we can see that there is a small difference of only 0.1dB and 0.7dB. According to the average of Max, Min and average σ^0 (dB) it can be seen that variation of sigma values is within plus and minus1dB, the standard deviation of σ^0 (dB) against incidence angle is 0.36 and 0.56, smaller than 1, which means σ^0 (dB) almost centralized to average value. Moreover, by comparing scenes of Australia and Colombia, it has been found that there are some variations in σ^0 (dB) average for the reason that the research area located in different type of land use land cover. There is a large range of agriculture land in research area in Australia, whereas a large range of forest located in research area in Colombia.

However, according to the PALSAR technical specification, we know that radiometric accuracy of PALSAR instrument is less than 1dB within scene (Rosenqvist et al., 2004; PALSAR Reference Guide, 2012; ALOS user handbook) because of restriction of PALSAR instrument itself like filter bandwidth, time delay, inter-beam deviation etc. Based on the result of this study, we can arrive to conclusion that the effect of incidence angle is within the acceptable range of PALSAR.

3.3 Spatial correpondence between AMSR-E NDFI/NDPI LSWC distribution map and PALSAR LSWC distribution map

Spatial correspondence between PALSAR LSWC and AMSR-E NDFI, AMSR-E-NDPI was discussed by comparing LSWC distribution map of them. Figure 3.4 and Figure 3.5 are AMSR-E NDFI/NDPI LSWC distribution map and PALSAR LSWC distribution map in Mexico and Colombia on the same day respectively. Among them, Figure 3.4a and Figure 3.5a are AMSR-E NDFI LSWC distribution map. Figure 3.4b and Figure 3.5b are AMSR-E NDPI LSWC distribution map. Figure 3.4c and Figure 3.5c show PALSAR LSWC distribution map, which have been made by layer stacking with AMSR-E image in order to get the same area and also resized into the same spatial resolution with AMSR-E. Brighter area indicates high abundance of water coverage at that pixel. According to them, a good agreement between AMSR-E NDFI, NDPI and PALSAR LSWC can be seen. LSWC distribution images visually match to each other.

However, on comparison with different scenes, especially in case of Mexico, some spatial variations can be found between PALSAR LSWC and AMSR-E NDFI, NDPI LSWC distribution maps. Combined with Google Earth map we found that the land use and land cover of research area is complicated. As we know, the mechanism of PALSAR is backscattering, whereas the mechanism of AMSR-E is brightness temperature. Although they both belong to microwave remote sensing, the mechanism of them is totally different. There are some affects brought by surface roughness and vegetation on performance of PALSAR. In addition, the incidence angle is an influence factor to backscattering for PALSAR ScanSAR image. Based on our previous research, we found that within small range of incidence angle, the incidence angle effect is within the acceptable $\sigma 0$ (dB) variation of PALSAR, however, in view of whole scene, from

N to F range a constant variation could be seen (Li and Takeuchi, 2015). PALSAR will slightly underestimate inundated area due the influence of surface roughness and vegetation. What's more, because of relative coarse spatial resolution of AMSR-E, some blur will be produced along with coastal line. Besides, as for AMSR-E, the emitted microwave signal is sensitive to both the water and the soil moisture. It is hard to distinguish the wetness and flooding clearly by relative low spatial resolution. The inundated area will be slightly overestimated. Therefore, the calibration of AMSR-E is important.

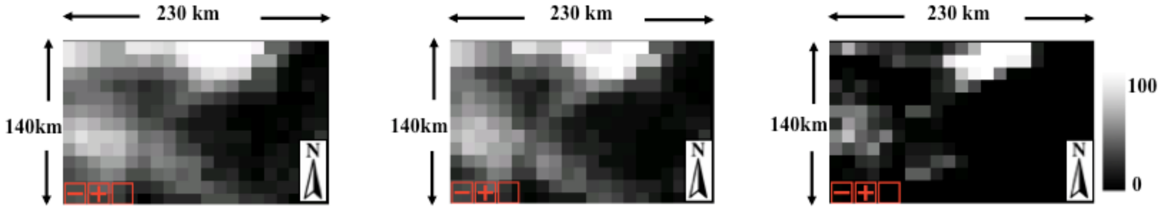

(a)AMSR-E NDFI LSWC (10km resolution)

(b). AMSR-E NDPI LSWC (10km resolution)

(c). PALSAR ScanSAR LSWC (10km resolution)

Figure 3.4 AMSR-E NDFI/NDPI LSWC distribution map and PALSAR LSWC distribution map in Mexico (2007/11/03) Brighter area indicates high abundance of water coverage at that pixel.

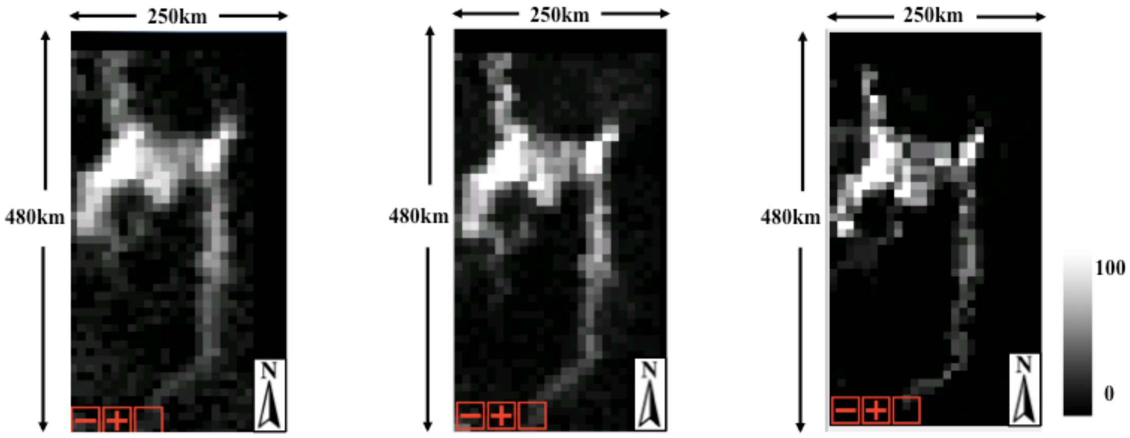

(a) AMSR-E NDFI LSWC (10km resolution)

(b). AMSR-E NDPI LSWC(10km resolution)

(c). PALSAR ScanSAR LSWC (10km resolution)

Figure 3.5 AMSR-E NDFI/NDPI LSWC distribution map and PALSAR LSWC distribution map in Colombia (2011/04/01) Brighter area indicates high abundance of water coverage at that pixel.

3.4 Inundated Threshold selecting

3.4.1 Interval estimation

Interval estimation was conducted to derive threshold based on statistical theory. 10 interest of regions (ROI) of water area were extracted, the mean μ (average) of backscattering (dB) and σ (standard deviation) of each ROI was calculated. Then, μ+σ, μ+2σ, μ+3σ, μ+4σ was calculated in order to mask the water area respectively and select the optimal range combined with image interpretation.

Figure 3.6 is scene of PALSAR ScanSAR HHσ^0 (dB) in Colombia in 2011/04/01. From it, a basin area was chosen and zoomed in as Figure 3.7e shows as a reference scene. Figure 3.7a, b, c, d are overlapped maps of water area in different masking ranges with reference scene. Combined with image interpretation we can clearly see that with the increase in multiples, masked out water area increased. It indicated that the water area was significantly underestimated by masking with μ+σ, μ+2σ, whereas the water area was overestimated by masking with μ+4σ.

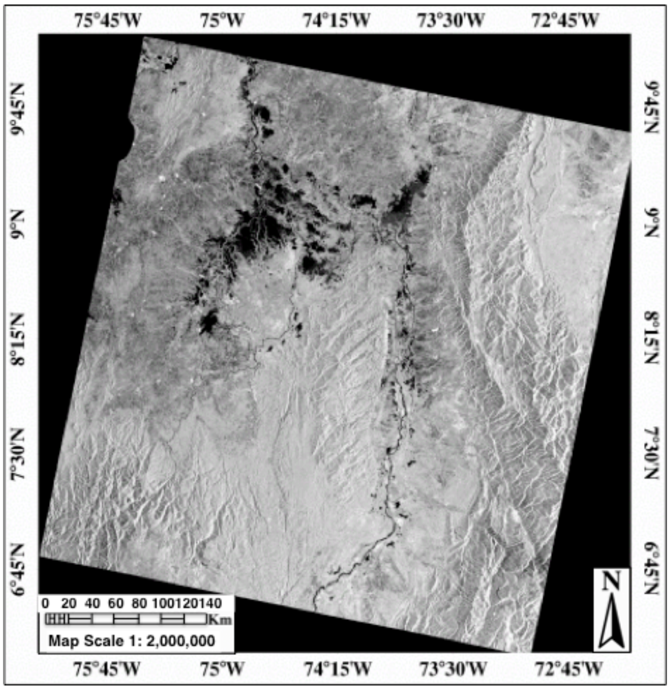

Figure 3.6 PALSAR ScanSAR HH σ0 (dB) scene in Colombia in 2011/04/01

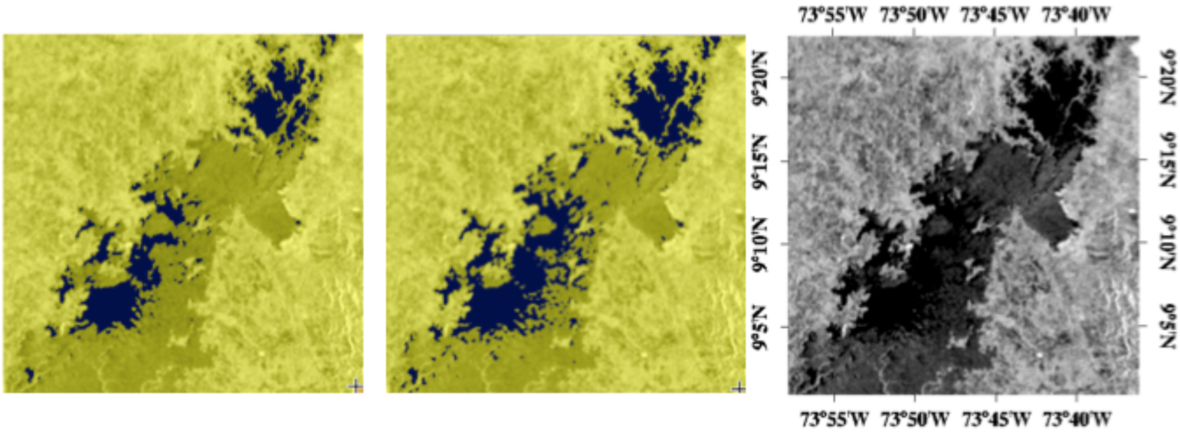

a.μ+σ (dB) b. μ+2σ (dB) e. Reference ScanSAR HH σ^0(dB)

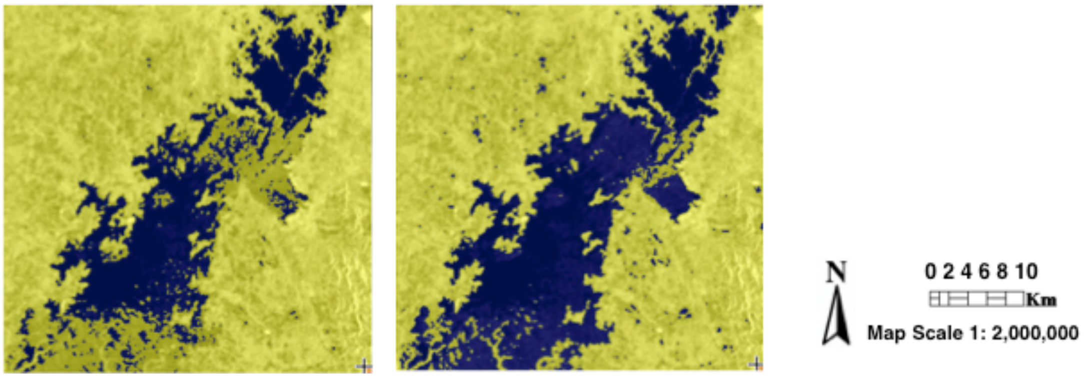

c. μ+3σ (dB) d. μ+4σ (dB)

Figure 3.7 Overlays of water map in different masking ranges with reference ScanSAR HH σ^0 (dB)

What's more, a mountain area was chosen and zoomed in shown as Figure 3.8a to discuss. Figure 3.8b is the water map masking with μ+4σ. On comparison with Figure 3.8c Google Earth image, we can see some valleys were also masked out as water area. Therefore it can be proved that on masking with μ+4σ range, the inundated area was overestimated.

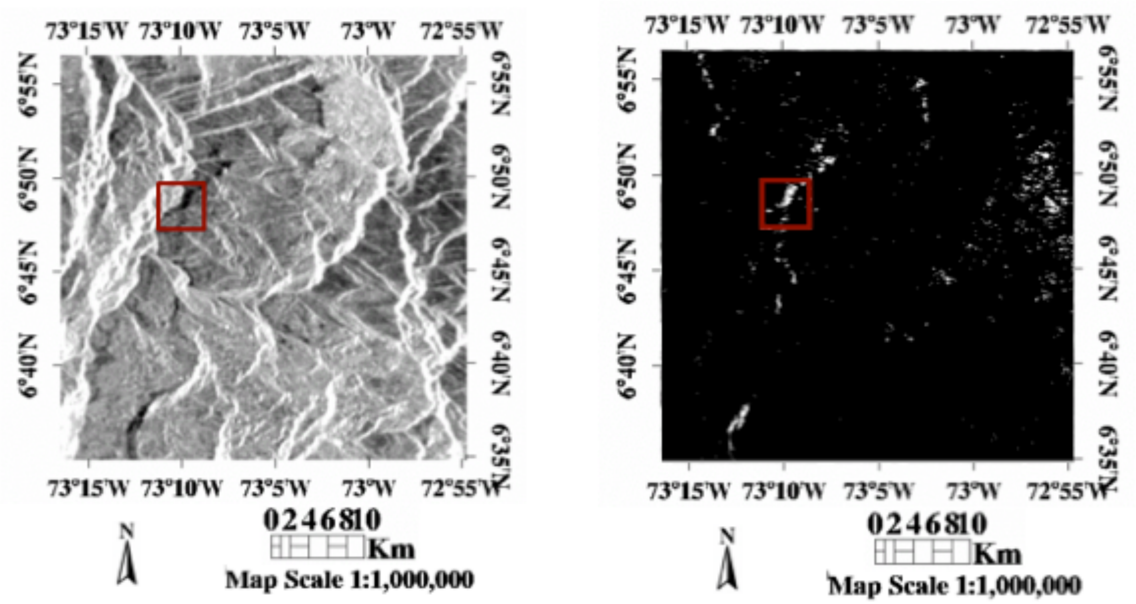

a. PALSAR ScanSAR HH σ^0 (dB)

b. Water area masking with $\mu+4\sigma$

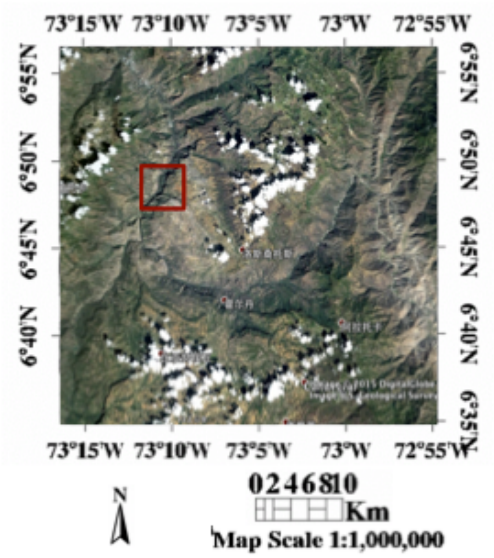

c. Google Earth Map

Figure 3.8Image interpretation of PALSAR scene in mountain area by masking with $\mu+4\sigma$

3.4.2 OTSU's method

In addition, Otsu's method was utilized to obtain inundated threshold based on histogram of backscatter coefficient. Figure 3.9 shows histogram of backscatter coefficient derived from PALSAR ScanSAR HH scenes in Australia and Vietnam.

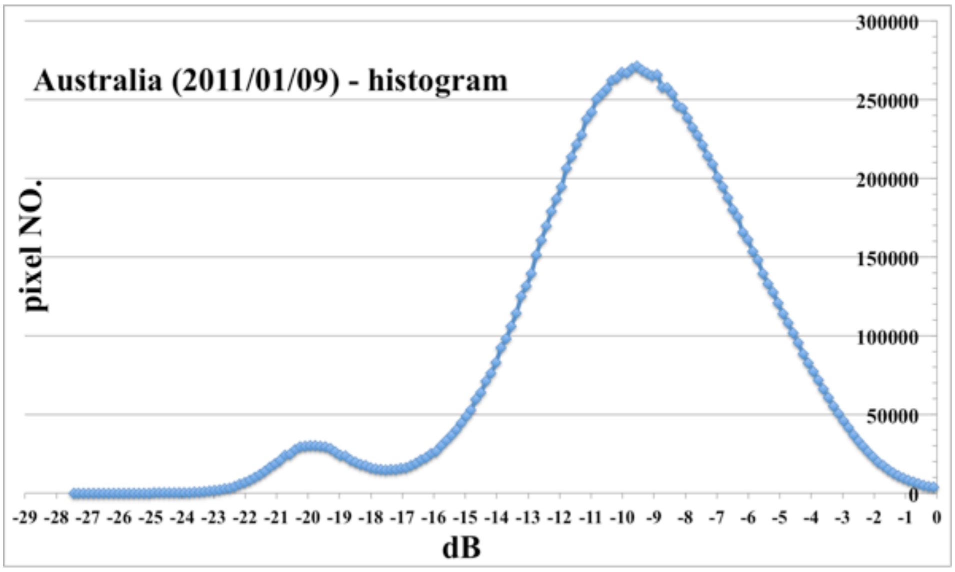

a. Australia (2011/01/09)

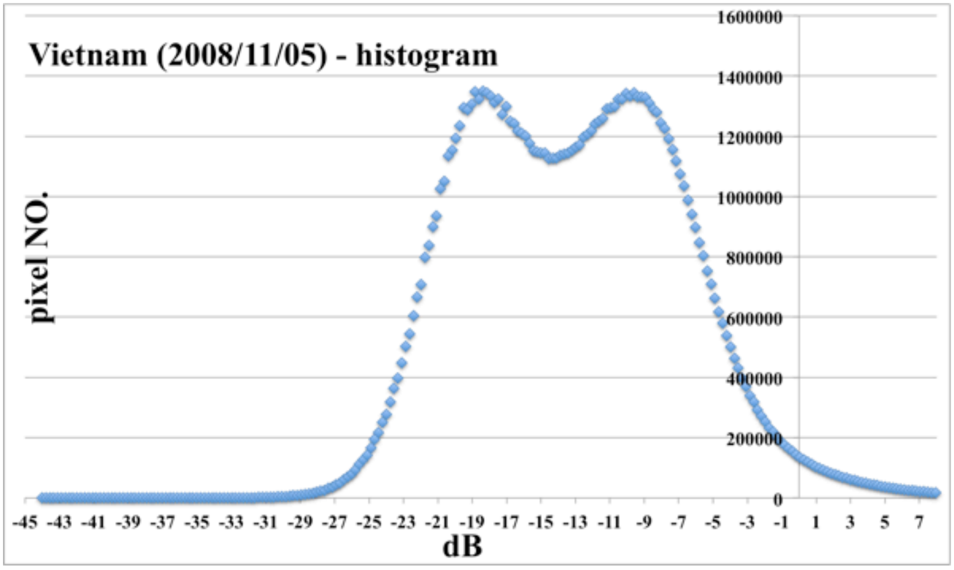

b. Vietnam (2008/11/05)

Figure 3.9 Histogram of backscattering coefficient derived from two PALSAR HH scenes

Table 3.4 Comparison of inundated threshold derived by interval estimation and Otsu's method

	Colombia	**Australia**	**Vietnam**	**Mexico**
$\mu+\sigma$ (dB)	-23.05	-20.10	-20.69	-21.85
$\mu+2\sigma$ (dB)	-21.50	-19.09	-18.32	-20.77
$\mu+3\sigma$ (dB)	-20.12	-18.06	-15.50	-19.69
$\mu+4\sigma$ (dB)	-17.65	-17.00	-13.50	-18.61
Otsu's method (dB)	-21.80	-17.90	-15.45	-19.43

Table 3.4 shows the comparison of inundated threshold derived by the two methods. By comparing dB, we found that the results obtained by interval estimation with μ+3σ and Otsu's method is identical statistically. The difference between μ+3σ and Otsu's is 0.16dB, 0.05dB, 0.26dB in Australia, Vietnam and Mexico, smaller than 0.5dB. However, when the target and the background vary greatly with disparity in size proportion, Otsu's method does not work so well sometimes (Zhang et al., 2011). Therefore we defined HH value with μ+3σ as the inundated threshold in this research.

3.5 Calibration of AMSR-E with PALSAR by regression analysis

3.5.1 Relationship between NDFI/NDPI and PALSAR LSWC

According to the result above, the confidence interval (μ-3σ, μ+3σ) was utilized to mask out inundated area of PALSAR image.

Figure 3.10 and Figure 3.11 shows the scatter plot of two cases in Mexico and Colombia, which represent the relationship between AMSR-E NDFI and PALSAR LSWC, AMSR-E NDPI and PALSAR LSWC. From the figure and Table 3.5, it was found that the exponential regression curve could precisely represent the scatter points and the determination coefficient reached more than 0.8. Both NDFI and NDPI have a good fitting result with PALSAR LSWC.

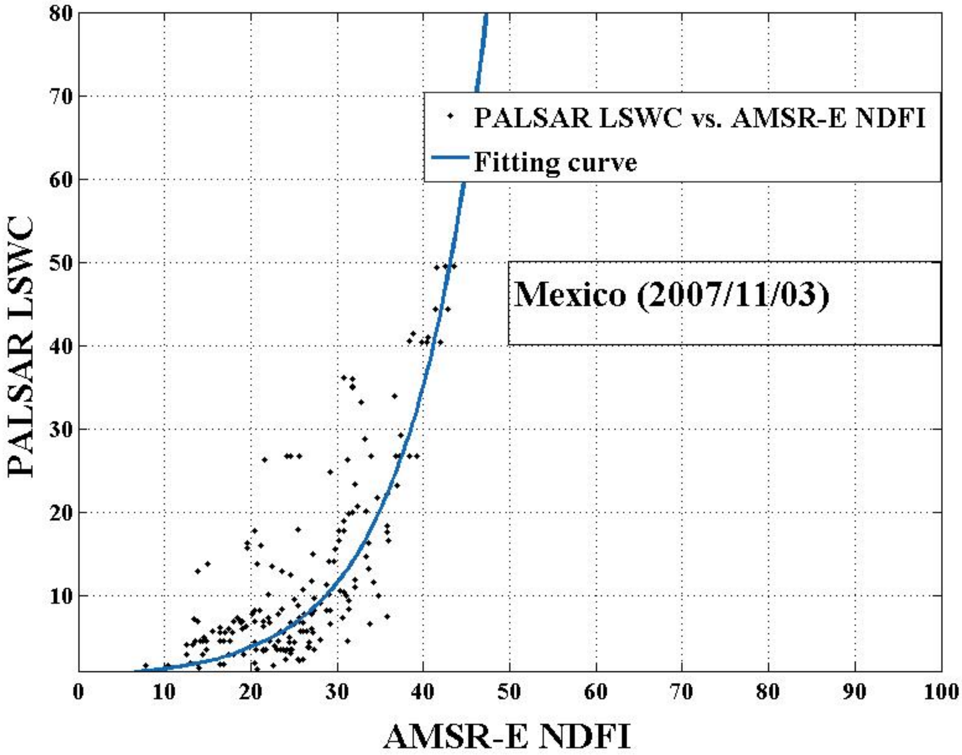

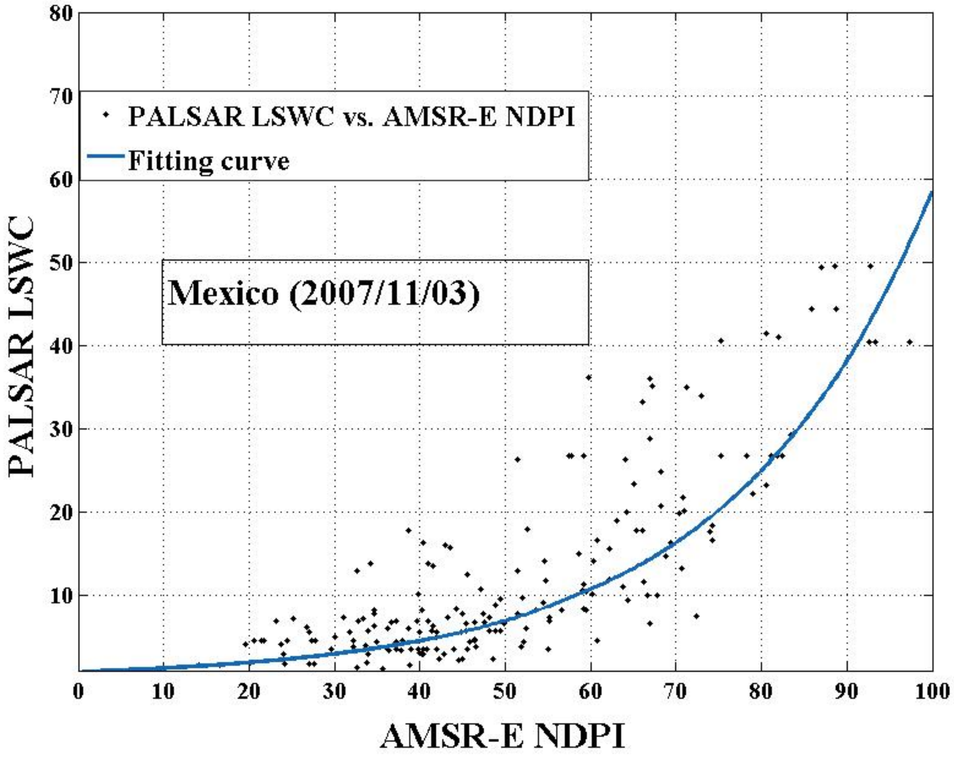

Figure 3.10 Scatter plot representing the relation between AMSR-E NDFI/NDPI and PALSAR LSWC

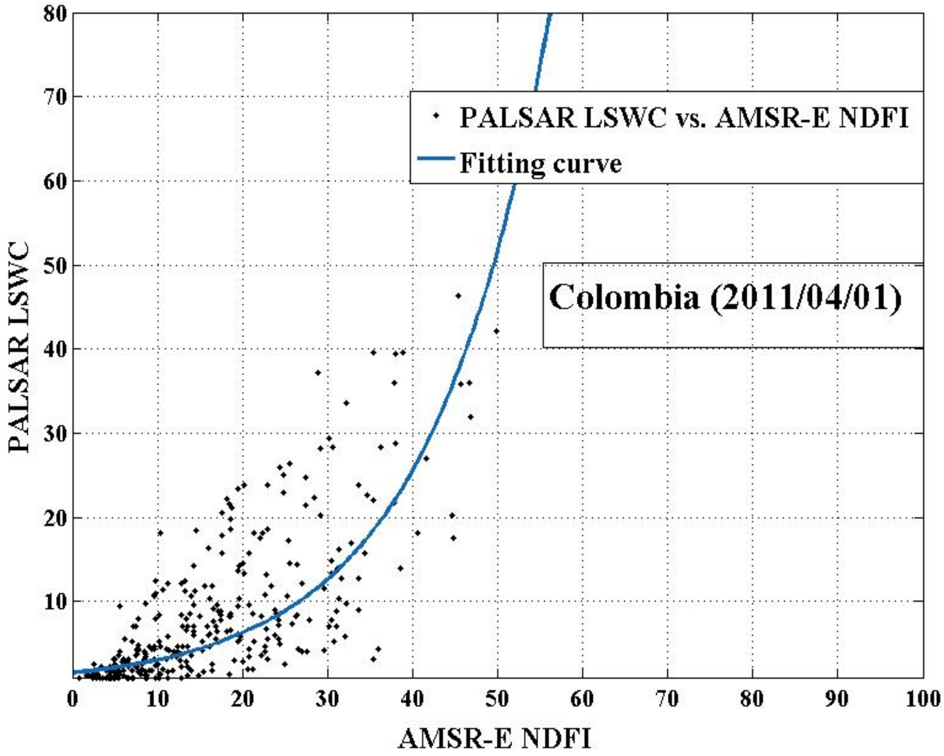

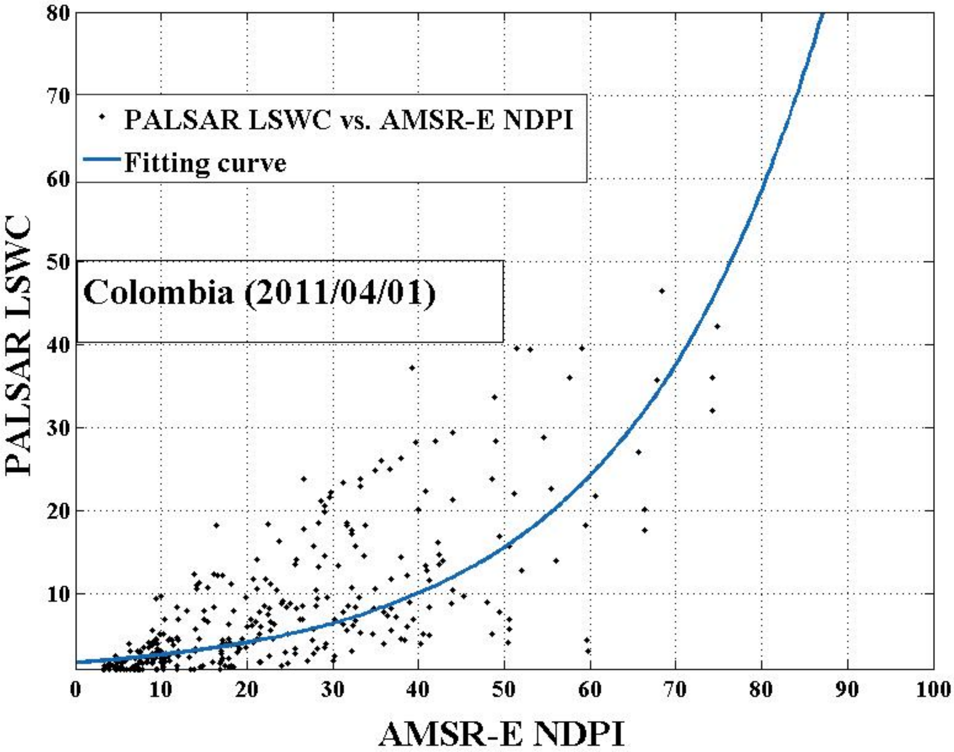

Figure 3.11 Scatter plot representing the relation between AMSR-E NDFI/NDPI and PALSAR

Table 3.5 Results of coefficients a, b and standard deviation

	Mexico (2007/11/03)		**Colombia (2011/04/01)**	
	NDFI-PALSAR	NDPI-PALSAR	NDFI-PALSAR	NDPI-PALSAR
a	1.850	2.137	1.599	2.006
b	0.056	0.025	0.064	0.036
R-square	0.961	0.962	0.897	0.822
RMSE	2.614	2.693	1.987	2.588

＊Coefficients (with 95% confidence bounds)

Furthermore, compared with NDFI and NDPI, we can see that the slope of curve are different, the same PALSAR LSWC corresponds to a bigger value of AMSR-E NDPI. For the reason that NDPI was calculated by brightness temperature with bigger frequency-36.5 GHz, which can lead to a stronger penetration. NDPI was more likely to be affected by surface roughness. What's more, the RMSE of NDFI is smaller than that of NDPI, NDFI showed a better performance than NDPI on land surface water coverage estimation.

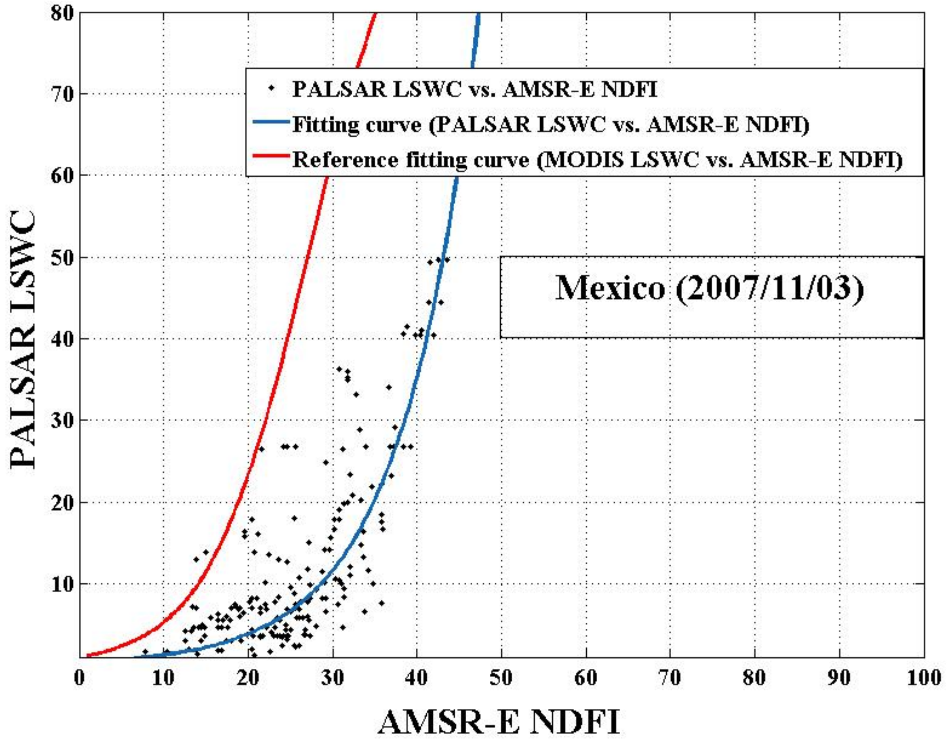

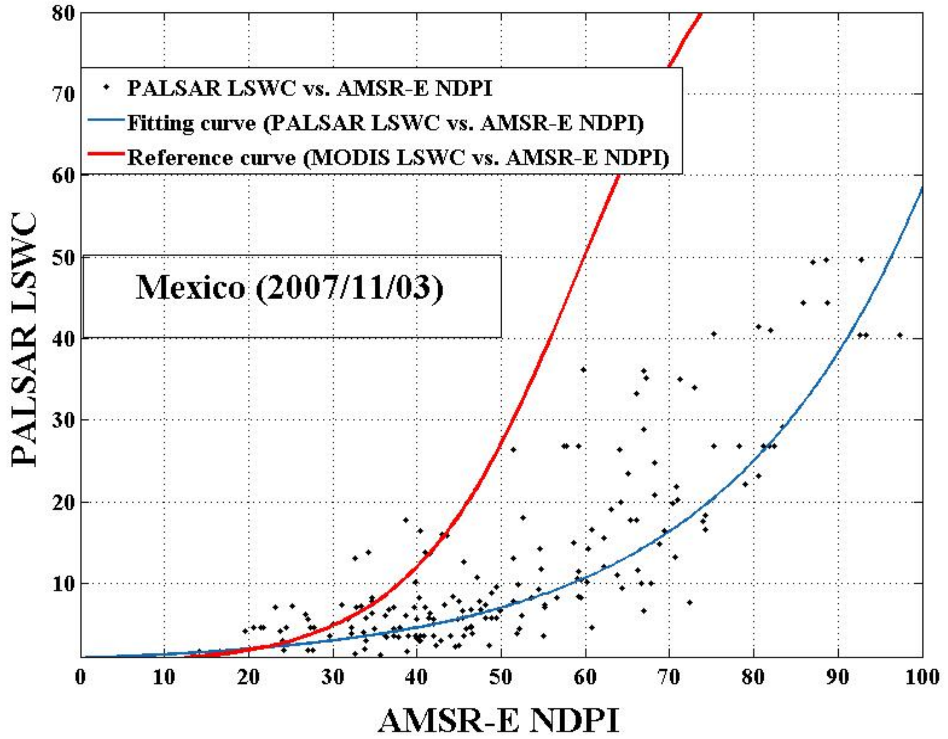

Figure 3.12 Scatter plot representing the relation between AMSR-E NDFI/NDPI and PALSAR

Moreover, Mori et al. estimated LSWC with AMSR-E and MODIS, found the relationship between AMSR-E NDPI and MODIS LSWC (Mori, et al., 2009).

According to the logistic function developed by AMSR-E and MODIS, the regression curve was added as the red line to compare with fitting curve of AMSR-E with PALSAR (Figure 3.12). Based on the result, we can see that in this research, the curve between AMSR-E and PALSAR can better represent scatter rather than the curve between AMSR-E and MODIS.

3.6 Compare of PALSAR with optical remote sensing—Landsat

In order to check the ability of water detection of PALSAR, optical remote sensing – Landsat was used to compare with it. We used the same location, close date of images to compare. Figure 3.13 is comparison of water area derived from PALSAR and Landsat. Figure A shows forest and hill area in Colombia, figure B shows urban area in Vietnam and figure C shows agriculture area in China. Among them, figure c and d are water area extracted from PALSAR and Landsat. Table 3.6 is statistical result of water area derived from different sensors. From the figure 3.13, we can see the water area basically coincided with each other. From the table 3.6, in the three groups the difference of water area is 4%, 1.5% and 4.1% in forest/hill area, urban area and agriculture area respectively, smaller than 5%.

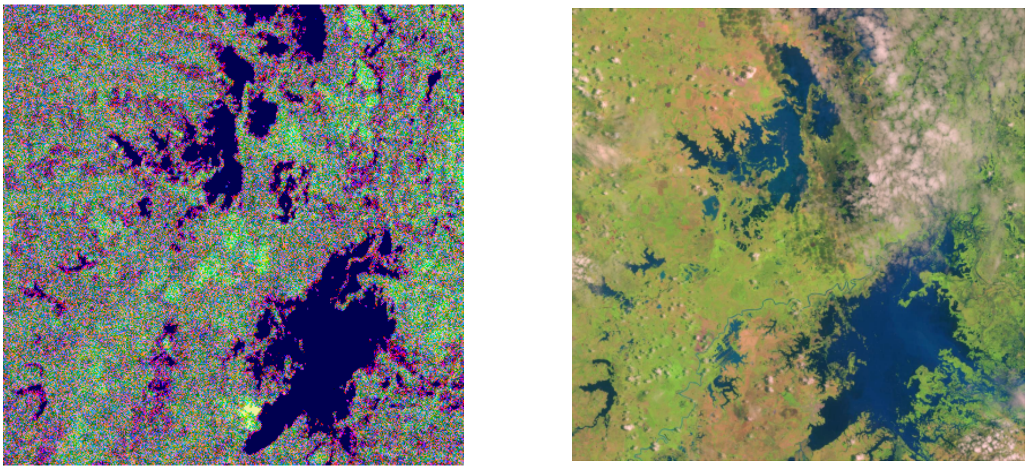

a. PALSAR – 20110401-Colombia-Forest/hill

b. Landsat – 20110406 –Colombia-Forest/hill

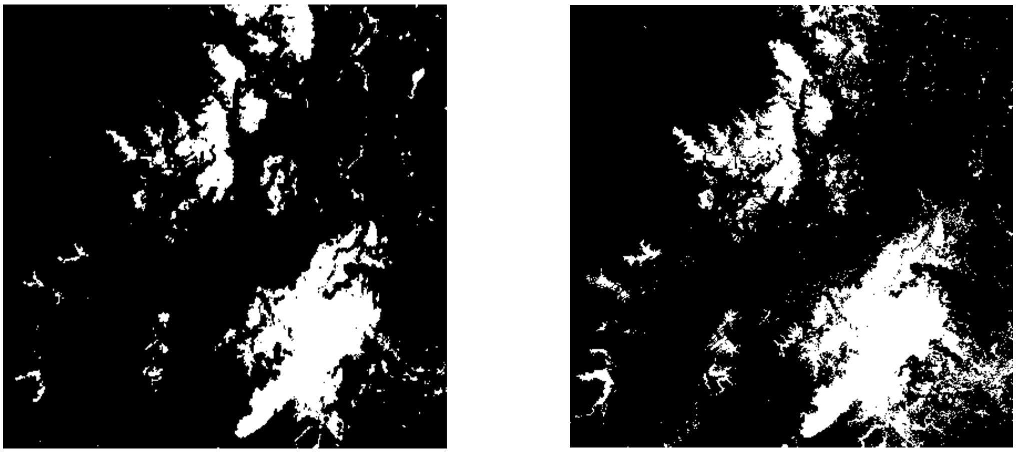

c. PALSAR - Water area -Colombia

d. Landsat - NDWI -Colombia

A. Colombia

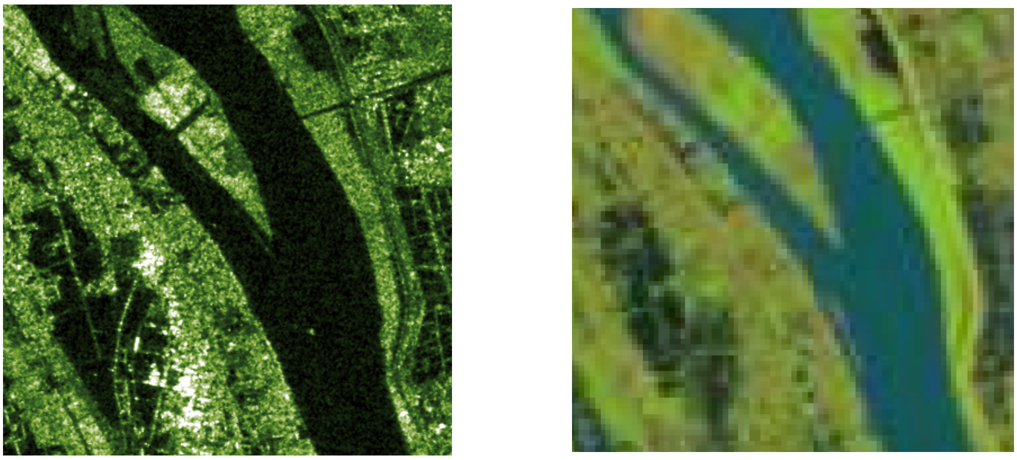

a. PALSAR-20081105-Vietnam-Urban

b. Landsat-20081111-Vietnam-Urban

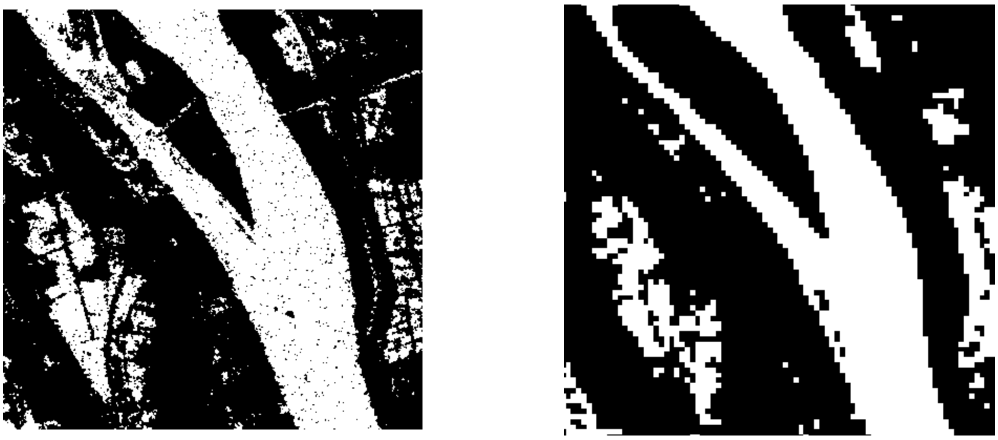

c. PALSAR-Water area -Vietnam

d. Landsat-NDWI -Vietnam

B. Vietnam

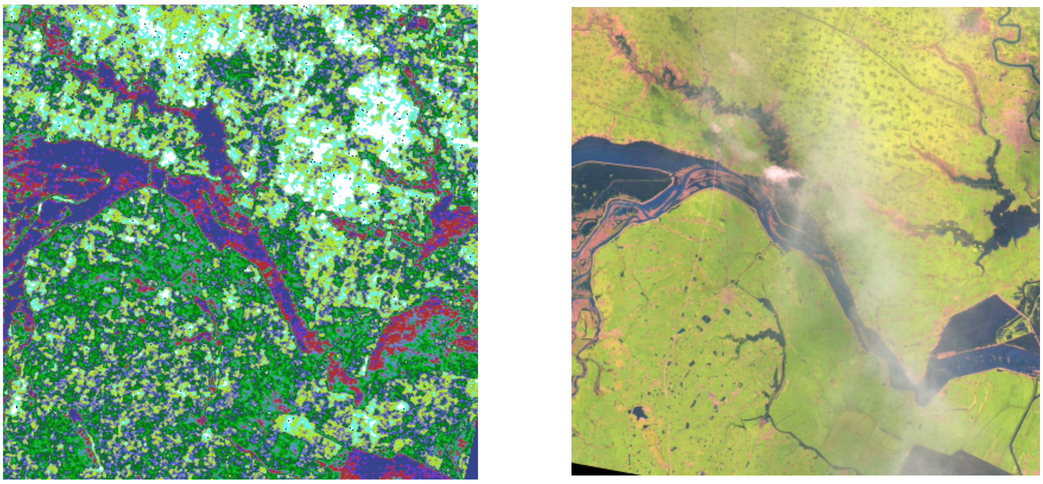

a. PALSAR – 20070719-China-Agriculture b. Landsat – 20070721-China-Agriculture

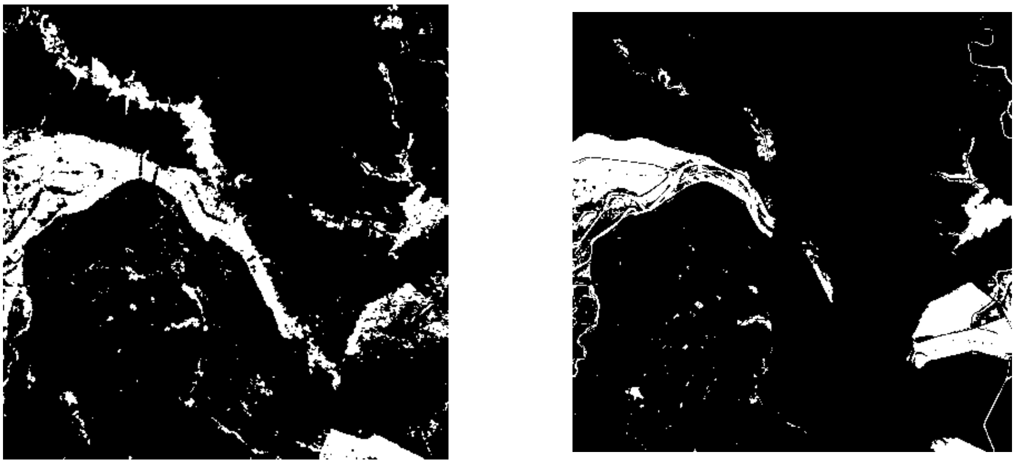

c. PALSAR - Water area -China d. Landsat - NDWI -China

C. China

Figure 3.13 Comparison of water area derived from PALSAR and Landsat

However, there is still some spatial variation between each other. For example, in figure 3.13.C, because of the impact of the cloud, 7.4% water area cannot be detected by Landsat as figure 3.13.C.dshows.Besides, in figure 3.13.A, in high slope hill area, because of terrain condition like shadow and layover, 5.4% water area was failed to detected by PALSAR. Meanwhile, the surface conditions and vegetation also influenced it so that it slightly underestimated inundated area.

Table 3.6statistical result of water area derived from different sensors

	Land cover type	**RS type**	**Water area (%)**	**Omission**	**Commission**
Colombia	Forest/hill	PALSAR	12.8%		
		Landsat	16.8%	1.3%	5.4%
Vietnam	Urban	PALSAR	34.8%		
		Landsat	33.3%	7.4%	3.3%
China	Agriculture	PALSAR	14.1%		
		Landsat	10.0%	5.6%	7.1%

Therefore, both of optical remote sensing and microwave remote sensing have some omission and commission. Selecting the optimal threshold with combination of omission and commission based on different objectives is important.

However, what we focus on in this study is large scale flooding on global scale, most of them are seasonal flooding almost happened in rainy season which always accompanied by cloudy weather. So in this case, it showed the advantage and superiority of microwave remote sensing.

3.7 Discussion and Conclusion

In this part, we found within small range of incidence angle, the effect of incidence angle is within the acceptable σ0 (dB) variation of PALSAR. What's more, we succeeded to select inundated threshold based on interval estimation and Otsu's method and defined HH value with $\mu+3\sigma$ as the inundated threshold in this study. Moreover, the LSWC distribution map of PALSAR was mapped. Finally, the calibration function was established to show a good relationship between NDFI, NDPI of AMSR-E and LSWC derived from PALSAR. Furthermore, we found AMSR-E NDFI showed a better performance than AMSR-E NDPI on land surface water coverage estimation.

Chapter4. Integrating 30 years of global record of LSWC database using SSMI, AMSR-E, WindSAT and AMSR2

4.1 Datasests and methods

4.1.1 Passive microwave radiometers of SSMI, WindSAT and AMSR2

Table 4.1 shows the comparative operating characteristics of each passive microwave radiometers.

Table 4.1 Comparative Operating Characteristics of SSMI, AMSR-E, WindSAT and AMSR2

Passive microwave radiometer	**Frequencies (GHz)**	**Sample Footprint Sizes (km)**	**Temporal resolution**	**Parameter**	**Time period**
SSMI	19.3, 22.3, 36.5, 85.5	37 x 28 (37 GHz) 15 x 13 (85.5 GHz)	Daily	Brightness Temperatures	1987/07/09-Present
AMSR-E	6.9, 10.7, 18.7, 23.8, 36.5, 89.0	74 x 43 (6.9 GHz) 14 x 8 (36.5 GHz) 6 x 4 (89.0 GHz)	Half day	Brightness Temperatures	2002/05/04-2011/10/04
WindSAT	6.8, 10.7, 18.7, 23.8, 37.0	40 x 60 (6.8 GHz) 16 x 27 (18.7 GHz) 8 x 13 (37.0 GHz)	Daily	Brightness Temperatures	2003/01/06-Present
AMSR2	6.9, 10.7, 18.7, 23.8, 36.5, 89.0	62 x 35 (6.9 GHz) 12 x 7 (36.5 GHz) 5 x 3 (89.0 GHz)	Half day	Brightness Temperatures	2012/05/18-Present

4.1.2 River basin delineation using HYDRO1k

HYDRO1k is a geographic database developed to provide consistent and comprehensive global coverage of topographically derived data sets, which provides a standard suite of geo-referenced data sets with a resolution of 1 km. The HYDRO1k data sets are being developed on a continent-by-continent basis, for all landmasses of the globe without Antarctica and Greenland.

Vector river basin data from HYDRO1k was imported into ArcGIS 10.2.2 for processing. After converting the projection from Lambert-Azimuthal Equal Area to Geographic Lat/Lon in WGS84, the first level of basins (main river basin) were highlighted and selected based on the Pfafstetter Coding System (1989). Besides, population density data of the world derived from gridded population of the world (GPW) which provides estimation of population density for the years 2000, 2005, 2010, 2015 based on counts consistent with national censuses and population registers with respect to relative spatial distribution (Tobler et al., 1997, Deichmann et al., 2001). Then, a subdivision for the first level of river basin was carried out in densely populated or river rich areas so that the global major river basin was derived.

4.1.3 Cross calibration among SSMI, AMSR-E, WindSAT and AMSR2 in the alternate process of sensors by linear regression analysis

Each major river basin was treated as research areas. The same river basin respectively from SSMI LSWC map and AMSR-E LSWC map on the same day were exported to compare. Moreover, the same way was used for cross-calibration of AMSR-E LSWC map and WindSAT LSWC map, WindSAT LSWC and AMSR2 LSWC.

Then, a linear regression model was derived to express the relationship as linear function as shown in equation (2).

$$\mathrm{F(x)} = \mathrm{P_1\,X} + \mathrm{P_2} \qquad (2)$$

Where F(x) represent AMSR-E LSWC when X express WindSAT LSWC, whereas F(x) represent SSMI LSWC or WindSAT LSWC when X express AMSR-E LSWC or AMSR2 LSWC. The parameter p_1 express slope of line and p_2 express intercept.

4.1.4 Cumulative distribution function

Firstly, one representative pixel in a region of interest (ROI) was extracted, which the size is 10km multiply by 10km. Then, the number of days corresponding to each LSWC value was calculated by integrating totally all days. Thirdly, after drawing histogram we calculated the probability and cumulative distribution function of representative pixel against LSWC. The cumulative distribution function of a real-valued random variable X is the function given by (Gentle, J.E., 2009)

$$F_X(x) = P\,(X \leq x) \qquad (3)$$

P represents the probability that the random variable X takes on a value less than or equal to x.

The Cumulative distribution function (CDF) of a continuous random variable X can be expressed as the integral of its probability density function f(x) as follows (Daniel, Z. and Stephen, K., 2010):

$$F_X(x) = \int_{-\infty}^{x} f_X(t)dt \qquad (4)$$

t represents an observed value of the test statistic.

Finally, probability and cumulative distribution function of all pixels in global area during last 30 years by programming were calculated. The global cumulative distribution function map set was derived. The simplified diagram of integrating processing was showed in Figure 4.1.

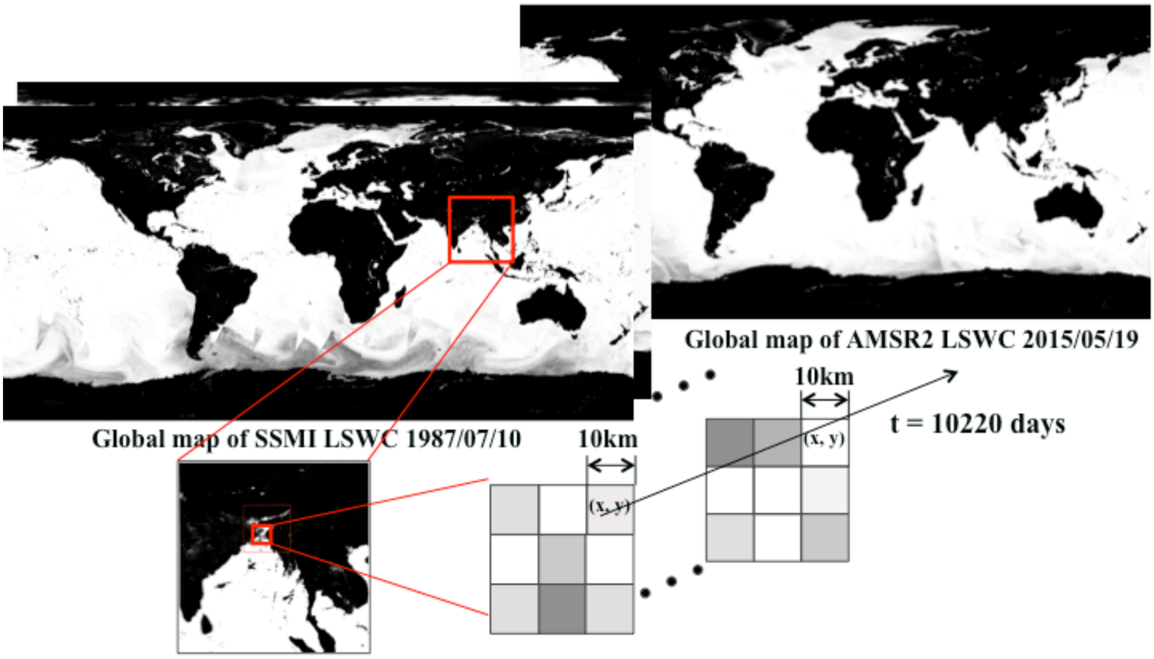

Figure 4.1 Simplified diagram of integrating processing

4.2 Cross calibration among SSMI, AMSR-E, WindSAT, AMSR2

4.2.1 River basin extraction

Global map of gridded population density in 2015 was prepared and the first level river basins (main river basin) all over the world were derived from HYDRO1k data set. Figure 4.2shows the gridded population density of the world in 2015 overlaid by the first level of river basins wherein each pixel value represents persons per square kilometer. It can be seen that the population density in Asia and some area in Europe and Africa is very high, especially that in India, Bangladesh and China is much high.

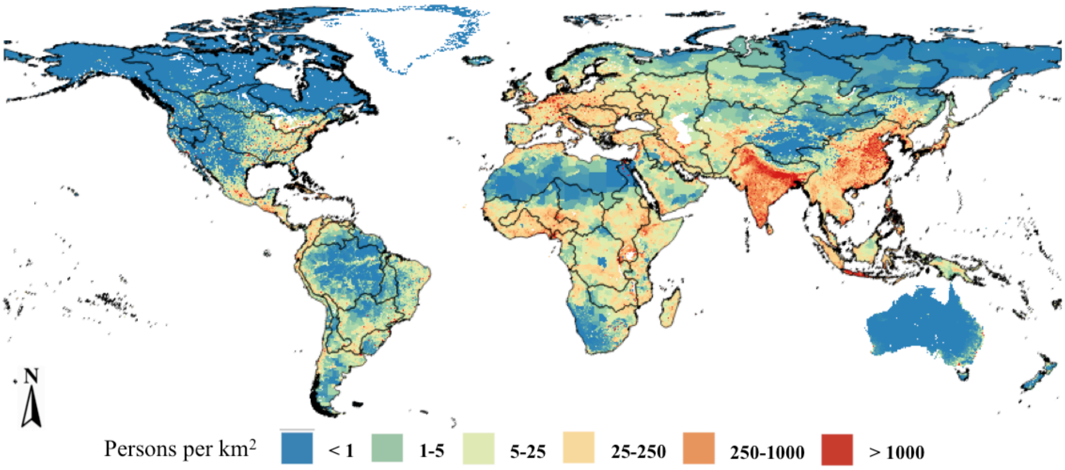

Figure 4.2 Gridded population density of the world in 2015 overlaid by the first level of river basins, the pixel values represent persons per square kilometre.

Since flooding causes more damage in densely populated areas. Therefore, taking into account the river distribution and population density we carried out a subdivision for the first level river basin in densely populated or rich basin area and finally the 68 major river basins in the worldwide with ID as shown in Figure 4.3. Table 4.2 shows the list of several significant major river basins and the corresponding ID of each continent.

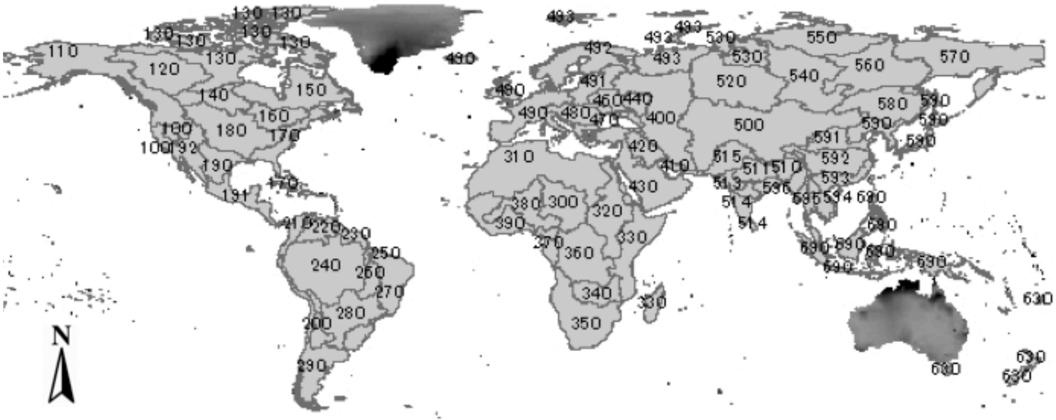

Figure 4.3 68 major river basin with ID of the world derived from HYDRO 1k data set.

Table 4.2 Selected several major river basins and the corresponding ID by continents.

Continent	**ID**	**River basin**	**ID**	**River basin**
North America	100	Great basin	110	Yukon
	120	Mackenzie	140	Saskatchewan/Nelson
	160	St Lawrence	170	East coast
	180	Mississippi	192	Colorado
South America	200	La Puna/Mar Chiquita	220	Orinoco Basin
	230	Atlantic North Coast	240	Amazon Basin
	260	Tocantins Basin	280	La Plata Basin
Africa	300	Lake Chad	350	Orange
	320	Nile	360	Congo
	340	Zambezi	380	Niger
Europe	420	Tigris/Euphrates	440	Don
	450	North Black Sea Coast	460	Dnieper
	480	Danube	492	Sweden/Finland/Scandinavia
Asian	510	Brahmaputra Basin	580	Amur Basin
	511	Ganges	591	Huang He Basin
	515	Indus Basin	592	Yangtze Basin
	520	Ob	594	Mekong Basin
	540	Yenisey	596	Irrawaddy Basin

4.2.2 Spatial correpondence among each passive microwave sensing in the alternate process of sensors

Spatial correspondence between SSMI LSWC and AMSR-E LSWC; AMER-E LSWC and WindSAT LSWC; WindSAT LSWC and AMSR2 LSWC had also been discussed. We mapped the SSMI LSWC, AMSR-E, WindSAT, AMSR2 LSWC distribution map. Brighter area indicates high abundance of water coverage at that pixel. Some river basins were chosen to show. From Figure 4.4, Figure 4.5, Figure 4.6, we can see a high correspondence among four passive microwave radiometers in each compared area. Images basically match to each other. Moreover, in the LSWC map of SSMI and WindSAT, the edge of water area shows some blur. For the reason that the spatial resolution of SSMI and WindSAT radiometer is less than 10km, after we resized it to the same spatial resolution of AMSR-E, it cannot clearly tell the difference with relative coarse spatial resolution. Therefore, the calibration between each sensor in the alternate process is necessary.

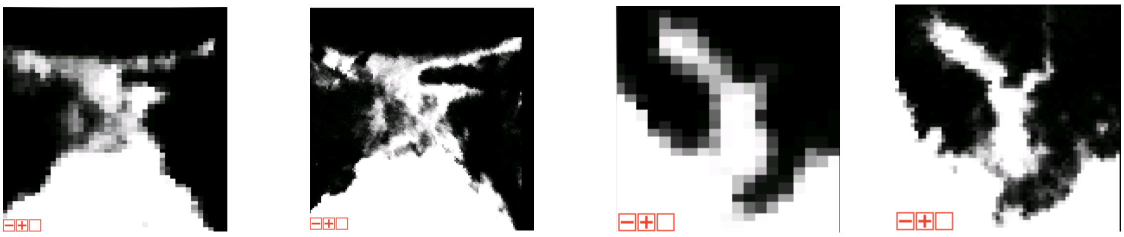

SSMI LSWC AMSR-E LSWC SSMI LSWC AMSR-E LSWC

a. Ganges delta (2002/07/27) b. Mekong delta (2002/08/24)

Figure 4.4 Spatial correspondence between SSMI LSWC distribution map and AMSR-E LSWC distribution map in different areas on the same day, brighter area indicates high abundance of water coverage at that pixel.

Windsat LSWC AMSR-E LSWC Windsat LSWC AMSR-E LSWC

a. Ganges delta (2011/10/01) b. Mekong delta (2011/10/01)

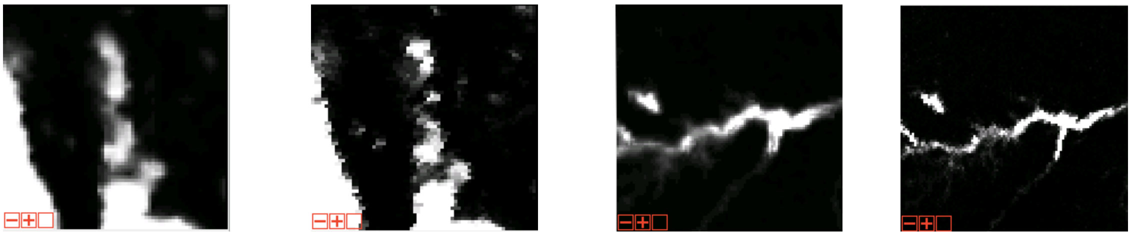

Windsat LSWC AMSR-E LSWC Windsat LSWC AMSR-E LSWC

c. Chao Phraya River basin, Tailand (2011/10/01) d. Amazon basin (2011/10/01)

Figure 4.5 Spatial correspondence between AMSR-E LSWC distribution map and WindSAT LSWC distribution map in different areas on the same day, brighter area indicates high abundance of water coverage at that pixel.

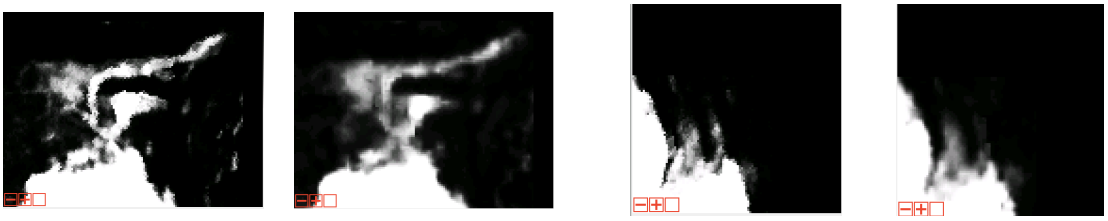

AMSR2 LSWC Windsat LSWC AMSR2 LSWC Windsat LSWC

a. Ganges delta (2012/07/03) b. Irrawaddy River, Myanma (2012/07/03)

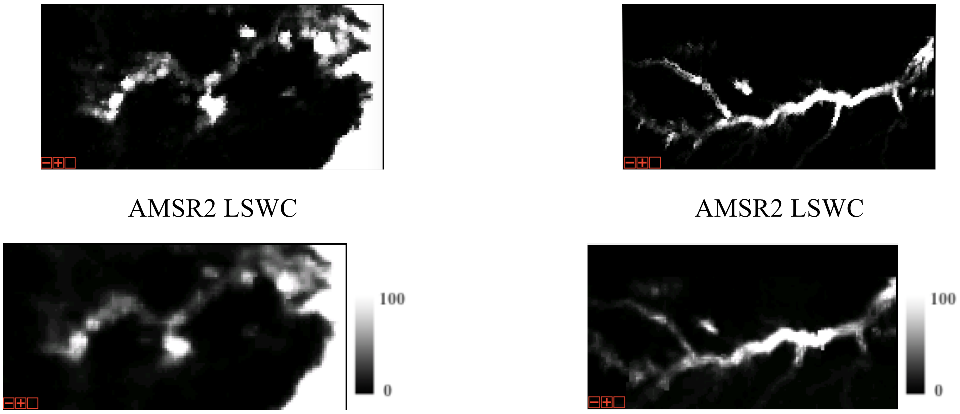

AMSR2 LSWC AMSR2 LSWC

Windsat LSWC Windsat LSWC

c. Huai river basin, China (2012/07/03) d. Amazon basin (2012/07/03)

Figure 4.6 Spatial correspondence between WindSAT LSWC distribution map and AMSR2 LSWC distribution map in different areas on the same day, brighter area indicates high abundance of water coverage at that pixel.

4.2.3 Calibration among SSMI, AMSR-E, WindSAT and AMSR2 LSWC for all the river basin

Cross calibration was conducted for all the 68 river basins. The regression function and scatter plot was made. Figure 4.7, Figure 4.8and Figure 4.9show scatter plots of different river basins on the same day which representing the relationship between SSMI LSWC and AMSR-E LSWC, AMSR-E LSWC and Windsat LSWC, Windsat LSWC and AMSR2 LSWC. The X axis represents AMSR-E LSWC, Y axis represent WindSAT LSWC and scatter is value of each pixel. We can see that in each case, scatter plots present a linear distribution. Moreover, from scatter plot, we can see the regression line of some basins tend to be one to one line, but in some river basin the slope of regression line is small. So the cross calibration river basin by river basin is necessary.

Figure 4.10 is cross calibration line of SSMI with AMSR-E for all the river basins. It can be seen that there are some variance between line and line. Table 4.3shows all the regression equation and evaluation parameters of SSMI with AMSR-E for each river basin. With the same way, we got calibration functions for all the river basins between AMSR-E and WindSAT, WindSAT and AMSR2 shown as Figure 4.11.Based on these equations, we modified the original database and finally got a cross calibrated LSWC database in time series from 1978 to 2015 successfully.

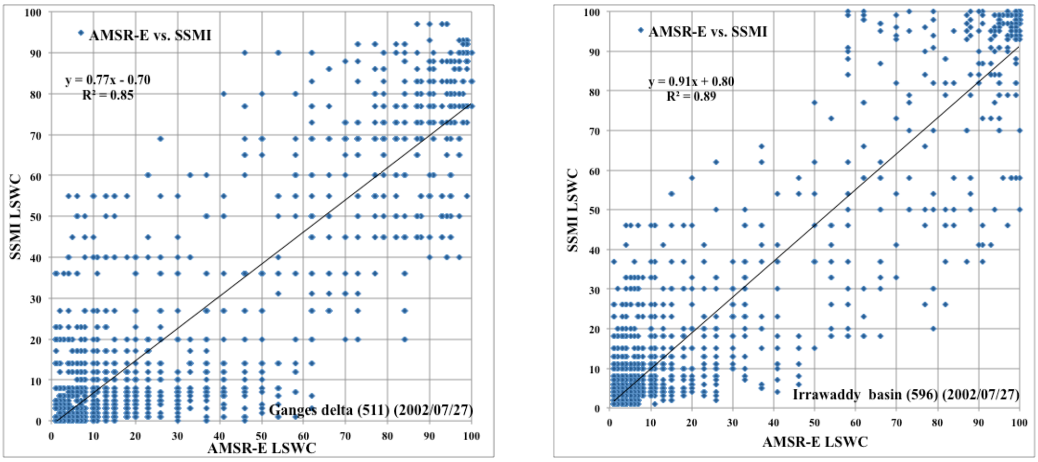

a. Ganges delta (2002/07/27)

b. Irrawaddy basin (2002/07/27)

Figure 4.7 Scatter plot representing the relation between SSMI LSWC and AMSR-E LSWC

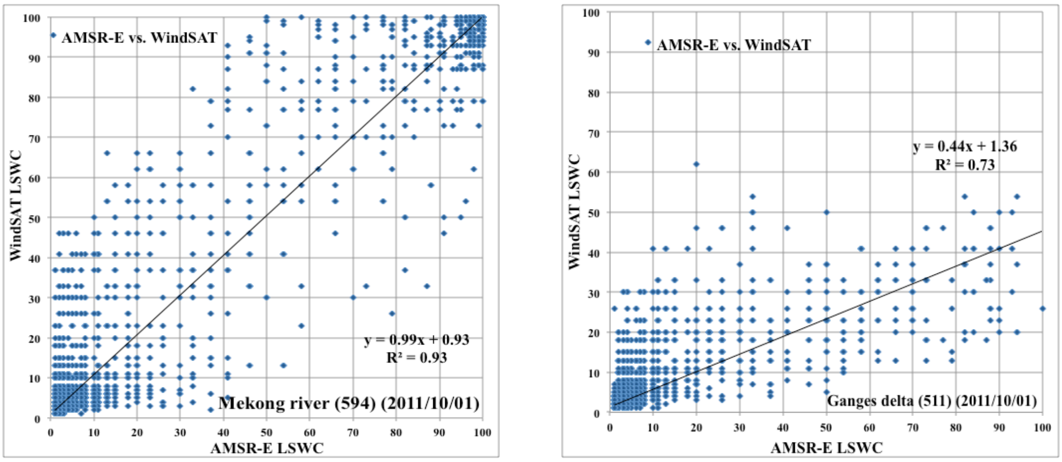

a. Mekong river (2011/10/01)

b. Ganges delta (2011/10/21)

Figure 4.8 Scatter plot representing the relation between AMSR-E LSWC and WindSAT LSWC

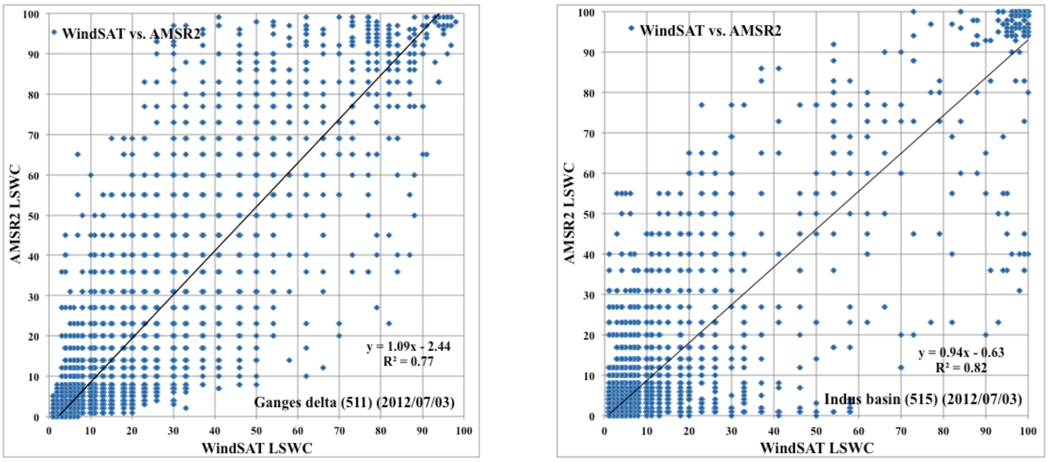

a. Ganges delta (2012/07/03)

b. Indus basin (2012/07/03)

Figure 4.9 Scatter plot representing the relation between WindSAT LSWC and AMSR2 LSWC

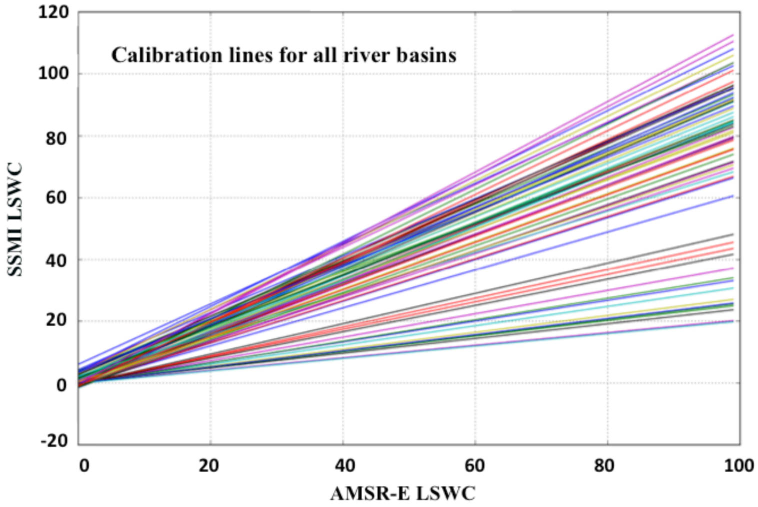

Figure 4.10 Calibration line of SSMI with AMSR-E for all the river basins

Table 4.3 The regression equation and evaluation parameters between SSMI and AMSR-E

ID	Function	R2	ID	Function	R2	ID	Function	R2
500	y=0.61x-0.43	0.65	400	y=0.98x-0.44	0.90	100	y=0.261x-0.11	0.69
510	y=0.79x+0.31	0.73	410	y=0.85x+0.81	0.71	110	y=0.85x+1.19	0.77
511	y=0.77x-0.70	0.85	420	y=0.20x-0.06	0.23	120	y=0.68x-0.79	0.77
512	y=0.87x-1.74	0.94	430	y=0.82x+0.39	0.64	130	y=0.67x+2.13	0.53
513	y=0.85x-1.52	0.80	440	y=0.24x+0.01	0.37	140	y=0.73x-1.11	0.70
514	y=0.80x+1.33	0.65	450	y=0.92x+4.17	0.73	150	y=0.71x+0.28	0.58
515	y=0.81x-0.86	0.63	460	y=0.25x-0.01	0.34	160	y=0.95x+2.54	0.85
520	y=0.34x-0.22	0.58	470	y=0.87x-1.39	0.85	170	y=0.87x+3.22	0.76
530	y=0.80x+3.89	0.53	480	y=0.31x-0.29	0.43	180	y=0.76x-1.20	0.77
540	y=0.77x-0.84	0.75	490	y=1.01x+3.24	0.71	190	y=1.03x-1.06	0.89
550	y=0.91x+2.38	0.63	491	y=0.89x+0.37	0.83	191	y=0.86x+1.80	0.74
560	y=0.38x-0.44	0.38	492	y=0.95x+1.45	0.67	192	y=1.14x-0.33	0.72
570	y=0.90x+2.41	0.69	493	y=1.06x+3.45	0.61	200	y=0.71x-0.73	0.90
580	y=0.49x-0.59	0.62	300	y=0.26x-0.18	0.38	210	y=1.04x+2.82	0.62
590	y=0.98x+5.89	0.68	310	y=0.99x-0.46	0.67	220	y=0.43x-0.59	0.62

591	y=0.98x-0.85	0.72	320	y=0.86x-1.10	0.83	230	y=0.95x-0.52	0.79
592	y=0.44x-0.53	0.59	330	y=0.79x+0.67	0.72	240	y=0.35x-0.51	0.63
593	y=0.90x+1.19	0.74	340	y=0.77x-0.60	0.89	250	y=0.79x-0.08	0.70
594	y=0.82x-1.27	0.67	350	y=0.92x-0.36	0.72	260	y=0.20x-0.20	0.75
595	y=0.90x+1.81	0.76	360	y=0.68x-0.79	0.81	270	y=1.12x-0.22	0.63
596	y=0.91x +0.80	0.89	370	y=1.05x-0.49	0.79	280	y=0.27x-0.10	0.56
630	y=0.90x+2.57	0.77	380	y=0.47x-0.64	0.57	290	y=0.83x+1.53	0.61
690	y=0.91x+3.17	0.76	390	y=0.87x-0.60	0.63			

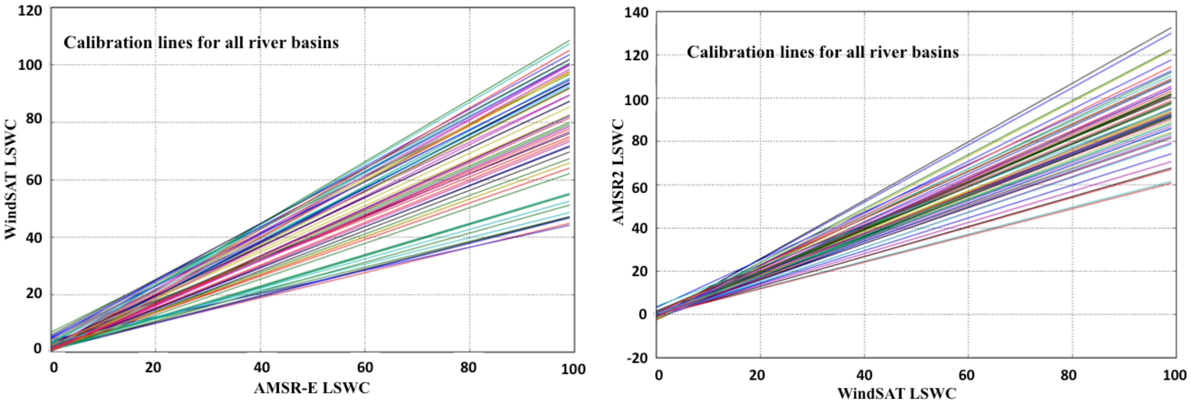

Figure 4.11Calibration line of WindSAR with AMSR-E and AMSR2 with WindSAT for all river basins

4.3 Temporal analysisby calibrated 30 year LSWC dataset

LSWC of one pixel, which has area of 100km², in some flooding areas was computed by combining SSMI, AMSR-E, WindSAT and AMSR2 from 1987 to 2015. Figure 4.12shows daily change of LSWC from 1987 to 2015 of ten flooding events. According to time series plotting, we could learn the variation characteristics and regular pattern of LSWC. The flooding in Tabasco, Mexico and in Songhua river basin, China were used to illustrate, we can see that in Tabasco, Mexico, LSWC increased obviously almost in every year around Nov., which was most evident in 2007, 2008 and 2010, more than 80%. However, in the research area of Songhua river basin, China, LSWC increased obviously only in 2013. We already know that a big flooding happened in Nov. 2007 in Tabasco, Mexico and in Aug. 2013 in Songhua river basin, China according to the International charter. Therefore, we could initially conclude that the flood happened in Tabasco, Mexico belongs to the seasonal flood. Whereas, flood happened in Songhua River basin, China belongs to the flash flood. In previous research, LSWC has been proved a good performance in large-scale flooding detection (Li and Takeuchi, 2014, 2015). Based on viewpoint of retrieval of historical record and long-term database, we can not only detect flood event but also make clear the flooding pattern of each flooding area.

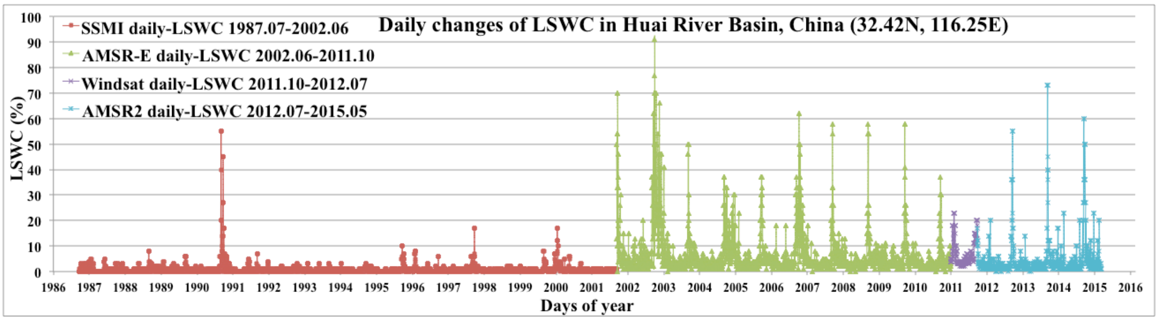

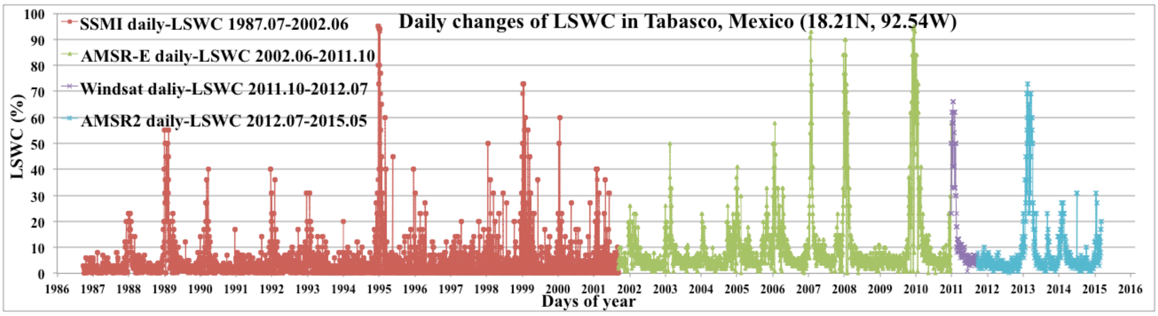

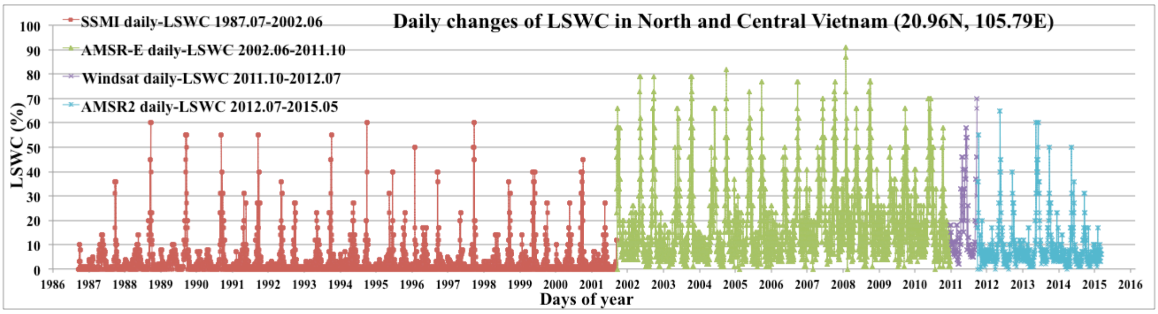

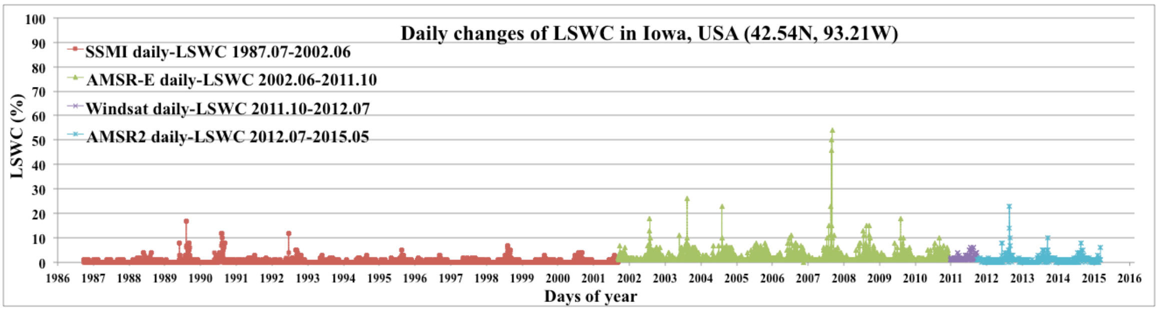
Daily changes of LSWC in Iowa, USA (42.54N, 93.21W)
SSMI daily-LSWC 1987.07-2002.06
AMSR-E daily-LSWC 2002.06-2011.10
Windsat daily-LSWC 2011.10-2012.07
AMSR2 daily-LSWC 2012.07-2015.05
LSWC (%)
0 10 20 30 40 50 60 70 80 90 100
1986 1987 1988 1989 1990 1991 1992 1993 1994 1995 1996 1997 1998 1999 2000 2001 2002 2003 2004 2005 2006 2007 2008 2009 2010 2011 2012 2013 2014 2015 2016
Days of year

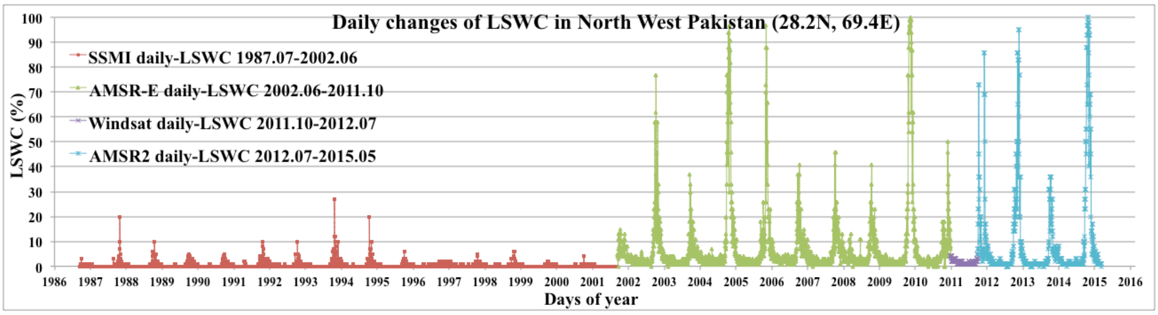
Daily changes of LSWC in North West Pakistan (28.2N, 69.4E)
SSMI daily-LSWC 1987.07-2002.06
AMSR-E daily-LSWC 2002.06-2011.10
Windsat daily-LSWC 2011.10-2012.07
AMSR2 daily-LSWC 2012.07-2015.05
LSWC (%)
0 10 20 30 40 50 60 70 80 90 100
1986 1987 1988 1989 1990 1991 1992 1993 1994 1995 1996 1997 1998 1999 2000 2001 2002 2003 2004 2005 2006 2007 2008 2009 2010 2011 2012 2013 2014 2015 2016
Days of year

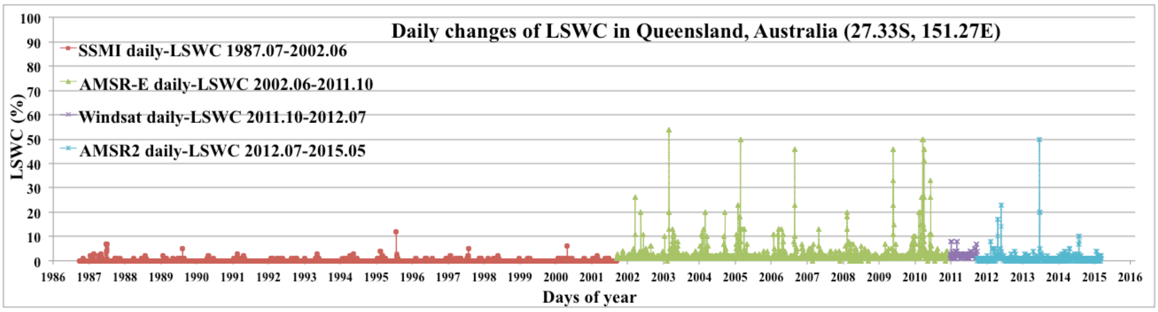
Daily changes of LSWC in Queensland, Australia (27.33S, 151.27E)
SSMI daily-LSWC 1987.07-2002.06
AMSR-E daily-LSWC 2002.06-2011.10
Windsat daily-LSWC 2011.10-2012.07
AMSR2 daily-LSWC 2012.07-2015.05
LSWC (%)
0 10 20 30 40 50 60 70 80 90 100
1986 1987 1988 1989 1990 1991 1992 1993 1994 1995 1996 1997 1998 1999 2000 2001 2002 2003 2004 2005 2006 2007 2008 2009 2010 2011 2012 2013 2014 2015 2016
Days of year

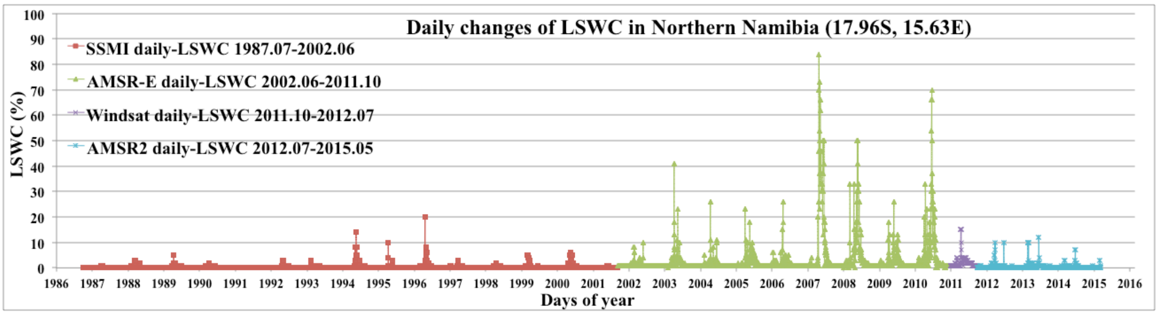
Daily changes of LSWC in Northern Namibia (17.96S, 15.63E)
SSMI daily-LSWC 1987.07-2002.06
AMSR-E daily-LSWC 2002.06-2011.10
Windsat daily-LSWC 2011.10-2012.07
AMSR2 daily-LSWC 2012.07-2015.05
LSWC (%)
0 10 20 30 40 50 60 70 80 90 100
1986 1987 1988 1989 1990 1991 1992 1993 1994 1995 1996 1997 1998 1999 2000 2001 2002 2003 2004 2005 2006 2007 2008 2009 2010 2011 2012 2013 2014 2015 2016
Days of year

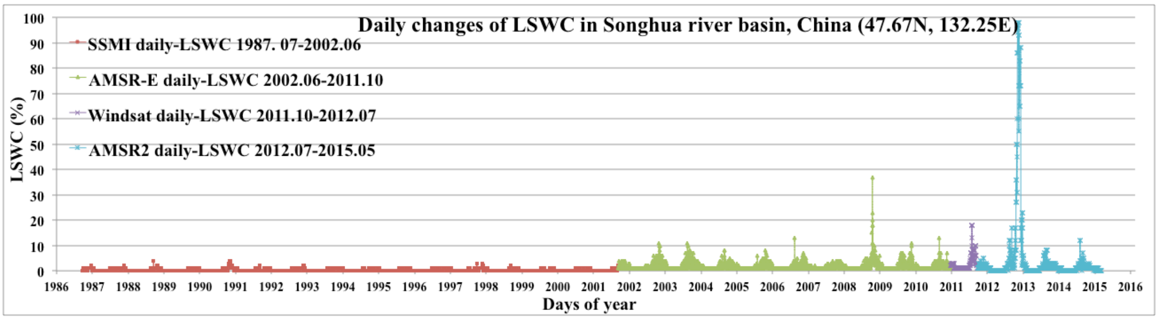
Daily changes of LSWC in Songhua river basin, China (47.67N, 132.25E)
SSMI daily-LSWC 1987. 07-2002.06
AMSR-E daily-LSWC 2002.06-2011.10
Windsat daily-LSWC 2011.10-2012.07
AMSR2 daily-LSWC 2012.07-2015.05
LSWC (%)
0 10 20 30 40 50 60 70 80 90 100
1986 1987 1988 1989 1990 1991 1992 1993 1994 1995 1996 1997 1998 1999 2000 2001 2002 2003 2004 2005 2006 2007 2008 2009 2010 2011 2012 2013 2014 2015 2016
Days of year

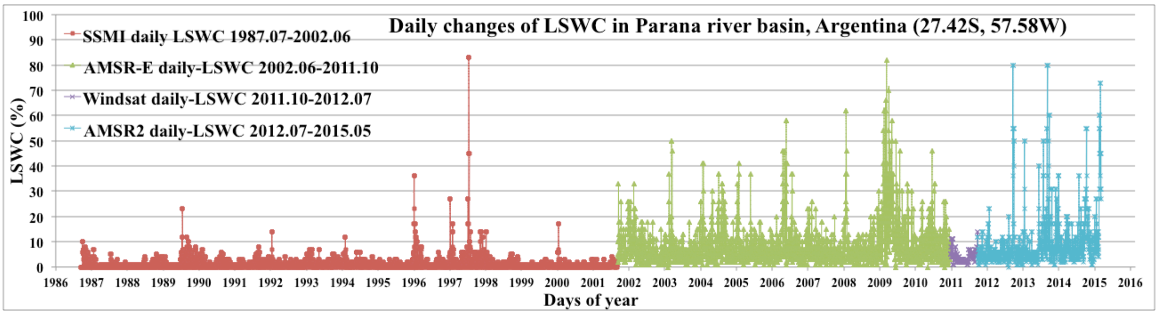

Figure 4.12 Daily change of LSWC in each flooding event from 1987 to 2015

Moreover, the average of LSWC in last 15 years and last 30 years was also calculated to compare with the selected specific year when big flooding happened as Figure 4.13shows. The blue line represents the average LSWC in last 30 years, the red line represents the average LSWC in last 15 years, and the black dotted line represents the LSWC in a specific flooding year. According to 10 cases showed in Figure 4.13, we can see that LSWC during the flooding in specific year significantly exceeds the average. Moreover, we can also see that the trend of LSWC in last 15 years was basically consistent with the trend of LSWC in last 30 years. While the LSWC value of nearly 15 years is greater than the value of nearly 30 years. It is indicated that LSWC has increased year by year, and it was expected a growth trend from now on.

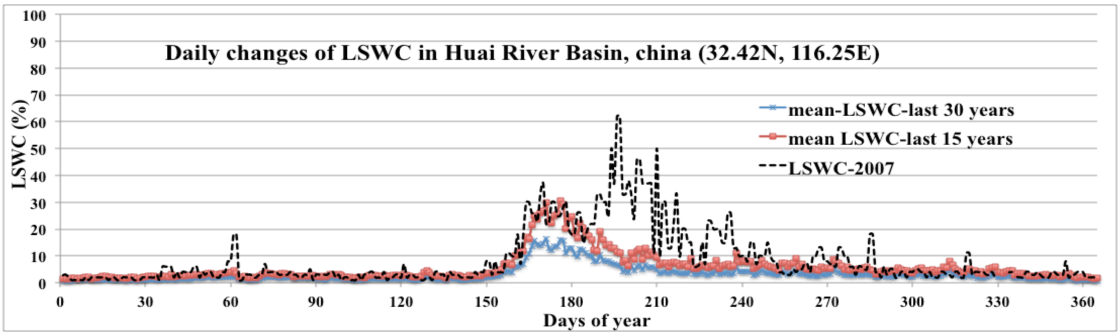

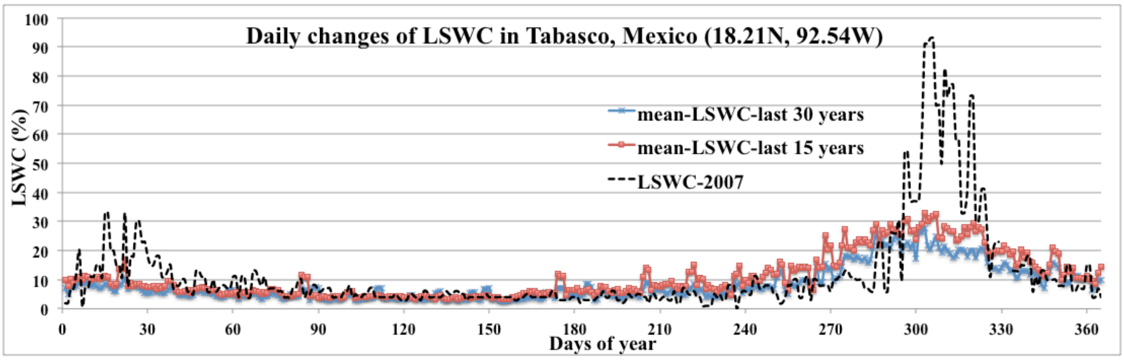
Daily changes of LSWC in Tabasco, Mexico (18.21N, 92.54W)
LSWC (%)
0
10
20
30
40
50
60
70
80
90
100
mean-LSWC-last 30 years
mean-LSWC-last 15 years
LSWC-2007
0
30
60
90
120
150
180
210
240
270
300
330
360
Days of year

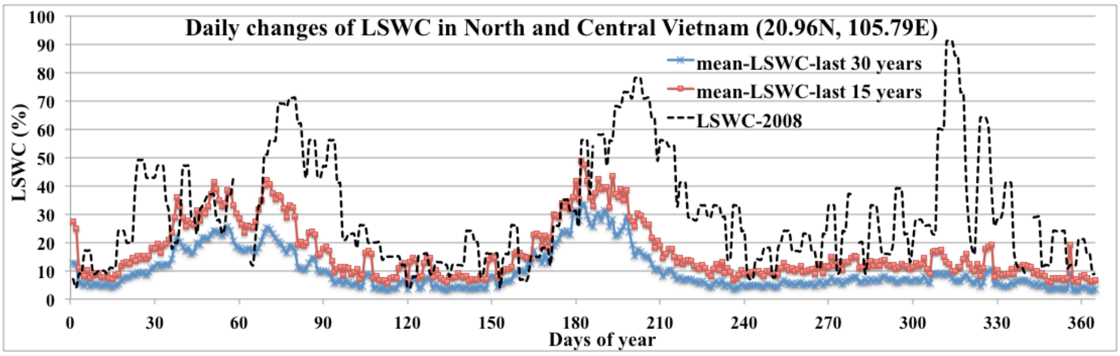
Daily changes of LSWC in North and Central Vietnam (20.96N, 105.79E)
LSWC (%)
0
10
20
30
40
50
60
70
80
90
100
mean-LSWC-last 30 years
mean-LSWC-last 15 years
LSWC-2008
0
30
60
90
120
150
180
210
240
270
300
330
360
Days of year

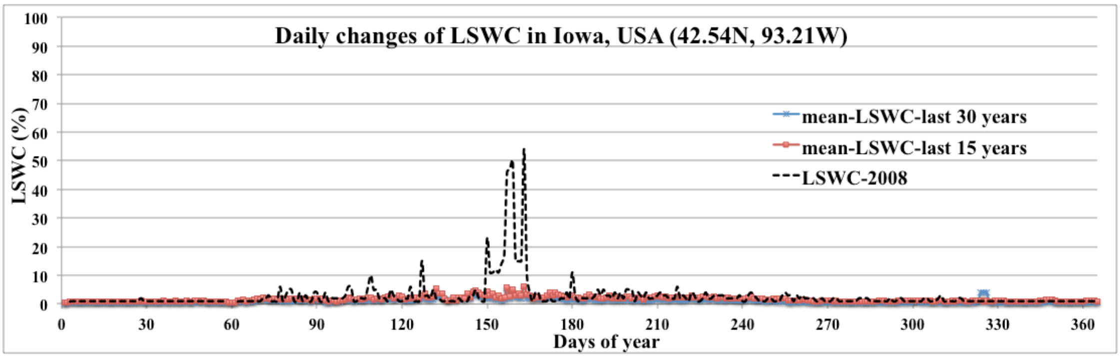
Daily changes of LSWC in Iowa, USA (42.54N, 93.21W)
LSWC (%)
0
10
20
30
40
50
60
70
80
90
100
mean-LSWC-last 30 years
mean-LSWC-last 15 years
LSWC-2008
0
30
60
90
120
150
180
210
240
270
300
330
360
Days of year

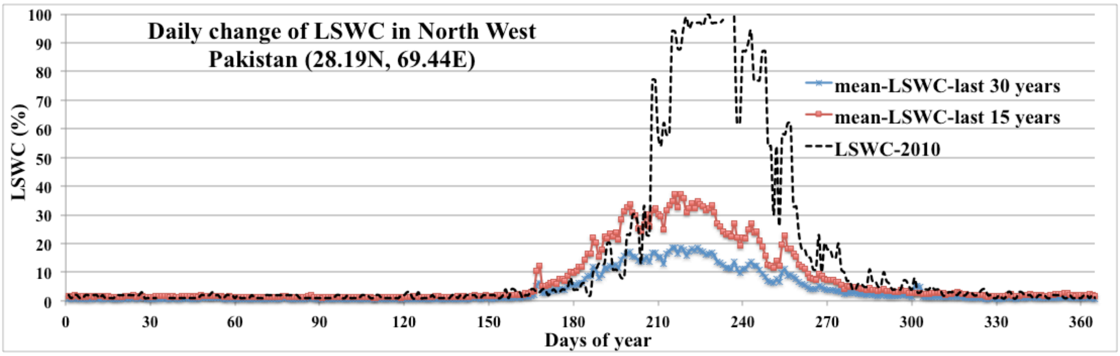
Daily change of LSWC in North West Pakistan (28.19N, 69.44E)
LSWC (%)
0
10
20
30
40
50
60
70
80
90
100
mean-LSWC-last 30 years
mean-LSWC-last 15 years
LSWC-2010
0
30
60
90
120
150
180
210
240
270
300
330
360
Days of year

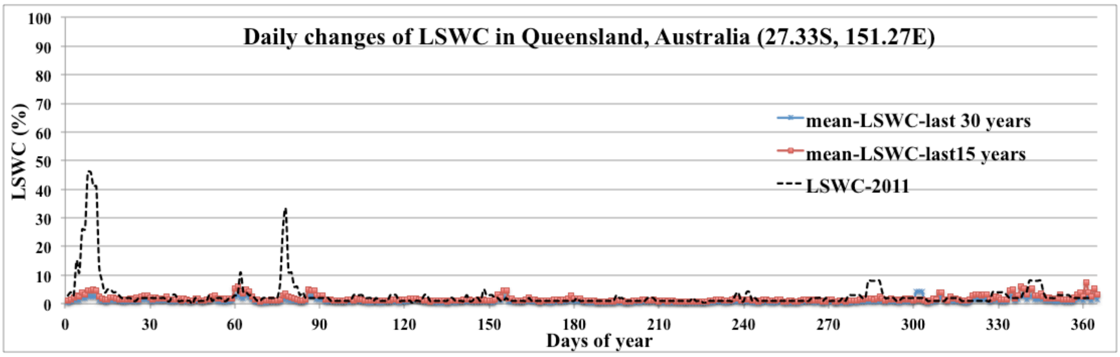

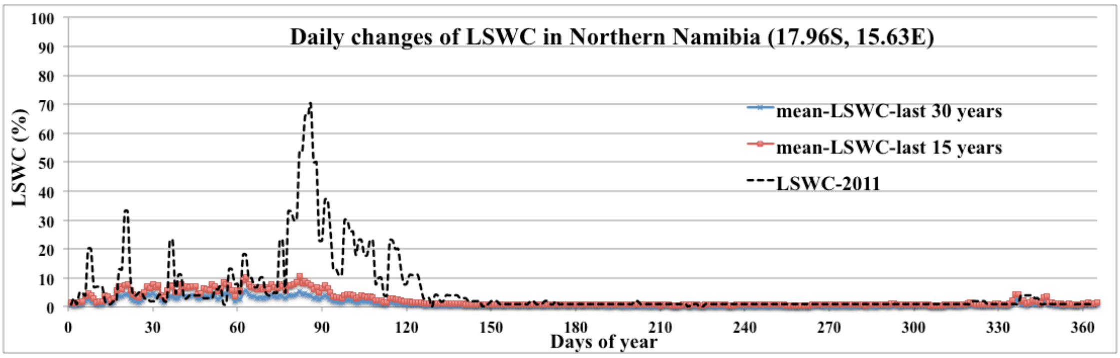

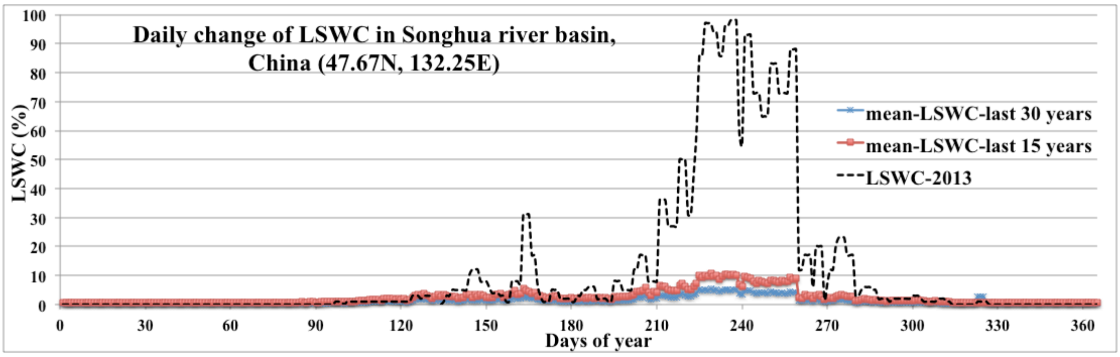

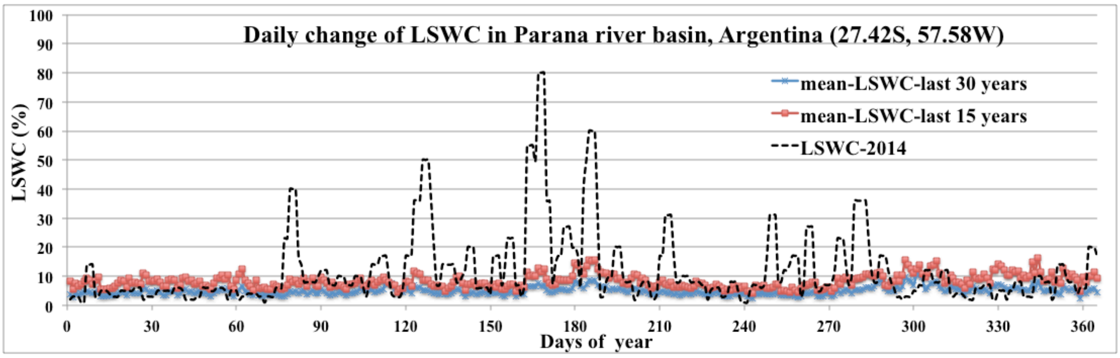

Figure 4.13Comparison of daily changes of LSWC among average of last 30 years and average of last 15 years and a specific flooding year

4.4 Probability density analysis and cumulative distribution function of LSWC

4.4.1 Pixel scale

We chose one representative pixel from each research area and drew cumulative distribution curve belongs to different land use land cover types as Figure 4.14shows. It can be seen that in different land use land cover types the slope of curve changed greatly, shows different kind of curve shapes. From barren land, agriculture land, forest, wetland to urban land, the slope of curve getting flat. Moreover, when LSWC greater than 20, there are one month in one year in the wetland of Mexico. For the urban land in Vietnam there are about three and half months in one year. Table 4.4 shows the cumulative distribution function of each representative pixel. It can be seen that determination coefficient R^2 is bigger than 0.60. From barren land, agriculture land, forest, wetland to urban land, the coefficient of fitting equation is getting bigger, changes from 0.04 to 0.27.

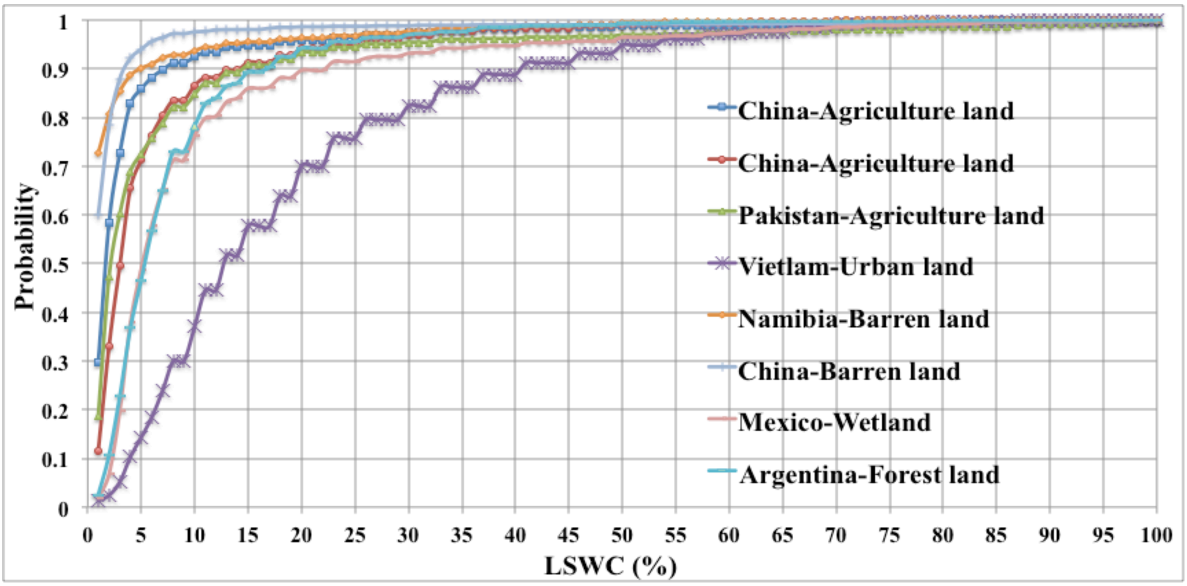

Figure 4.14 Comparison of probability of LSWC in different position of different land use land cover types

Table 4.4 Cumulative distribution function of each representative pixel

Position	Land use land cover	Fitting equation	R^2
Huai river basin 1, China (32.5N 115.8E)	Agriculture	$y = 0.08\ln(x) + 0.69$	0.64
Huai river basin 2, China (32.4N 116.3E)	Agriculture	$y = 0.12\ln(x) + 0.51$	0.74
Pakistan (28.2N 69.4E)	Agriculture	$y = 0.11\ln(x) + 0.55$	0.77
Vietnam (20.9N 105.8E)	Urban land	$y = 0.27\ln(x) - 0.17$	0.95
Namibia (17.9S 15.6E)	Barren land	$y = 0.04\ln(x) + 0.83$	0.86
Songhua river basin, China (47.7N 132.3E)	Barren land	$y = 0.04\ln(x) + 0.85$	0.60
Mexico (18.2N 92.5W)	Wetland	$y = 0.17\ln(x) + 0.28$	0.81
Argentina (27.4S 57.6W)	Forest land	$y = 0.17\ln(x) + 0.32$	0.76

According to the result above, it can be seen a basic regularity among different land use and land cover type. From wetland, forest, agriculture, to barren land, with the increase of aridity, the probability with high LSWC in one year decreases. The probability of LSWC can also be inferred by land use land cover type.

4.4.2 Global scale

With the same method, we got 100 images to show the probability and cumulative distribution for all the pixels corresponding to different LSWC value on global scale. Figure 4.15 is probability distribution map for each LSWC value in global area and Figure 4.16 is cumulative distribution map for each LSWC value in global area during nearly 30 years. From Figure 4.15, we can see that some areas like North Africa, Mongolia, where the CDF tend to be maximum when LSWC is 1, are always very dry. Whereas when the CDF in almost all the area tend to be 1, but some areas like Yangtze basin, Ganges basin, still remained small value. It can be proved they are very wet areas. Based on it, we could know cumulative distribution corresponding to each LSWC value on global scale.

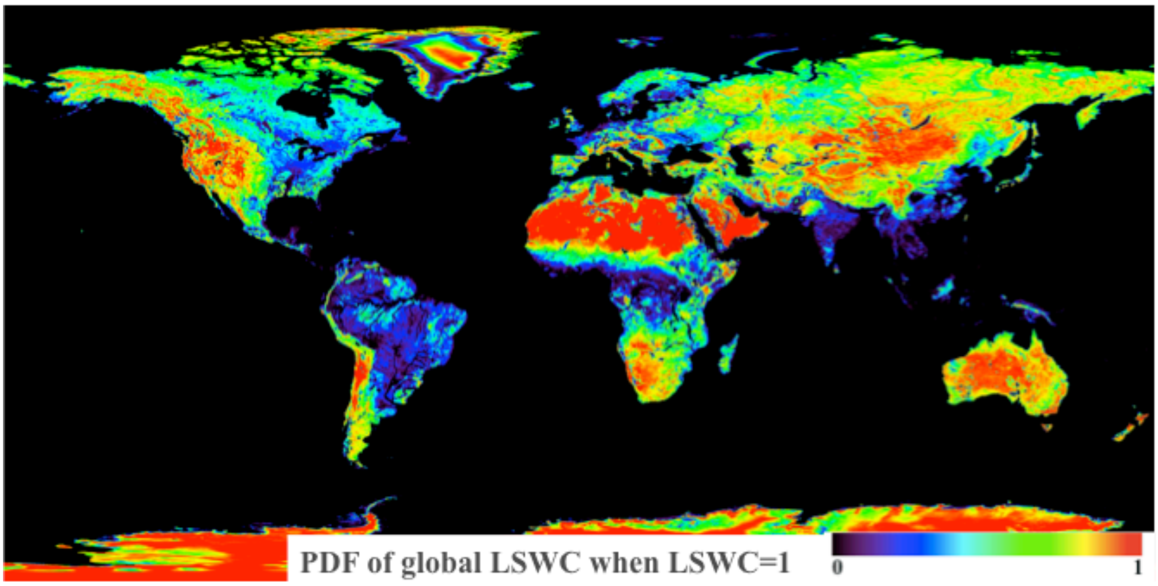

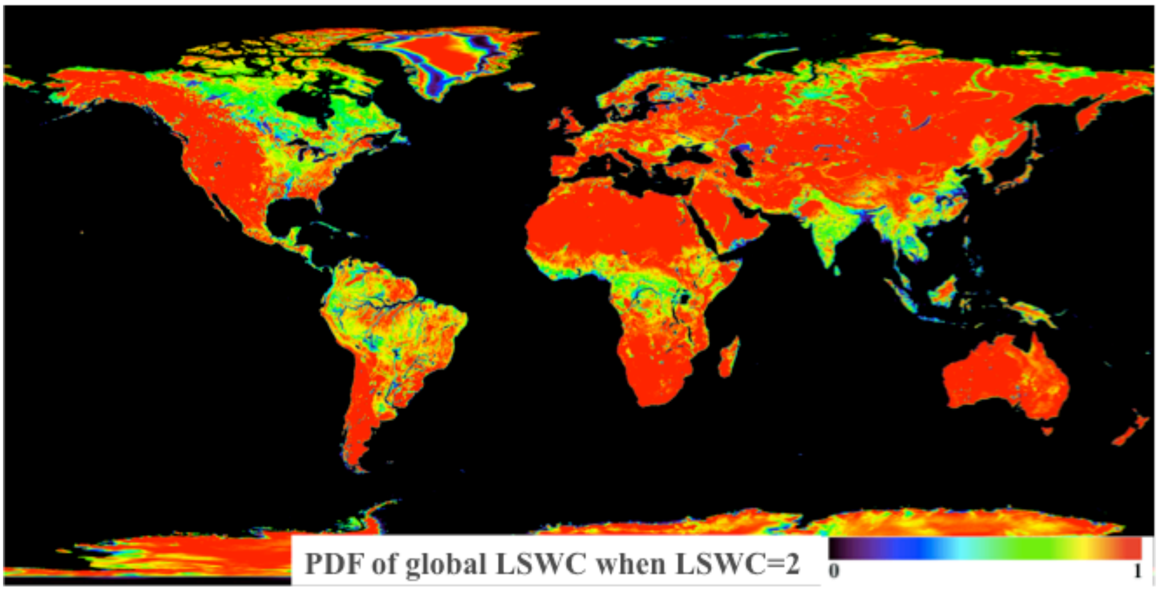
PDF of global LSWC when LSWC=2
0
1

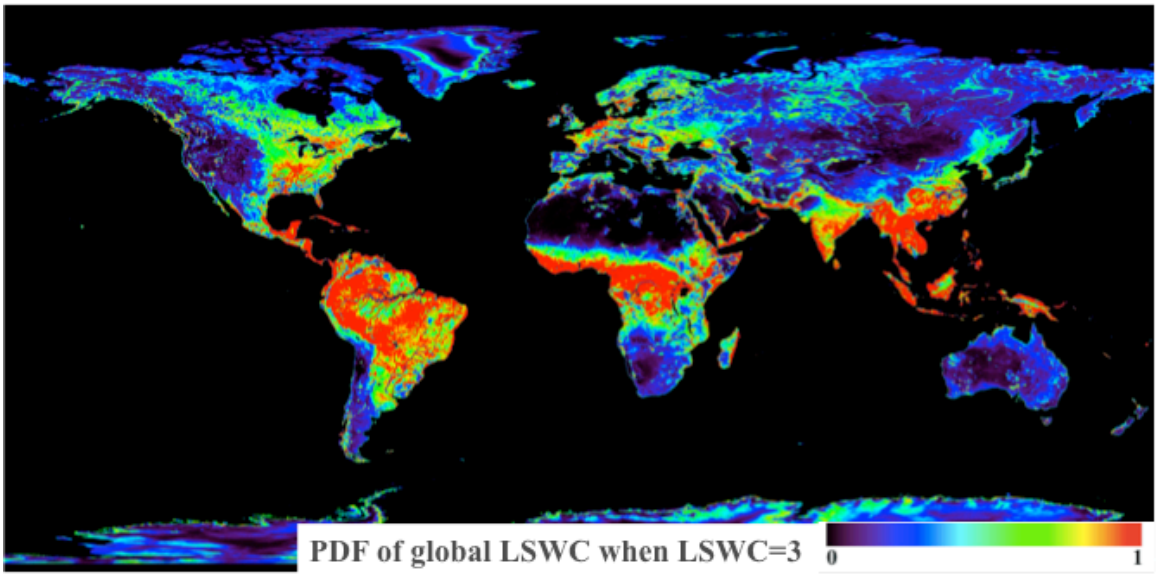
PDF of global LSWC when LSWC=3
0
1

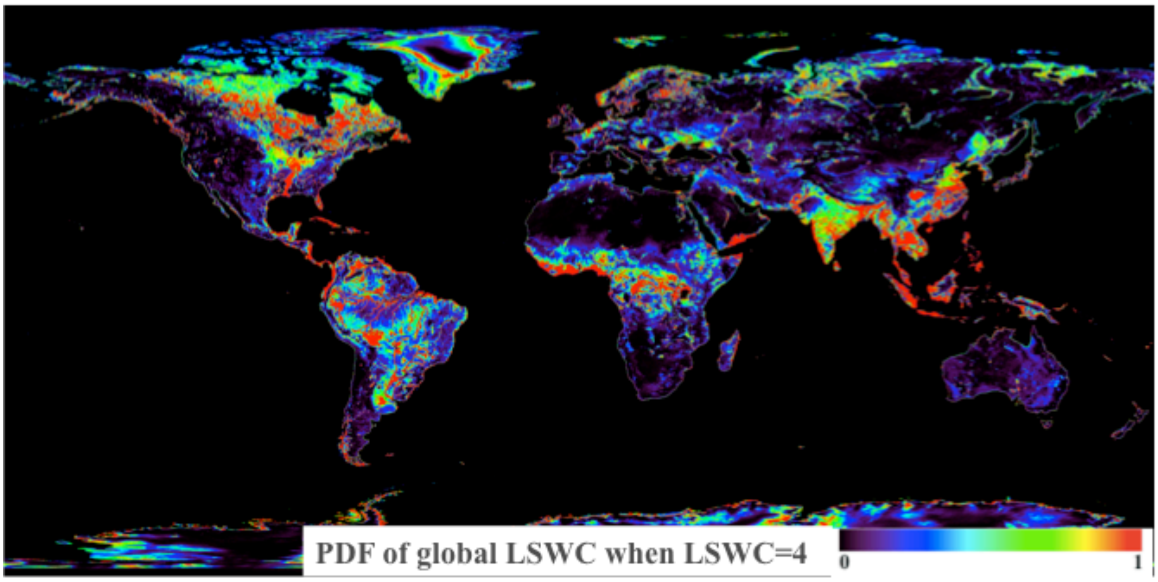

Figure 4.15Probability distribution map of each LSWC value in global area

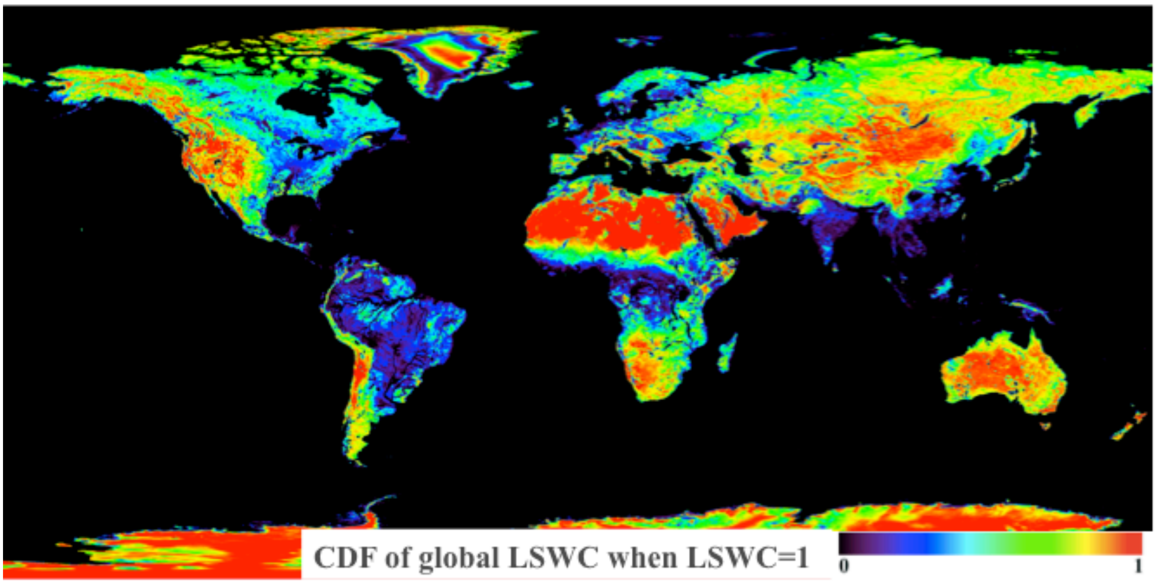

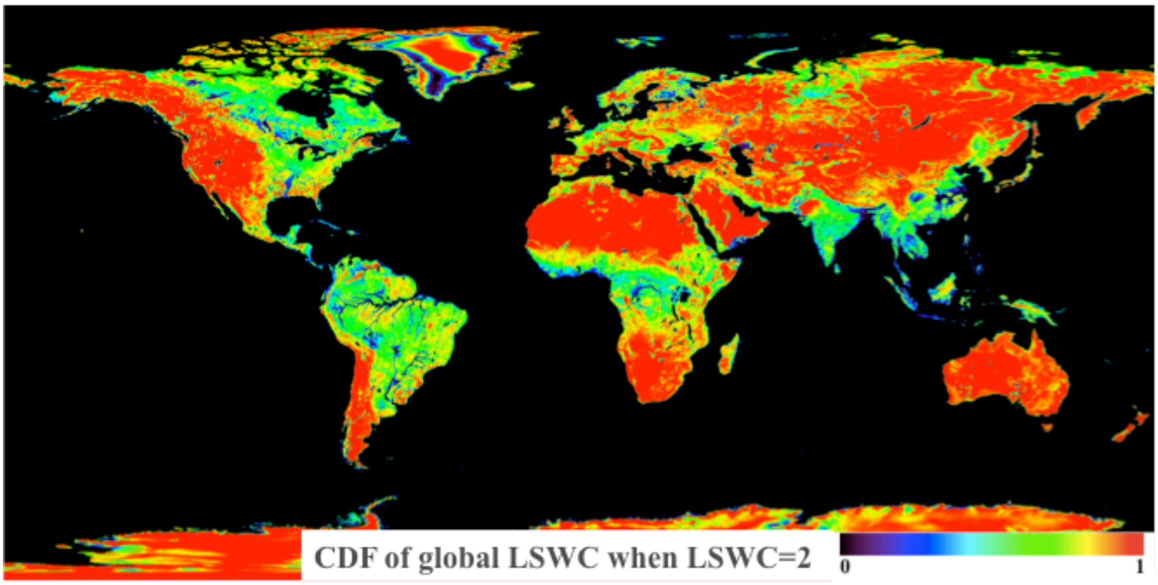
CDF of global LSWC when LSWC=2
0
1

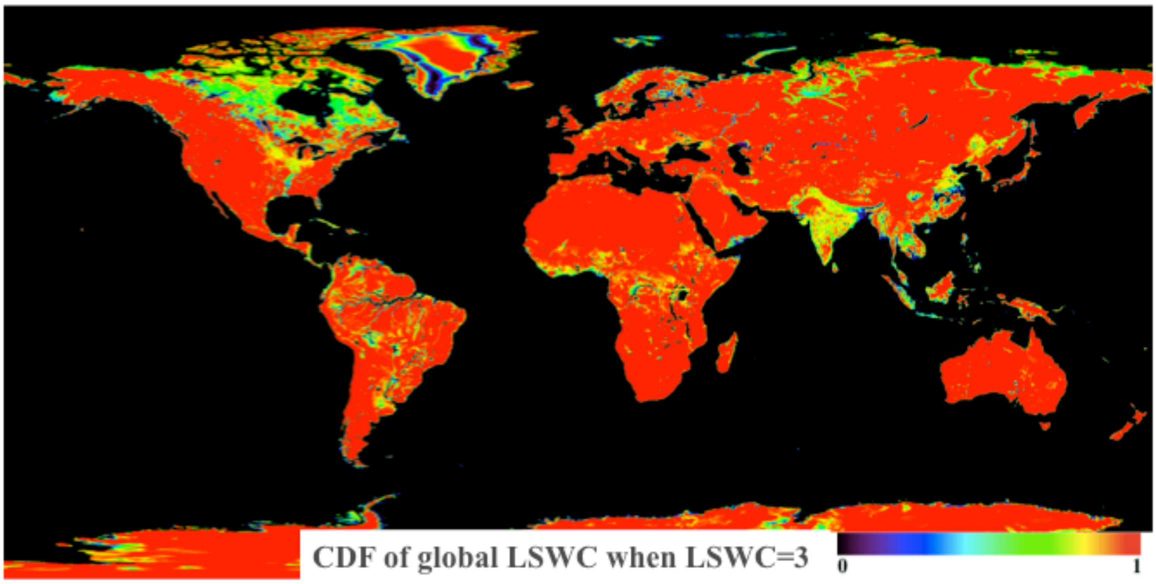
CDF of global LSWC when LSWC=3
0
1

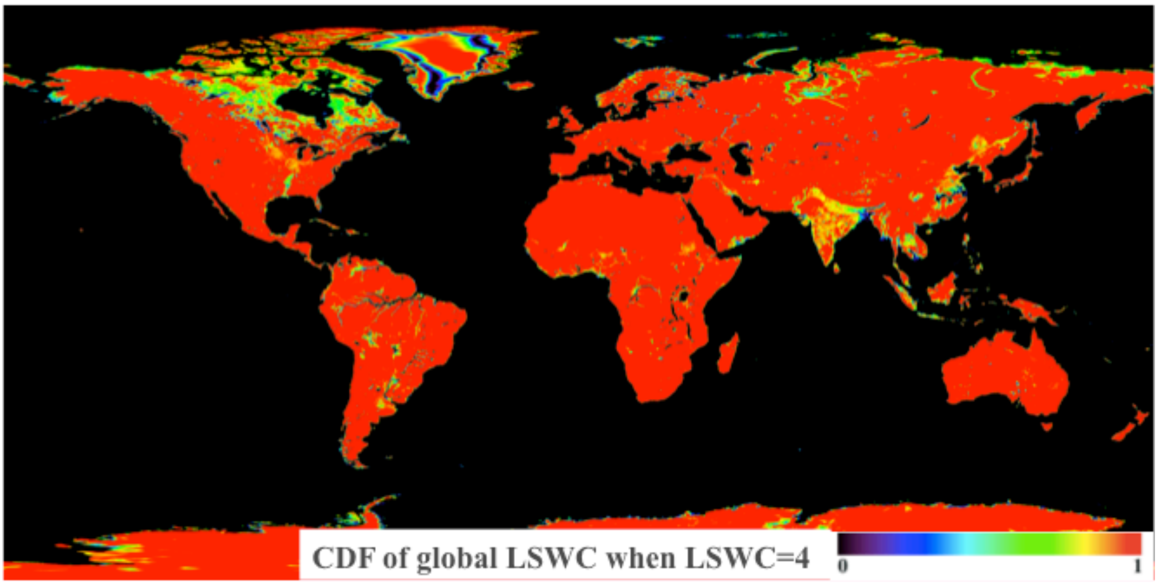

Figure 4.16Cumulative distribution map of each LSWC value in global area during 30 years

4.5 Discussion and Conclusion

In this part, at first, the 68 major river basins were derived in the worldwide. Then, LSWC derived from SSMI, AMSR-E, WindSAT, AMSR2 was mapped and cross calibration among each passive microwave radiometers in the alternate process of sensors was conducted for each river basin. Based on every calibration equations, the original database was modified and finally we got a cross calibrated LSWC database in time series from 1978 to 2015 successfully. In addition, by conducting temporal analysis by cross-calibrated LSWC database, it was found that the LSWC value of latest 15 years is greater than the value of latest 30 years. It is indicated a growth trend in LSWC during last 30 years. What's more, we calculated the histogram and probability of LSWC by integrating data during 30 years and created a global cumulative probability distribution data set in global scale. From wetland, forest, agriculture, to barren land, with the increase of aridity, the probability with high LSWC in one year decreases. It is indicated that the probability of LSWC can be inferred by land use land cover type.

Chapter5. Analysisof precipitation and land cover change on the global LSWC database& LSWC anomaly detection

5.1 Datasets and methods

5.1.1 Climate variables of precipitation analysis by CRU_TS_V3.23

The gridded CRU_TS (time-series) v3.23 dataset, produced by the Climatic Research Unit (CRU) at the University of East Anglia, provides month-by-month variations in climate over the period from 1901 to 2014 with 0.5×0.5 degree grids (Hulme, 1992, Hulme et al., 1998). Firstly the same coordinate system (Geographic Lat/Lon in WGS84) was defined to CRU_TS precipitation data as projection of river basin in order to combine rainfall dataset with river basin. Then rainfall pattern of each major river basin was computed by integrating long time series of data from 1980 to 2014 in order to compare with the LSWC pattern of the same river basin.

5.1.2 STL analysis and correlation analysis

Linear regression has been widely applied to the trend analyses, however, it is unable to provide accurate assessment of nonlinear trends (Shamsudduha et al. 2009). A nonparametric time series decomposition method known as STL is capable of detecting nonlinear patterns in the long-term trends (Shamsudduha et al. 2009). STL is a filtering procedure based on locally weighted regression smoother (LOESS) for decomposing time series data into trend, seasonal and remainder component (Cleveland et al., 1990). STL provides an accurate and robust estimation of trend and seasonal components due to its capacity to deal with outliers or missing values within the time series (Jacquin et al. 2010). It has been used to assess the degradation of vegetation cover in the

Madagascar savanna based on MODIS NDVI time series data (Jacquin et al. 2010).

STL decomposes time series data into three separate components—seasonal (St), trend (Tt) and remainder (Rt):

$Xt=St + Tt + Rt$ (2)

The seasonal component provides the information of phenology cycle of the research variables, the trend component enables determination of the direction of change during the study period (Jacquin et al. 2010). The trend component was modeled by a piecewise linear function.

The cross-correlation was used to detect the temporal relationship between the trend component of monthly LSWC and the trend component of monthly precipitation. Cross-correlation was calculated in software R. Least-square linear fit of the annual change of LSWC was carried out to explore yearly trend of LSWC in this study. The accuracy test was conducted using the coefficients of determination (R2) for linear models (Chang et al. 2014).

5.1.3 Land cover change map

The land cover maps from year of 1992 (UMD_LC), 2000 (GLC2000) and 2012 (BU_LC) were used to discuss and explore the relationship between land cover change and LSWC change (Loveland et al., 2000, Friedl et al., 2002, Bartholome and Belward, 2005). The specification of three land cover products is shown in Table 5.1 (Zhang and Tateishi, 2013, Song et al., 2014). Based on three kind of classification schemes and conversion legends as shown in Table 5.2 (Bai et al., 2014), urban area, forest, cropland area and water body for the years 1992, 2000 and 2012 was masked out respectively. Finally the land area change of each land cover type in each major river basin was calculated.

Table 5.1 Characteristics of the three global land cover data sets assessed in this study.

Global land cover data set	Classification scheme	Sensor	Date	Number of classes	Resolution
UMD_LC	Simplified IGBP	AVHRR	1992	14	1km
GLC2000	FAO LCCS	SPOT-4	2000	23	1km
BU_LC	IGBP	MODIS	2012	17	1km

Table 5.2 Conversion legends table of three land cover maps.

Target legend	1992 (UMD-LC)	2000 (GLC2000)	2012 (BU-LC)
Cropland	Class 11	Class16-18	Class 12, 14
Forest	Class1-6	Class1-6, 9-10	Class 1-5, 8
Urban	Class 13	Class 22	Class 13
Water	Class 0	Class 20	Class 0

5.2 Time series analysis between precipitation and LSWC

In order to make clear the relationship between rainfall and LSWC, the monthly precipitation change of all river basins worldwide was computed by integrating long-term monthly CRU precipitation dataset from 1981 to 2014. In addition, daily LSWC change from 1987 to 2015 based on cross-calibrated LSWC dataset combining with SSM/I, AMSR-E, WindSAT and AMSR2for each river basin was computed. The graph of comparison of precipitation and water area for 68 river basins were made.

Figure 5.1 shows the corresponding relationship between precipitation and water area for some major river basin. It can be seen that the water area change pattern basically coincides with the rainfall pattern, showing a seasonal variation characteristic within each year. Moreover in the long term, the trend of continued growth or decreasing in rainfall is not clear whereas water area showed an increasing trend. Figure 5.2 shows least square linear fit of the annual total change of water area. We can see that water area in these river basins showed an annual increasing trend. It can be indicated that rainfall is not the only factor that makes the change of LSWC.

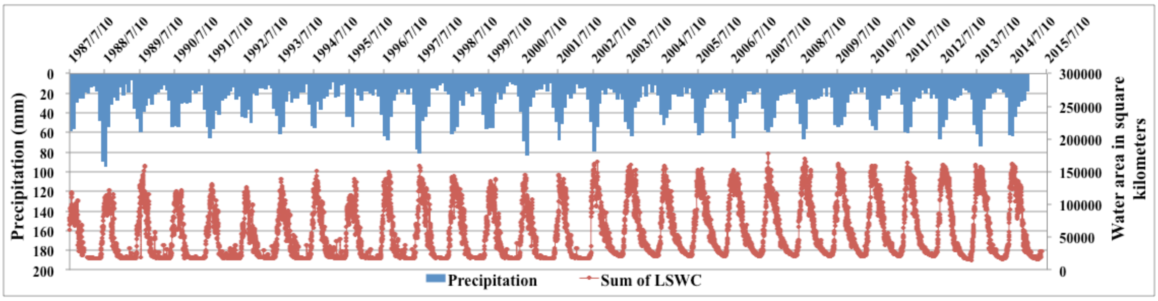

a. Machenzie (120)

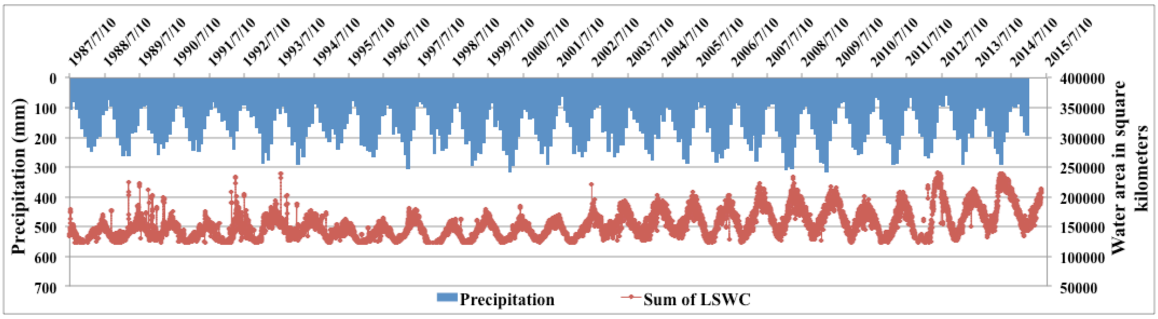

b. Amazon (240)

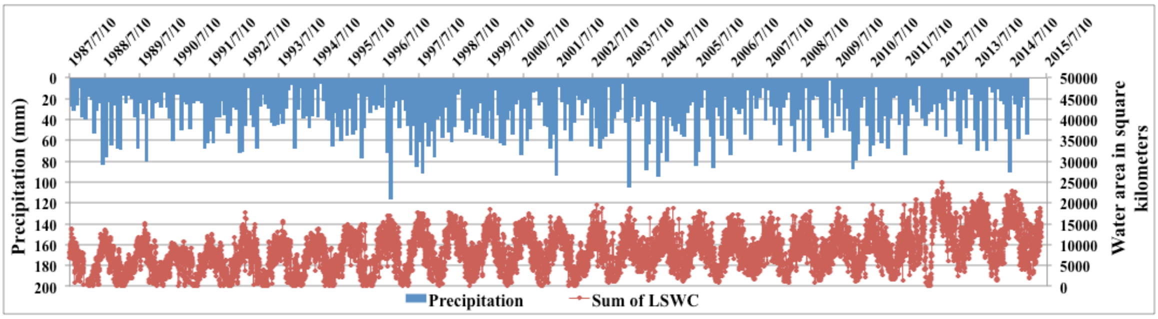

c. North Black Sea Coast (450)

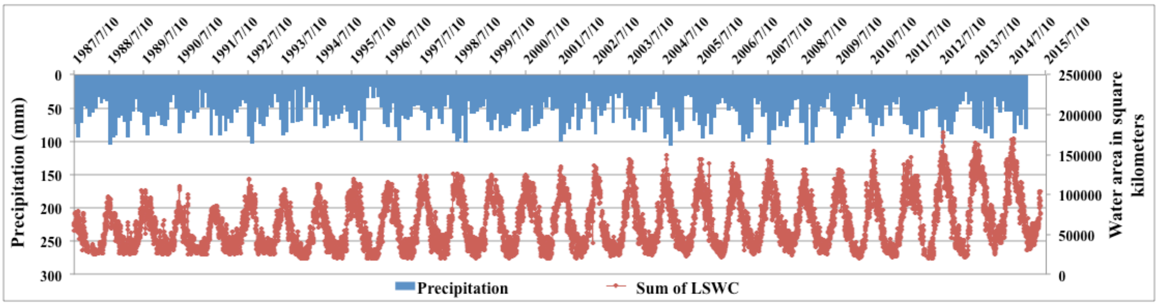

d. Sweden/Finland/Scandinavia (492)

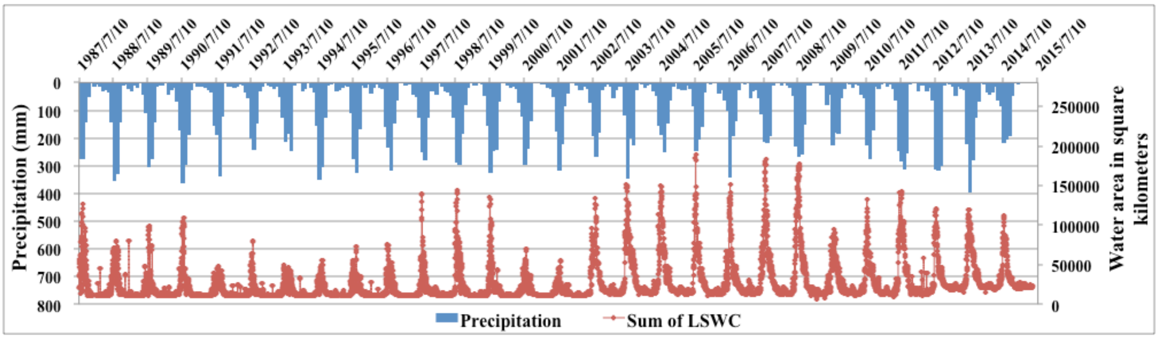

e. Ganges (511)

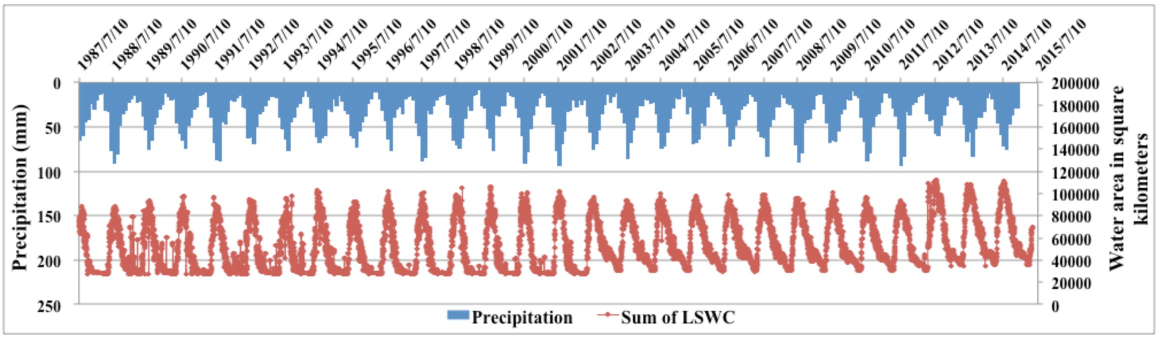

f. Yenisey (540)

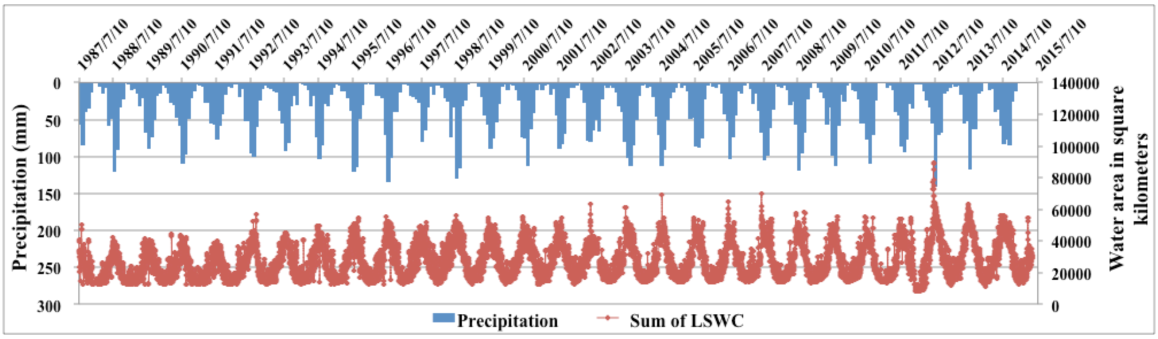

g. Huang He (591)

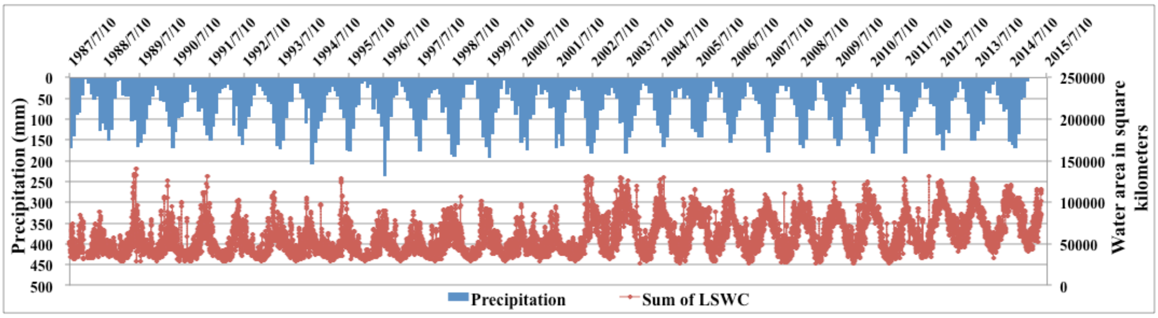

h. Yangtze (592)

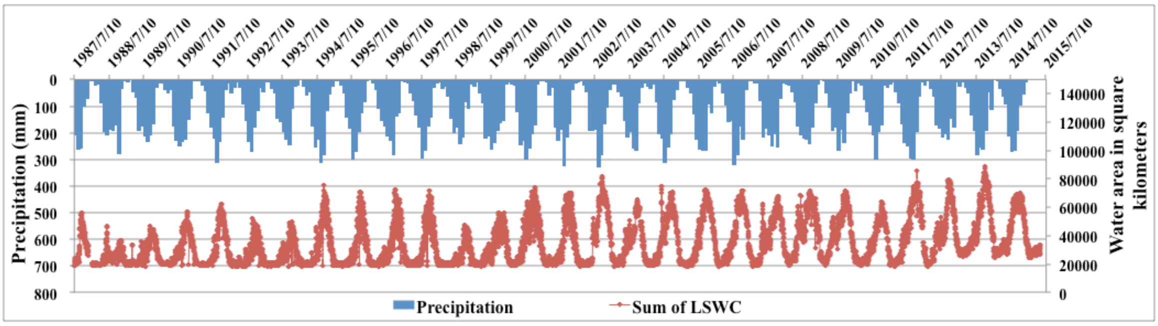

i. Mekong (594)

Figure 5.1 Daily change of water area and monthly change of precipitation of each river basin.

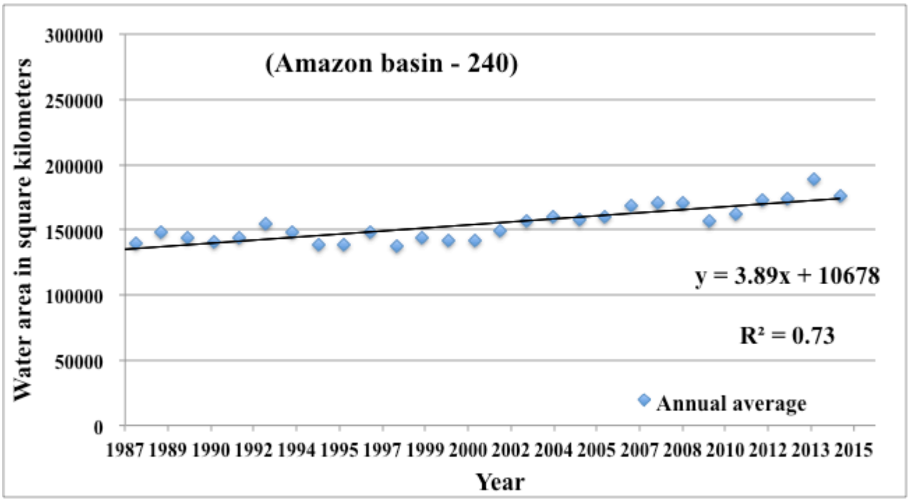

a. Amazon (240)

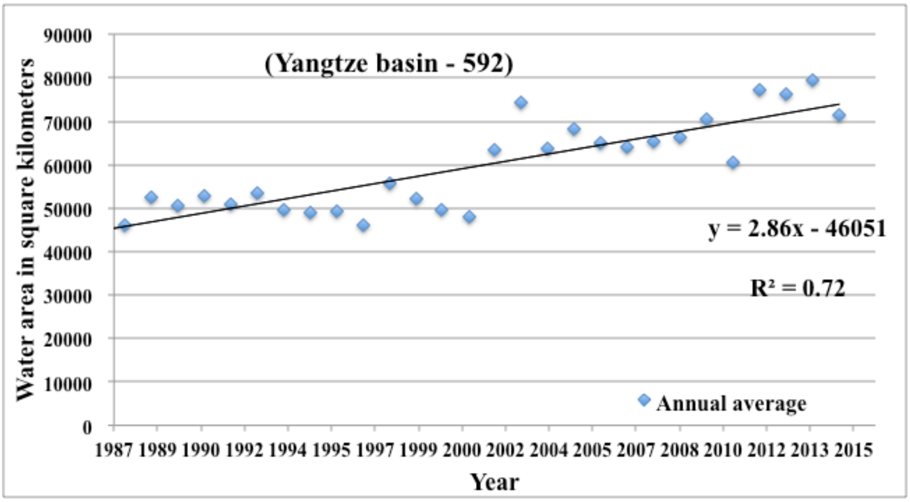

b. Yangtze (592)

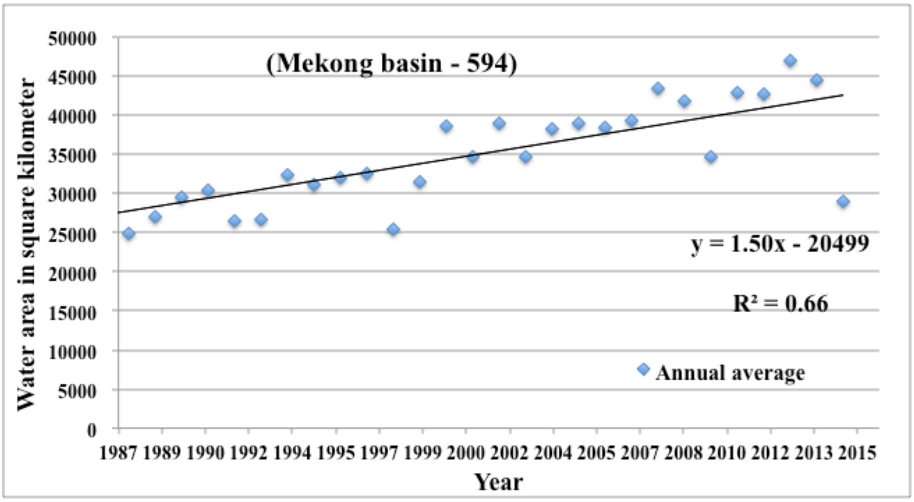

c. Mekong (594)

Figure 5.2 Least square linear fit of the annual change

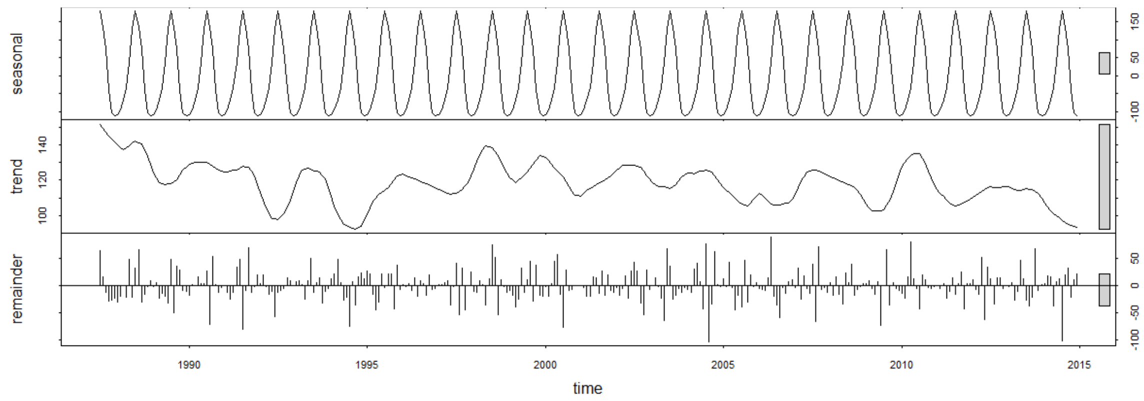

Figure 5.3 Seasonal trend and long-term trend of precipitation in Brahmaputra (510)

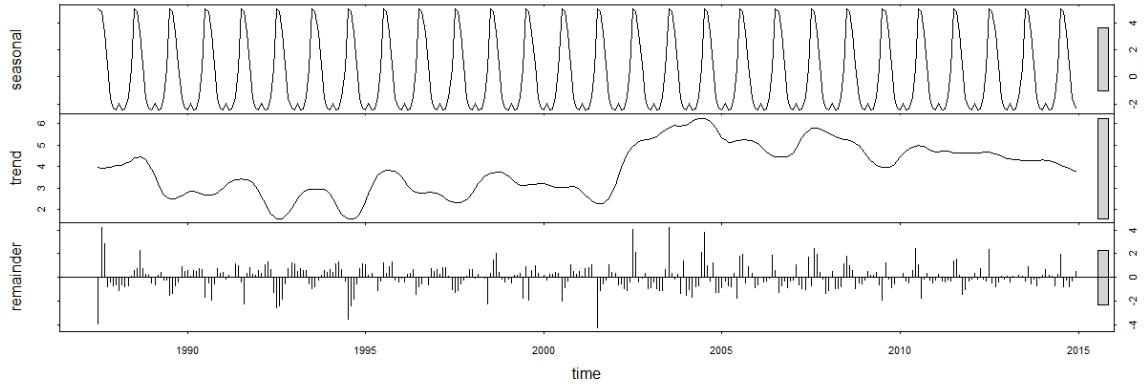

Figure 5.4 Seasonal trend and long-term trend of LSWC in Brahmaputra (510)

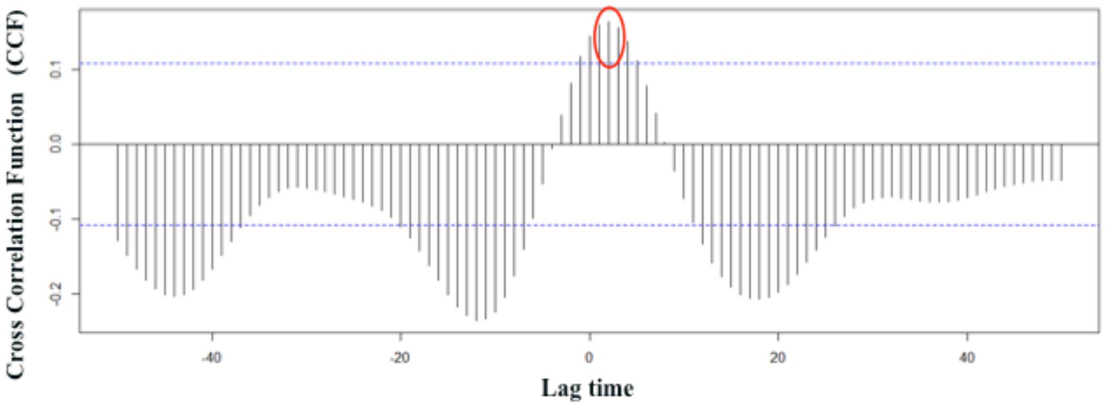

Figure 5.5 The interactive correlation of long-term trend between precipitation and LSWC in Brahmaputra (510)

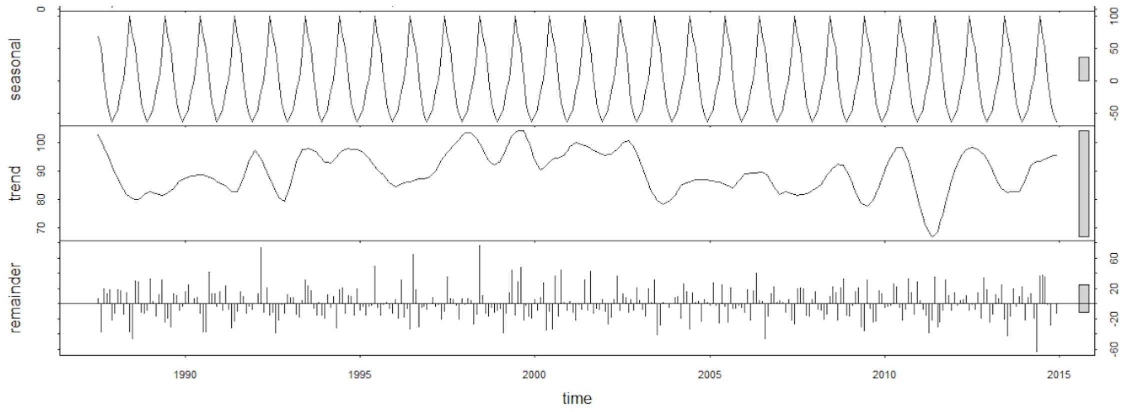

Figure 5.6 Seasonal trend and long-term trend of precipitation in Yangtze basin (592)

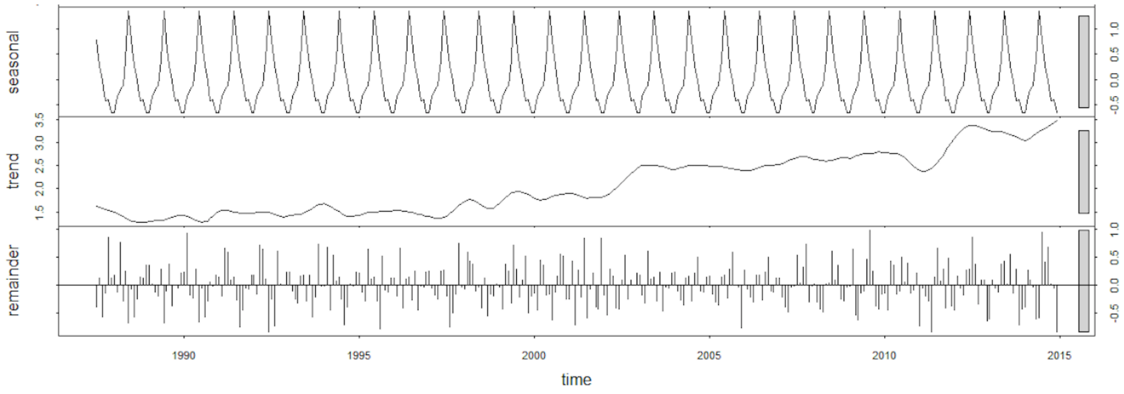

Figure 5.7 Seasonal trend and long-term trend of LSWC in Yangtze basin (592)

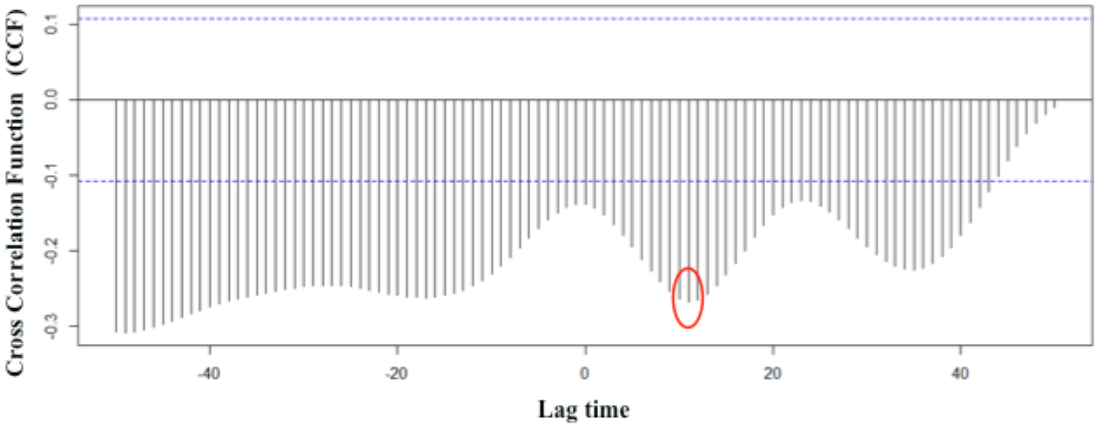

Figure 5.8 The interactive correlation of long-term trend between precipitation and LSWC in Yangtze basin (592)

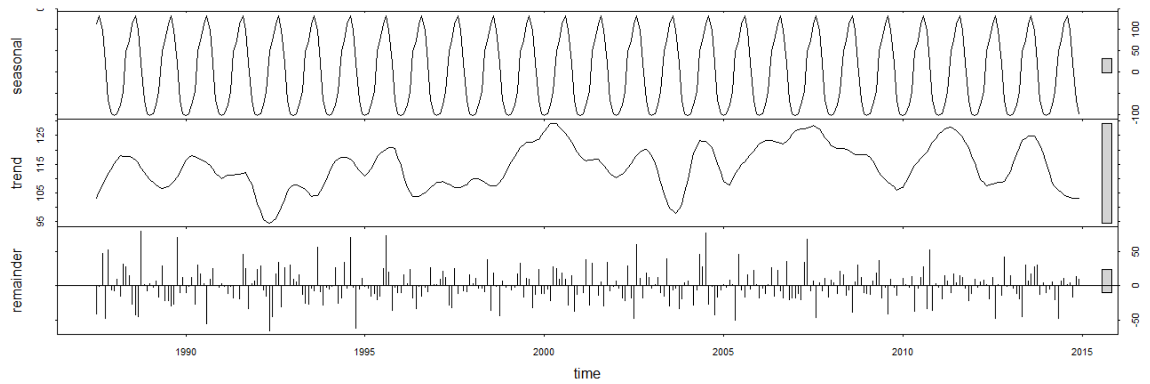

Figure 5.9 Seasonal trend and long-term trend of precipitation in Mekong-river (594)

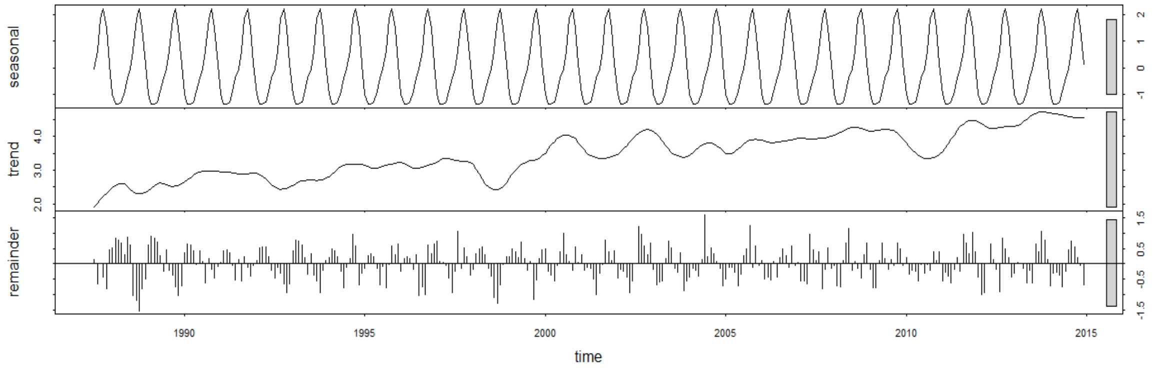

Figure 5.10 Seasonal trend and long-term trend of LSWC in Mekong-river (594)

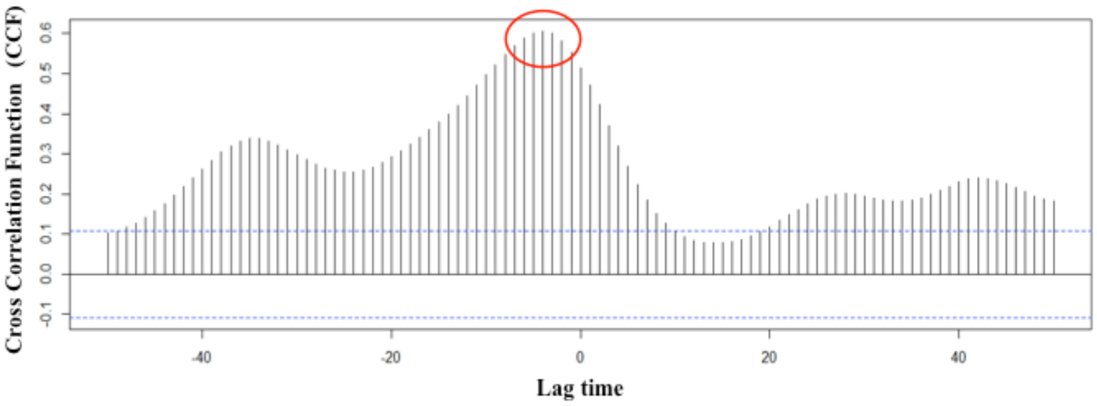

Figure 5.11 The interactive correlation of long-term trend between precipitation and LSWC in Mekong-river (594)

In addition, STL method was used in order to make clear the long-term trend relationship between precipitation and water area change. Figure 5.3, Figure 5.6, Figure 5.9 is seasonal trend and long-term trend of precipitation in Brahmaputra, Yangtze basin and Mekong-river. Figure 5.4, Figure 5.7, Figure 5.10shows seasonal trend and long-term trend of LSWC in Brahmaputra, Yangtze basin and Mekong-river. It was found that the seasonal trend between precipitation and LSWC was very coincided but the long-term trend of them was not identical even though we still can find some similar shape. Moreover, from the interactive correlation of long-term between precipitation and LSWC shown as Figure 5.5, Figure 5.8, Figure 5.11, in Yangtze basin, the precipitation is negatively related to the LSWC and the correlation coefficient was -0.27. In the case in Mekong basin, the interactive correlation coefficient was 0.6. There is some relationship but no significant correlation between long-term trend in LSWC and precipitation. Rainfall was indicated not the only factor that brings about the change in LSWC.

5.3 Trend of water area of each river basin in global scale

After integrating 30 years of global LSWC daily data, the trend of LSWC in each river basin was computed as shown in Figure 5.12. In all 68 basins, almost unchanged river basin just accounted for only 18%, most of them showed obvious growth trend. Declining trend basin accounted for 2.9%, essentially unchanged basin accounted for 20.6%, the growth trend basin accounted for 76.5%

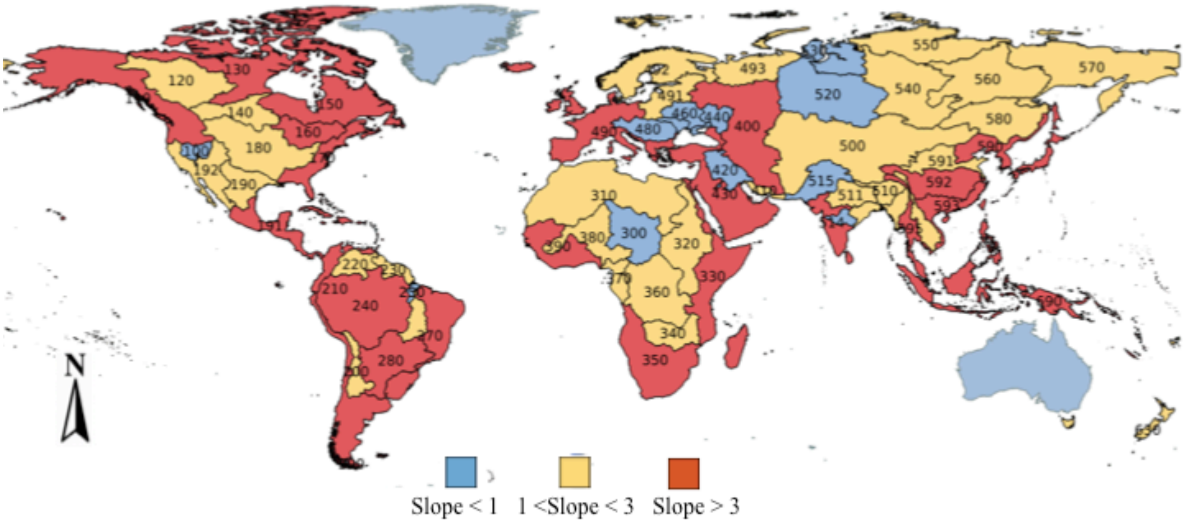

Figure 5.12 The trend of water area on global scale during last 30 years

5.4 The influence of land cover change on LSWC change

5.4.1 Land cover change from the year 1992, 2000 to 2012 in different river basin

To further explore factors affecting LSWC, land cover change has been discussed. Figure 5.13 shows the proportion of cropland, forest, urban and water body area for the year 1992, 2000 and 2012 in different river basin, from which we could clear understand the composition and change of each land cover type during last 20 years. It could be seen there was no clear trend feature in forest cover change. A strong increase in urban area could be found in each basin. Especially in Yangtze basin and Huang He basin from 2000 to 2012, the urban region increased from 0.08% to 0.83% and from 0.17% to 2.21%. It can also be seen that due to global warming, the Himalayan snowmelt year by year, causing water in Brahmaputra river increased significantly. Moreover, from 1992 to 2000 and then to 2012, the proportion of croplands consistent increased. Brahmaputra basin area increased by 13.61%, Yangtze basin increased by 8.02%, especially Ganges basin increased by 41.35%, grew to nearly 70%.

By comparing cropland with LSWC change from 1992, 2000 to 2012 in each basin as shown in Table 5.3, we can find that the cropland presented consistent growth situation along with LSWC. According to the relative change in Brahmaputra basin, the croplands increased by 5% and 8%, while LSWC increased by 4% and 3%. It is hypothesized that since during sowing season irrigation causes cropland surfaces to be covered by water, it could have led it to be detected as an inundated area. Moreover, since the increase of human population and standards of living demand more harvest and production from the earth resources, increased irrigation frequency or sowing time in one year can be anticipated. Thus it is expected that the widespread expansion of cropland may bring about LSWC increasing. In addition, it can also be inferred that the rapid expansion of urban and reduction of forest area may be factors affecting LSWC change.

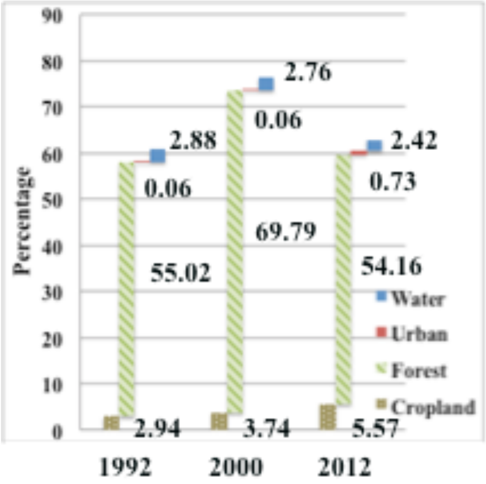

a. Yenisey (540)

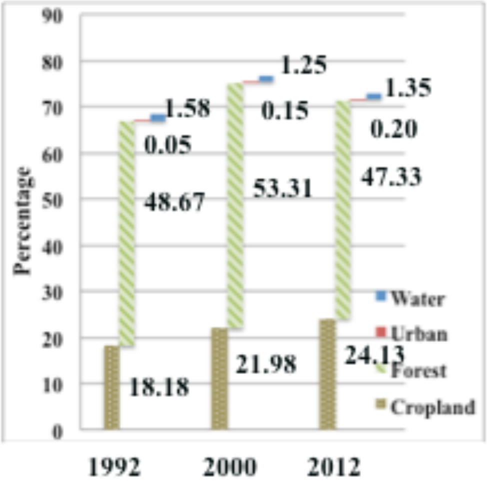

b. AmurBasin(580)

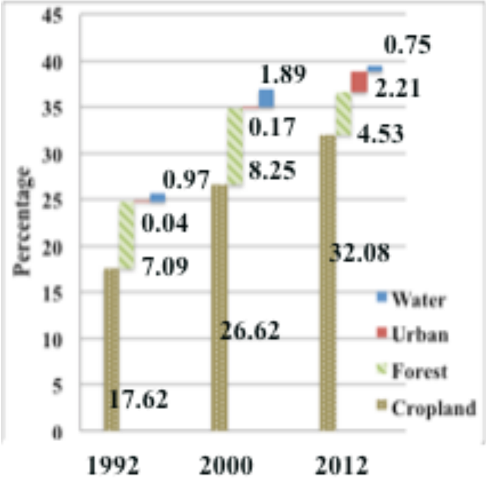

c. Huanghe(591)

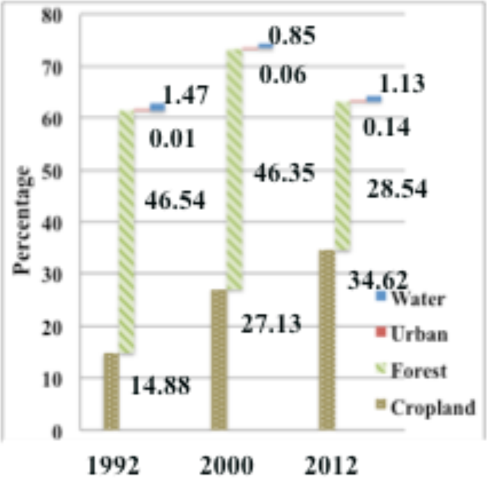

d. Mekong (594)

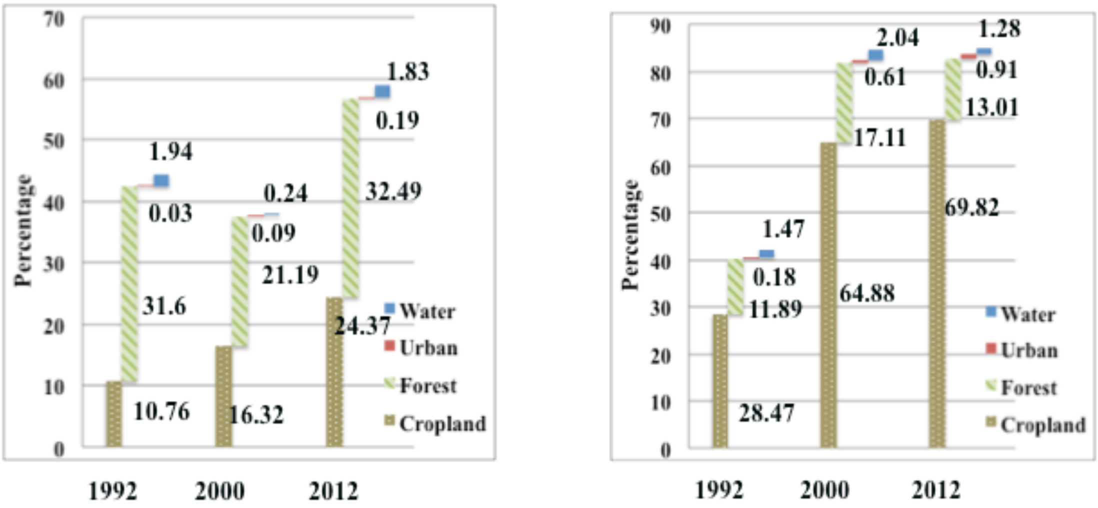

a. Brahmaputra (510)

b. Ganges (511)

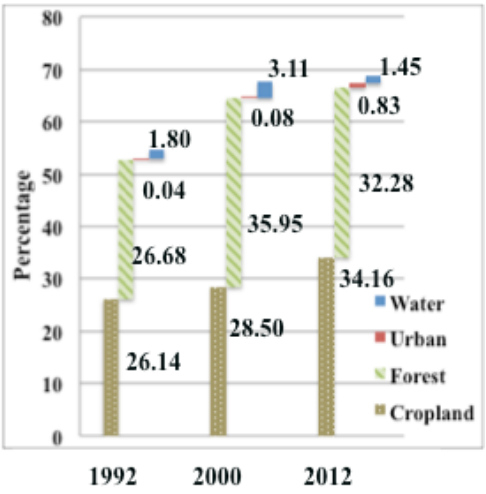

c. Yangtze (592)

Figure 5.13 Proportion of 4 types of land cover for 1992, 2000 and 2012 in each river basin

5.4.2 Compare of cropland area change with LSWC change

Table 5.3 Compare of cropland and LSWC change from 1992, 2000 to 2012 in three basins

River basin	**Category**	**Percentage (%)**					**Correlation coefficient**
		1992	**2000**	**2012**	**Relative change**		
					1992-2000	**2000-2012**	
Brahmaputra	Cropland	11	16	24	5	8	0.99
(510)	LSWC	7	11	14	4	3	
Ganges	Cropland	28	65	69	37	4	0.88
(511)	LSWC	4	5	6	1	1	
Huanghe	Cropland	18	27	32	9	5	0.98
(591)	LSWC	16	20	24	4	4	
Yangtze	Cropland	26	29	34	3	5	0.98
(592)	LSWC	1	2	3	1	1	
Mekong	Cropland	15	27	35	12	8	0.99
(594)	LSWC	3	4	5	1	1	

By comparing cropland with LSWC change from 1992, 2000 to 2012 in each basin as shown in Table 5.3, we can find that the cropland presented consistent growth situation along with LSWC. The correlation coefficients between cropland and LSWC change was more than 0.85. We considered that since during sowing season irrigation causes cropland surfaces to be covered by water, it could have led it to be detected as an inundated area. Moreover, since the increase of human population and standards of living demand more harvest and production from the earth resources, increased irrigation frequency or sowing time in one year can be anticipated. Thus it is expected that the widespread expansion of cropland may bring about LSWC increasing.

5.4.3 Compare of land cover change obtained by FAO and Remote Sensing

In order to validate the land cover change result obtained by method of remote sensing. The statistic data obtained from FAO (Food and Agriculture Organization) was used to compare. Table 5.4 shows the comparison of forest and cropland area in 1992, 2000 and 2012 year obtained by method of FAO and Remote Sensing.

Table 5.4 Comparison of land cover area in 1992, 2000 and 2012 year obtained by FAO and RS

Obtaining method	Land cover type	Area (%)		
		1992 year	2000year	2012 year
FAO	Forest	4.42 (%)	4.36 (%)	4.31 (%)
	Cropland	2.47 (%)	2.68 (%)	3.13 (%)
RS	Forest	6.44(%)	7.29(%)	6.87(%)
	Cropland	1.82 (%)	2.65 (%)	2.82 (%)

From table 5.4, comparing with method of FAO and Remote Sensing, it can be seen there is around 2.5% difference in forest. As for cropland, there is relative a small difference which is 0.65% in 1992, 0.03% in 2000 and 0.31% in 2012. Although there are some differences between the results obtained by two methods, but from year of 1992 to 2000 to 2012, the trend is substantially consistent especially for cropland. Therefore, it is indicated that the result of land cover change obtained by remote sensing in this study is reasonable and can be verified.

5.5 Anomaly detection

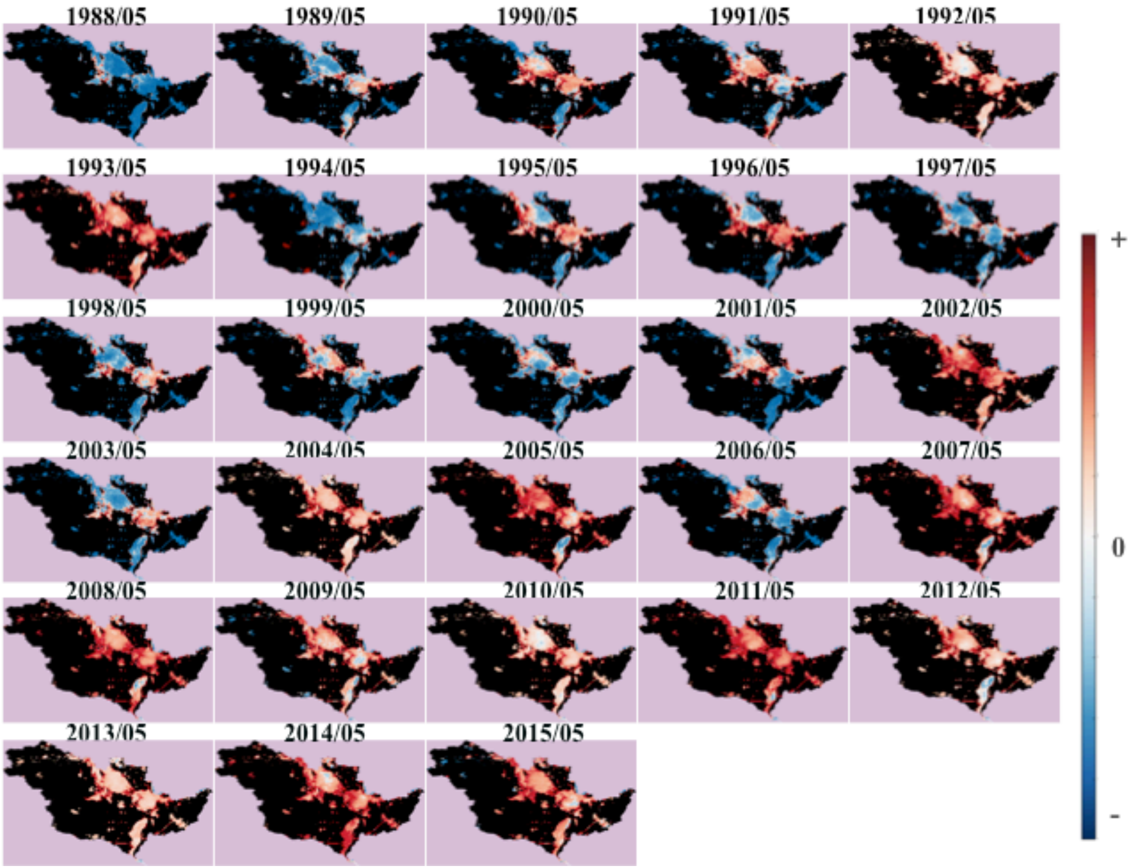

Figure 5.14 LSWC anomaly for Mississippi basin from 1988 to 2015

Figure 5.14 is the anomaly image of Mississippi basin in May from 1988 to 2015. Red color represents a positive difference, blue color represents for negative difference. According to this map, we can visually find in which year there is some anomaly.

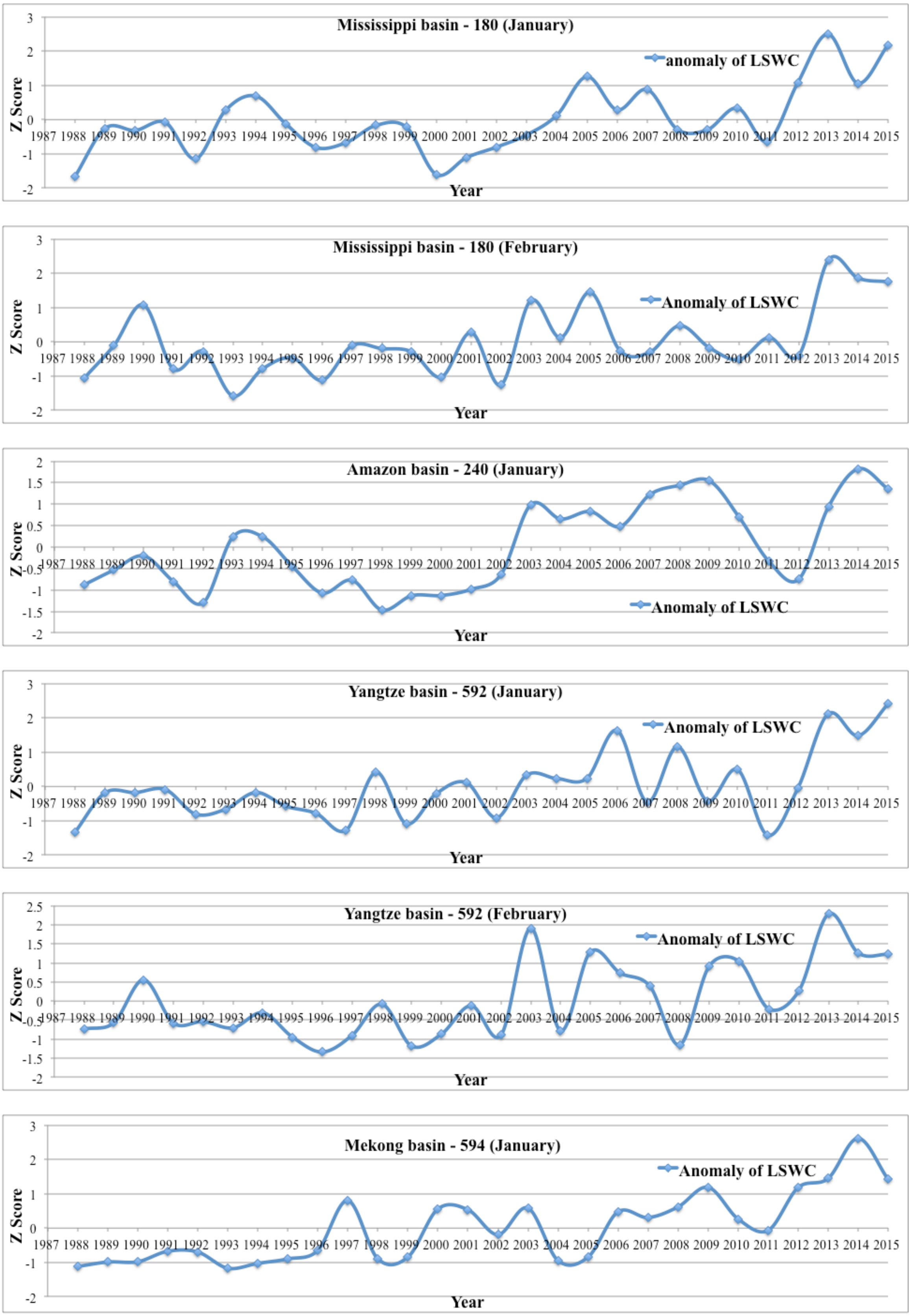

Figure 5.15 LSWC anomaly in each month during 1987-2015 in each basin

Then, we calculated the z-score of LSWC and counted the anomaly in each month since 1987 to 2015 for each river basin as shown in Figure 5.15.

1988

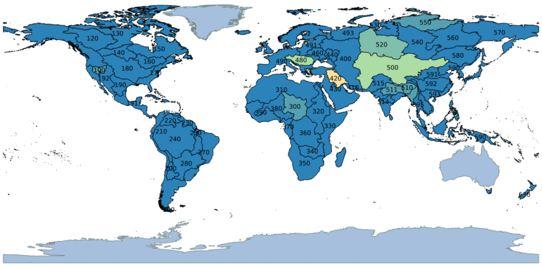

1989

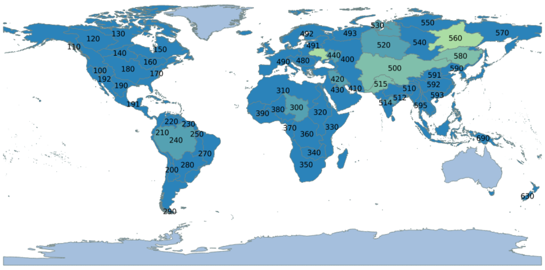

1990

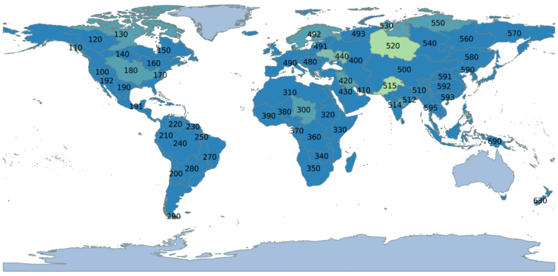

1991

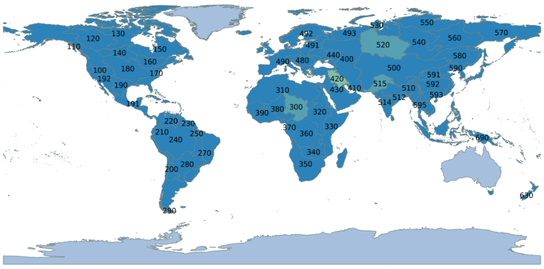

1992

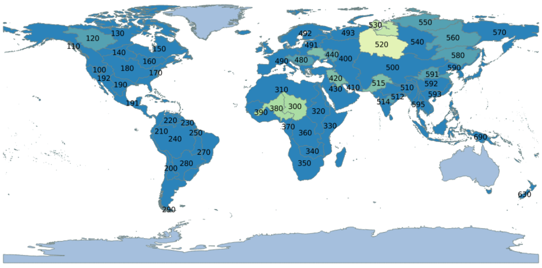

1993

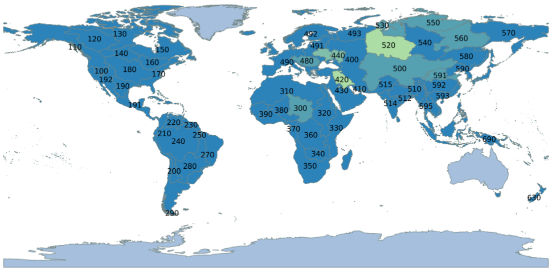

1994

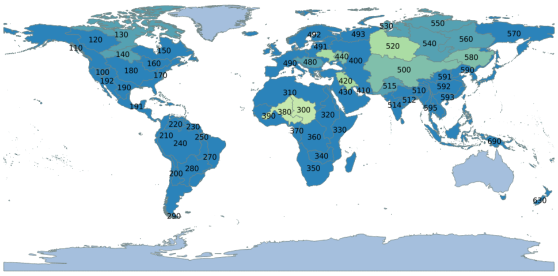

1995

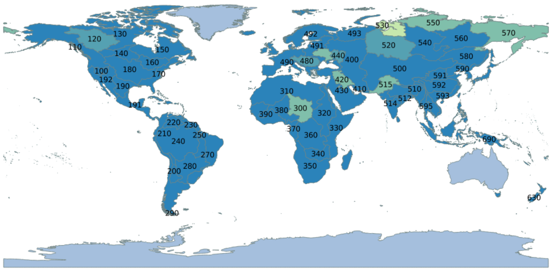

1996

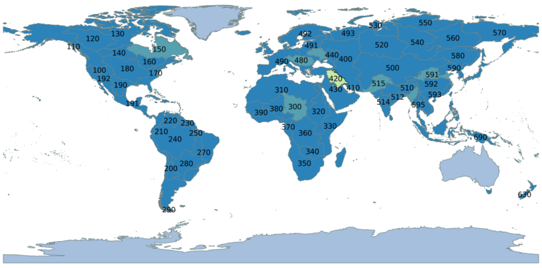

1997

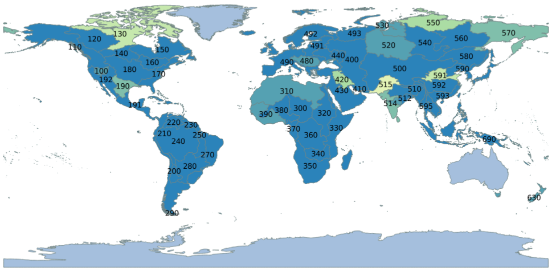

1998

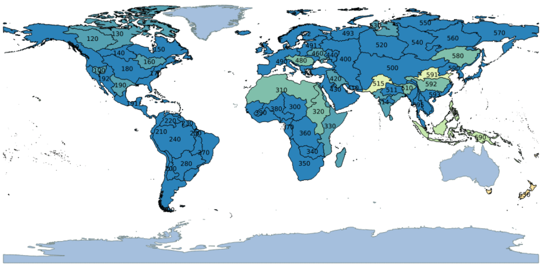

1999

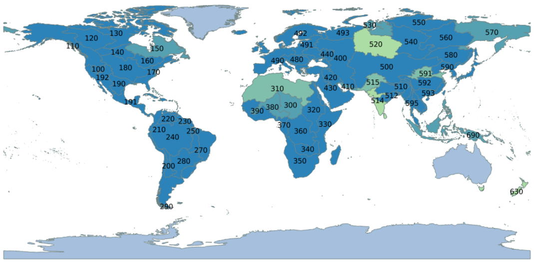

2000

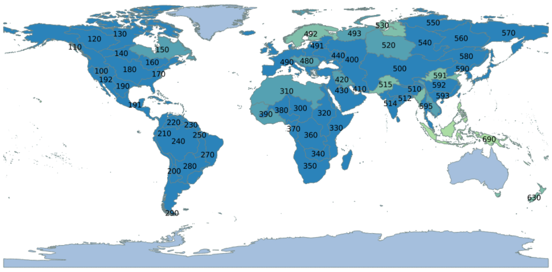

2001

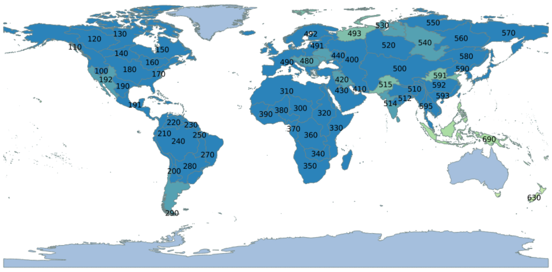

2002

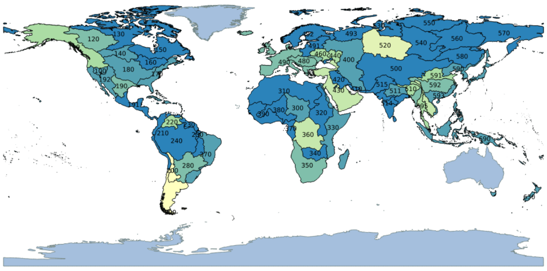

2003

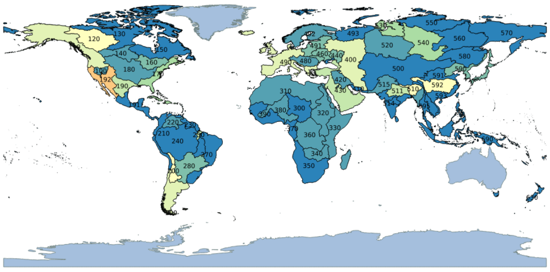

2004

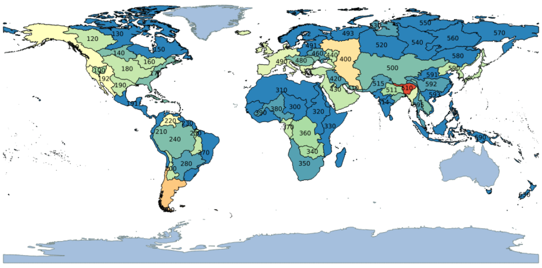

2005

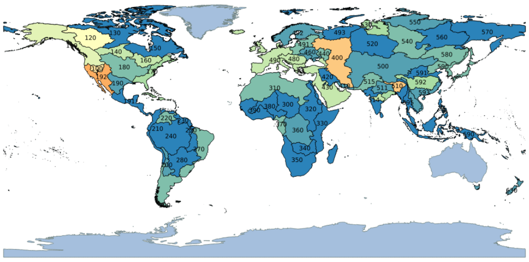

2006

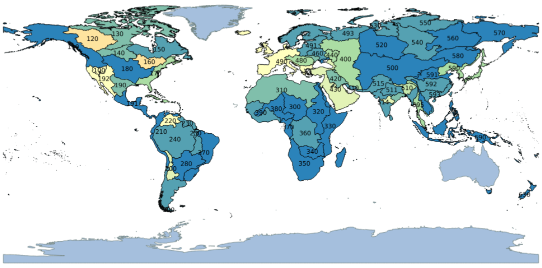

2007

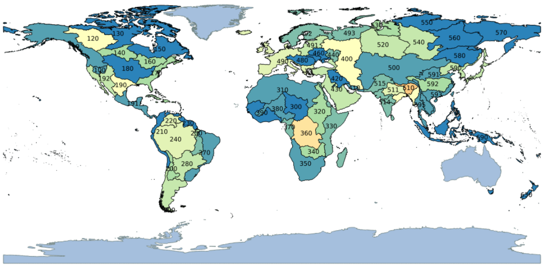

2008

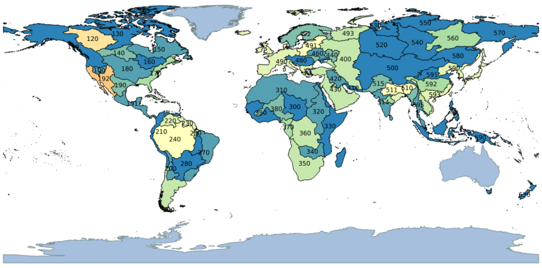

2009

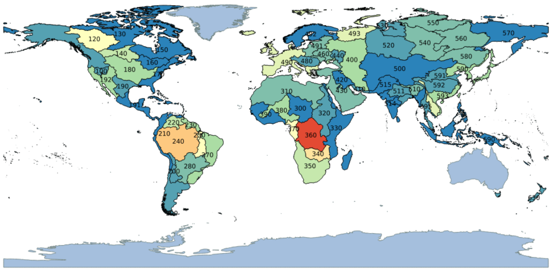

2010

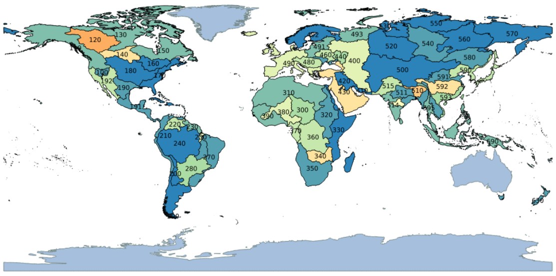

2011

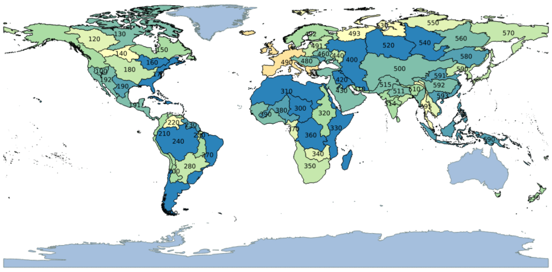

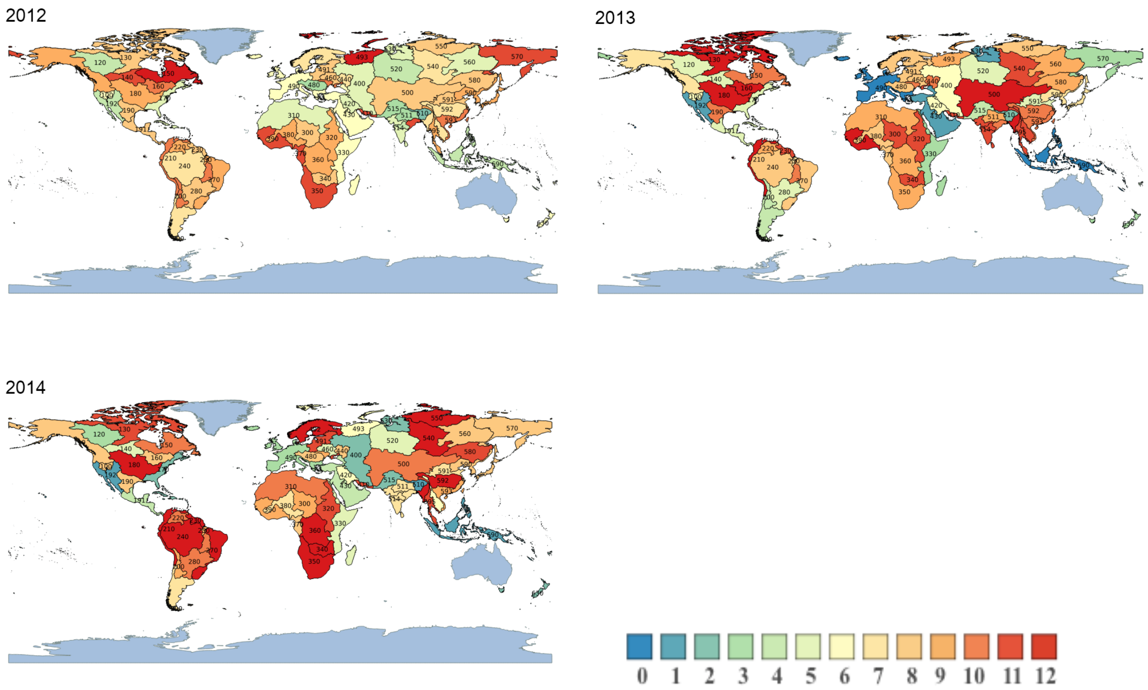

Figure 5.16 The monthly flooding development during last 30 years in global scale.

Combining anomaly of 12 months, we made anomaly map for each year and got the monthly flooding development during nearly last 30 years in global scale. From Figure 5.16, it showed a growth trend of anomaly on frequency especially since last 15 years. And a significantly rise could be found in nearly five years, the potential floods can be detected.

5.6 Discussion and Conclusion

In this part, firstly, by comparing precipitation monthly change with LSWC daily change of each river basin, we found that LSWC pattern basically coincide with rainfall pattern, showing a seasonal variation characteristic in each year. Secondly, by conducting STL method, it can be found their seasonal trend was similar however there was no significant correlation between long-term trend in LSWC and precipitation. Rainfall was indicated not the only factor that brings about the change in LSWC. Thirdly, it was found that the change in urban was very strong in Yangtze basin, from 2000 to 2012, changed from 0.08% to 0.83%. Moreover, the proportion of cropland increased significantly, especially Ganges basin increased by 41.35%, grew to nearly 70%. In addition the trend of consistent growth was showed both by cropland and LSWC. It is expected that the widespread expansion of cropland may bring about LSWC increasing. What's more, by comparing with statistic data of land cover change obtained by FAO, it is indicated that the result of land cover change obtained by remote sensing in this study is reasonable and can be verified. Furthermore, by detecting the anomaly of LSWC, the potential floods can be detected, which showed a monthly growth trend on frequency especially since last 15 years.

Chapter6. Conclusions and future work

6.1 Conclusions

This research using long term of nearly 30 years LSWC database the probability and trend of land surface water coverage on global scale were estimated which could help us understand historical tendency of land surface water coverage in each river basin.

Firstly, the investigated incidence angle effect to the backscattering for PALSAR. The change of incidence angle brought backscattering variation in PALSAR ScanSAR images. The standard deviation of σ0 (dB) against incidence angle in two scenes is 0.36 and 0.56, smaller than 1dB, within the acceptable range of PALSAR in this study. Moreover, based on interval estimation and Otsu's method, (μ+3σ0) (dB) was defined as the inundated threshold to map LSWC distribution of PALSAR in this study. In addition, the calibration function was established to show a good relationship between NDFI, NDPI of AMSR-E and LSWC derived from PALSAR, which all the R2 was more than 0.80. Besides, since the NDPI was calculated by brightness temperature with bigger frequency-36.5GHz, which can lead to a stronger penetration, NDPI more likely to be affected by surface roughness. NDFI showed a better performance than NDPI on land surface water coverage estimation. What's more, for the mechanism of PALSAR is backscattering whereas the mechanism of AMSR-E is brightness temperature although they are belong to the same microwave remote sensing. A slight underestimation in inundated area was found for the surface conditions and vegetation would influence backscattering of PALSAR. However, because of relative low spatial resolution of AMSR-E, a slight overestimation was found in inundated area. Finally, by comparing with optical remote sensing, it showed the advantage and superiority of microwave remote sensing in this study.

Secondly, taking into account population density of the world 68 major river basins all over the world were delineated using Hydro 1k dataset. The long term of nearly 30 years global LSWC database was built by passive microwave radiometers of SSMI, AMSR-E, WindSAR and AMSR2. we mapped LSWC derived from SSMI, AMSR-E, WindSAR, AMSR2 and conducted cross calibration between SSMI LSWC and AMSR-E LSWC, AMSR-E LSWC and WindSAT LSWC, WindSAT LSWC and AMSR2 LSWC in the alternate process of sensors. By conducting temporal analysis with cross-calibrated LSWC database, it was found that the LSWC value of nearly 15 years is greater than the value of nearly 30 years. It is indicated a growth trend in LSWC during last 30 years. From wetland, forest, agriculture, to barren land, with the increase of aridity, the probability with high LSWC in one year decreases. Finally, global probability distribution function (PDF) and global cumulative distribution function (CDF) was created by integrating 30 years of LSWC database.

Thirdly, the monthly precipitation change and daily LSWC change from 1987 to 2015of all river basins worldwide was computed. Based on the annual least squares fitting, the trend of LSWC in each river basin was computed. In all 68 basins, almost unchanged river basin just accounted for only 18%, most of them showed obvious growth trend. Declining trend basin accounted for 2.9%, essentially unchanged basin accounted for 20.6%, the growth trend basin accounted for 76.5%. Moreover, by comparing precipitation change with LSWC change of each river basin, LSWC pattern basically coincide with rainfall pattern, showing a seasonal variation characteristic in each year. However after carrying out STL time series analysis between precipitation and LSWC, it was found that the seasonal trend between each other was very close but the long-term trend of them was not similar, LSWC almost presented increasing trend whereas precipitation had no significant trend. The correlation coefficients were small, smaller than 0.50. Therefore, rainfall was indicated not the only factor that brings about the change in LSWC.

Additionally, by calculating 4 kinds of land cover change including cropland, forest, urban and water body in each river basin, it was found that the change in urban area was very strong in many river basin, especially in Yangtze basin and Huang he basin in China, from 2000 to 2012, changed from 0.08% to 0.83% and from 0.17% to 2.21%. Due to global warming, the Himalayan snowmelt increased year by year, causing water in Brahmaputra-river increased significantly. Besides, there is no clear trend feature in forest cover change. In addition, the proportion of cropland increased significantly, especially Ganges basin increased by 41.35%, grew to nearly 70%. Meanwhile, the cropland presented consistent growth situation along with LSWC. The correlation coefficients between cropland and LSWC change was more than 0.85. It is expected that the widespread expansion of cropland might bring about LSWC increasing. What's more, by comparing with statistic data of land cover change obtained by FAO, it is indicated that the result of land cover change obtained by remote sensing in this study is reasonable and can be verified. Furthermore, by detecting the anomaly of LSWC, the potential floods can be detected, which showed a monthly growth trend on frequency especially since last 15 years.

Consequently, this research demonstrated the advantages of microwave remote sensing, which indicates that they are in trade off relationship according to different research purpose. We can combine different remote sensing data to compensate each other. Moreover, this research covered a global range and provided macroscopic understanding and grasp of global land surface water coverage development based on daily long-term historical database and was expected to explain popular and significant phenomenon such as global warming, glacial melting, cropland use change, urban expansion.

6.2 Future work

Uncertainties and limitations still remain in this study. Major river basins were derived and analyzed. But there are a lot of small watersheds in these large basins, which would lead to uncertainties. Besides, we utilized three different land cover change datasets. As we known, different datasets got from different sensors and calculated by different methodology based on classification scheme. The inevitable variation existed among them, which could affect result of land cover change. What's more, since active microwave remote sensing PALSAR will be influenced by land surface roughness, passive microwave remote sensing will be influenced great by soil moisture, soil type and vegetation would also influence for land surface water condition in different place. In addition, since the research area is global in this study, different place has its own condition. Complex factors as population, social economy, policy and so on would bring about uncertainties. It was difficult to formulate a unified standard to adapt to the world.

For my next step, we advance to conduct spatial analysis of land cover change and combine other factors like social economy to discuss their influence on LSWC change. What's more, we try to use other method to choose anomaly threshold and the real flood events statistic data will be utilized to compare with the anomaly detection result. The flooding detection still needs to be analysis. Besides, we will use different data mining methods to distinguish cropland cover change effect. The flooding may also be related to rising populations, rapid urbanization, deforestation and other land-use changes. Separating the climate change signal from the human factors that increase flood risk is a real challenge.

Reference

Alexakis, D.D., Hadjimitsis, D.G., Agapiou, A., Themistocleous, K., Retalis, A., Michaelides, S., Pashiardis, S., Tymvios, F., 2012. Flood mapping of Yialias River catchment area in Cyprus using ALOS PALSAR radar images. Proc. SPIE - Int. Soc. Opt. Eng. 8531, 85310S. doi:10.1117/12.974581

Anh, T.T., Dinh, D.N., 2008. Flood Monitoring Using ALOS / PALSAR Imagery Flood Monitoring Using ALOS / PALSAR Imagery 19–22.

Apurv, T., Mehrotra, R., Sharma, A., Goyal, M.K., Dutta, S., 2015. Impact of climate change on floods in the Brahmaputra basin using CMIP5 decadal predictions. J. Hydrol. 527, 281–291. doi:10.1016/j.jhydrol.2015.04.056

Arnesen, A.S., Silva, T.S.F., Hess, L.L., Novo, E.M.L.M., Rudorff, C.M., Chapman, B.D., McDonald, K.C., 2013. Monitoring flood extent in the lower Amazon River floodplain using ALOS/PALSAR ScanSAR images. Remote Sens. Environ. 130, 51–61. doi:10.1016/j.rse.2012.10.035

Bai, Y., Feng, M., Jiang, H., Wang, J., Zhu, Y., Liu, Y., 2014. Assessing consistency of five global land cover data sets in China. Remote Sens. 6, 8739–8759. doi:10.3390/rs6098739

Bhattacharyya, A. 1943. “On a measure of divergence between two statistical populations defined by their probability distributions”. Bulletin of the Calcutta Mathematical Society 35, 99–109

Bartholome, E., Belward, A.S., 2005. GLC2000: A new approach to global land cover mapping from Earth observation data. Int. J. Remote Sens. 26, 1959−1977. doi:10.1080/01431160412331291297

Cayan, D.R., Maurer, E.P., Dettinger, M.D., Tyree, M., Hayhoe, K., 2008. Climate change scenarios for the California region. Clim. Change 87. doi:10.1007/s10584-007-9377-6

Chowdary, V.M.; Vinu Chandran, R.; Neeti, N.; Bothale, R.V.; Srivastava, Y.K.; Ingle, P.; Ramakrishnan, D.; Dutta, D.; Jeyaram, A.; Sharma, J.R.; et al. 2008. Assessment of surface and sub-surface waterlogged areas in irrigation command areas of Bihar state using remote sensing and GIS. Agr. Water Manag. 95,754–766

Chakraborty, R., Rahmoune, R., Ferrazzoli, P., 2011. Use of passive microwave signatures to detect and monitor flooding events in Sundarban Delta, in: 2011 IEEE International Geoscience and Remote Sensing Symposium. IEEE, pp. 3066–3069. doi:10.1109/IGARSS.2011.6049865

Cleveland, R.B., Cleveland, W.S., McRae, J.E., Terpenning, I., 1990. STL: A seasonal-trend decomposition procedure based on loess. J. Off. Stat. doi:citeulike-article-id:1435502

Chang HT, Wang SF, Vadeboncoeur MA and Lin TC (2014) Relating vegetation dynamics to temperature and precipitation at monthly and annual timescales in Taiwan using MODIS 128 vegetation indices. International journal of Remote Sensing 35(2): 598–620

Damien O'Grady, et al., 2014.The use of radar satellite data from multiple incidence angles improves surface water mapping. Remote Sensing of Environment 140, pp.652–664

Daniel, Z. and Stephen, K., 2010. CRC Standard Probability and Statistics Tables and Formulae. CRC Press. p. 49. ISBN 978-1-58488-059-2.

Das, T., Maurer, E.P., Pierce, D.W., Dettinger, M.D., Cayan, D.R., 2013. Increases in flood magnitudes in California under warming climates. J. Hydrol. 501, 101–110. doi:10.1016/j.jhydrol.2013.07.042

Deichmann, U., Balk, D., Yetman, G., 2001. Transforming Population Data for Interdisciplinary Usages : From census to grid 20pp.

Evans, T.L., Costa, M., Telmer, K., Silva, T.S.F., 2010. Using ALOS/PALSAR and RADARSAT-2 to Map Land Cover and Seasonal Inundation in the Brazilian Pantanal. IEEE J. Sel. Top. Appl. Earth Obs. Remote Sens. 3, 560–575. doi:10.1109/JSTARS.2010.2089042

Environmental Protection Agency (EPA). 2005.Wetland Mapping and Classification Methodology—Overall Framework—A Method to Provide Baseline Mapping and Classification for Wetlands in Queensland, Version 1.2; Queensland Government: Brisbane, QLD, Australia

Ferrazzoli, P., Rahmoune, R., Moccia, F., Grings, F., Salvia, M., Barber, M., Douna, V., Karszenbaum, H., Soldano, A., Goniadzki, D., Parmuchi, G., Montenegro, C., Kandus, P., Borro, M., 2010. The effect of rain and flooding events on AMSR-E signatures of la plata basin, argentina. IEEE J. Sel. Top. Appl. Earth Obs. Remote Sens. 3, 81–90. doi:10.1109/JSTARS.2010.2040584

Friedl, M.., McIver, D.., Hodges, J.C.., Zhang, X.., Muchoney, D., Strahler, a. ., Woodcock, C.., Gopal, S., Schneider, a, Cooper, a, Baccini, a, Gao, F., Schaaf, C., 2002. Global land cover mapping from MODIS: algorithms and early results. Remote Sens. Environ. 83, 287–302. doi:10.1016/S0034-4257(02)00078-0

Gizaw, M.S., Gan, T.Y., 2016. Regional Flood Frequency Analysis using Support Vector Regression under historical and future climate. J. Hydrol. 538, 387–398. doi:10.1016/j.jhydrol.2016.04.041

Hallegatte, S., Green, C., Nicholls, R.J., Corfee-Morlot, J., 2013. Future flood losses in major coastal cities. Nat. Clim. Chang. 3, 802–806. doi:10.1038/nclimate1979

Hoan, N.T., Tateishi, R., Alsaaideh, B., Ngigi, T., Alimuddin, I., Johnson, B., 2013. Tropical forest mapping using a combination of optical and microwave data of ALOS. Int. J. Remote Sens. 34, 139–153. doi:10.1080/01431161.2012.709329

Huang, G., Kadir, T., Chung, F., 2012. Hydrological response to climate warming: The Upper Feather River Watershed. J. Hydrol. 426-427, 138–150. doi:10.1016/j.jhydrol.2012.01.034

Hulme, M., 1992. A 1951-80 global land precipitation climatology for the evaluation of general circulation models. Clim. Dyn. 7, 57–72. doi:10.1007/BF00209609

Hulme, M., Osborn, T.J., Johns, T.C., 1998. Precipitation sensitivity to global warming: Comparison of observations with HadCM2 simulations. Geophys. Res. Lett. 25, 3379. doi:10.1029/98GL02562

Ishitsuka, N., 2006. Using Synthetic Aperture Radar (SAR) to Measure the Area of Rice Cultivation. Agricultural environment technology institute report, 24, pp. 95-151

Imaoka, K., Kachi, M., Kasahara, M., Ito, N., Nakagawa, K., Oki, T., 2010. Instrument Performance and Calibration of Amsr-E and Amsr2. Int. Arch. Photogramm. Remote Sens. Spat. Inf. Sci. 38, 1–4.

Juan Pablo Ardila Lopez, 2008. Assessment and modeling of angular backscattering variation in ALOS ScanSAR images over tropical forest areas. International institute for geo-information science and earth observation enschede, the netherlands

Jacquin A, Sheeren D and Lacombe JP (2010) Vegetation cover degradation assessment in Madagascar savanna based on trend analysis of MODIS NDVI time series. International Journal of Applied Earth Observation and

Geoinformation 12S: S3–S10

Kleinen, T., Petschel-Held, G., 2007. Integrated assessment of changes in flooding probabilities due to climate change. Clim. Change 81, 283–312. doi:10.1007/s10584-006-9159-6

Liao, P.S., Chen, T.S., Chung, P.C., 2001. A fast algorithm for multilevel thresholding. J. Inf. Sci. Eng. 17, 713–727.

Loveland, T.R., Reed, B.C., Brown, J.F., Ohlen, D.O., Zhu, Z., Yang, L., Merchant, J.W., 2000. Development of a global land cover characteristics database and IGBP DISCover from 1 km AVHRR data. Int. J. Remote Sens. 21, 1303–1330. doi:10.1080/014311600210191

Lucas, R., Armston, J., Fairfax, R., Fensham, R., Accad, A., Carreiras, J., Kelley, J., Bunting, P., Clewley, D., Bray, S., Metcalfe, D., Dwyer, J., Bowen, M., Eyre, T., Laidlaw, M., Shimada, M., 2010. An evaluation of the ALOS PALSAR L-band backscatter - Above ground biomass relationship Queensland, Australia: Impacts of surface moisture condition and vegetation structure. IEEE J. Sel. Top. Appl. Earth Obs. Remote Sens. 3, 576–593. doi:10.1109/JSTARS.2010.2086436

LI X and Takeuchi W 2015 Estimation of land surface water coverage with PALSAR and AMSR-E for flood detection on global scale The International Symposium on Remote Sensing (IRSR), Tainan, Taiwan

LI X and Takeuchi W 2015 Development of large scale flooding detection method by integrating historical global record using AMSR-E/AMSR2 with PALSAR IEEE IGARSS, Milan, Italy. 822–5

LI X and Takeuchi W 2015 Global flood detection and spatio-temporal analysis from 2002-2015 The 36th Asian Conference of Remote Sensing (ACRS), Manila, Philippines

Murray, N.J.; Phinn, S.R.; Clemens, R.S.; Roelfsema, C.M.; Fuller, R.A. 2012. Continental scale mapping of tidal flats across East Asia using the Landsat archive. Remote Sens. 4, 3417–3426

Madsen, H., Lawrence, D., Lang, M., Martinkova, M., Kjeldsen, T.R., 2014. Review of trend analysis and climate change projections of extreme precipitation and floods in Europe. J. Hydrol. 519, 3634–3650. doi:10.1016/j.jhydrol.2014.11.003

Mahmoud, S.H., Alazba, A.A., 2015. Hydrological response to land cover changes and human activities in arid regions using a geographic information system and remote sensing. PLoS One 10, 1–19. doi:10.1371/journal.pone.0125805

Mallakpour, I., Villarini, G., 2015. The changing nature of flooding across the central United States. Nat. Clim. Chang. 5, 250–254. doi:10.1038/nclimate2516

Mcfeeters, S.K., 2013. Using the Normalized Difference Water Index (NDWI) within a Geographic Information System to Detect Swimming Pools for Mosquito Abatement: A Practical Approach 3544–3561. doi:10.3390/rs5073544

Milly, P.C.D., Wetherald, R.T., Dunne, K. a, Delworth, T.L., 2002. Increasing risk of great floods in a changing climate. Nature 415, 514–517. doi:10.1038/415514a

Mishra, P., Singh, D., Yamaguchi, Y., Singh, D., 2011. Land Cover Classification of Palsar Images By Knowledge Based Decision Tree Classi- Fier and Supervised Classifiers Based on Sar Observables. Prog. Electromagn. Res. B 30, 47–70. doi:10.2528/PIERB11011405

Mori, S., Takeuchi, W. and S.H., 2009. Estimation of land surface water coverage (LSWC) with AMSR-E and MODIS, in: 2nd Joint Student Seminar on Civil Infrastructures, AIT. Thailand.

Njoku, E.G., Chan, S.K., 2006. Vegetation and surface roughness effects on AMSR-E land observations. Remote Sens. Environ. 100, 190–199. doi:10.1016/j.rse.2005.10.017

Njoku, E.G., Jackson, T.J., Lakshmi, V., Chan, T.K., Nghiem, S. V., 2003. Soil moisture retrieval from AMSR-E. IEEE Trans. Geosci. Remote Sens. 41, 215–228. doi:10.1109/TGRS.2002.808243

PALSAR Reference Guide, 6th Edition. November 2012. Japan Space Systems (J-space-systems)

Pfafstetter O, 1989, "Classification of hydrographic basins: coding methodology", unpublished manuscript, DNOS, Rio de Janeiro; translated by J.P. Verdin, U.S. Bureau of Reclamation, Brasilia, Brazil, September 5, 1991.

Ohana-Levi, N., Karnieli, A., Egozi, R., Givati, A., Peeters, A., 2015. Modeling the Effects of Land-Cover Change on Rainfall-Runoff Relationships in a Semiarid, Eastern Mediterranean Watershed. Adv. Meteorol. 16. doi:10.1155/2015/838070

Pall, P., Aina, T., Stone, D. a, Stott, P. a, Nozawa, T., Hilberts, A.G.J., Lohmann, D., Allen, M.R., 2011. Anthropogenic greenhouse gas contribution to flood risk in England and Wales in autumn 2000. Nature 470, 382–385. doi:10.1038/nature09762

Paloscia, S., Macelloni, G., Santi, E., 2006. Soil moisture estimates from AMSR-E brightness temperatures by using a dual-frequency algorithm. IEEE Trans. Geosci. Remote Sens. 44, 3135–3144. doi:10.1109/TGRS.2006.881714

Panahi, A., Alijani, B., Mohammadi, H., 2010. The Effect of the Land Use/Cover Changes on the Floods of the Madarsu Basin of Northeastern Iran. J. Water Resour. Prot. 2, 373–379. doi:10.4236/jwarp.2010.24043

Panigrahy, S.; Murthy, T.V.R.; Patel, J.G.; Singh, T.S. 2012. Wetlands of India: Inventory and assessment at 1:50,000 scale using geospatial techniques. Curr. Sci. 102, 852–856

Pearson, K. 1895. "Contributions to the Mathematical Theory of Evolution. II. Skew Variation in Homogeneous Material". Philosophical Transactions of the Royal Society A: Mathematical, Physical and Engineering Sciences 186, 343–414

Reis, D.S., Stedinger, J.R., 2005. Bayesian MCMC flood frequency analysis with historical information. J. Hydrol. 313, 97–116. doi:10.1016/j.jhydrol.2005.02.028

Rosenqvist, A., Shimada,M. and Watanabe, M., 2004. ALOS PALSAR: Technical outline and mission concepts. 4th International Symposium on Retrieval of Bio- and Geophysical Parameters from SAR Data for Land ApplicationsInnsbruck, Austria, pp.16-19

Shiroto, N., Tada, T. and Ouchi, K, 2010. Estimating spatial distribution of oceanic waves using polarimetric synthetic aperture radar. Coastal Engineering, Vol. 66,No.1, pp.1416-1420

Shimada, M., Isoguchi, O., Tadono, T. and Isono, K., 2009. PALSAR Radiometric and Geometric Calibration. IEEE TRANSACTIONS ON GEOSCIENCE AND REMOTE SENSING, VOL. 47, NO. 12, pp.3915-3932

Savary, S., Rousseau, A.N., Quilbé, R., 2009. Assessing the effects of historical land cover changes on runoff and low flows using remote sensing and hydrological modeling. J. Hydrol. Eng. 14, 575–587. doi:10.1061/(ASCE)HE.1943-5584.0000024

Schmocker-Fackel, P., Naef, F., 2010. More frequent flooding? Changes in flood frequency in Switzerland since 1850. J. Hydrol. 381, 1–8.

doi:10.1016/j.jhydrol.2009.09.022

Sezgin, M., Sankur, B., 2004. Survey over image thresholding techniques and quantitative performance evaluation. J. Electron. Imaging 13, 146. doi:10.1117/1.1631315

Singh, Y., Ferrazzoli, P., Rahmoune, R., 2013. Flood monitoring using microwave passive remote sensing (AMSR-E) in part of the Brahmaputra basin, India. Int. J. Remote Sens. 34, 4967–4985. doi:10.1080/01431161.2013.786194

Sippel, S.J., Hamilton, S.K., Melack, J.M., Choudhury, B.J., 1994. Determination of inundation area in the Amazon River floodplain using the SMMR 37 GHz polarization difference. Remote Sens. Environ. 48, 70–76. doi:10.1016/0034-4257(94)90115-5

Sippel, S.J., Hamilton, S.K., Melack, J.M., Novo, E.M.M., 1998. Passive microwave observations of inundation area and the area / stage relation in the Amazon River floodplain. Int. J. Remote Sens. 19, 3055–3074. doi:10.1080/014311698214181

Slayback, D.A., Brakenridge, G.R., Policelli, S., Tokay, M.M., Keiner, A., n.d. Near Real ‐ Time Global Satellite Monitoring of Flooding Events 2011 Floods : MoLvaLon Indus.

Song, X.-P., Huang, C., Feng, M., Sexton, J.O., Channan, S., Townshend, J.R., 2014. Integrating global land cover products for improved forest cover characterization: an application in North America. Int. J. Digit. Earth 7, 709–724. doi:10.1080/17538947.2013.856959

Shamsudduha M, Chandler RE, Taylor1 RG and Ahmed KM (2009) Hydrology and Earth System Sciences, 13: 2373–2385

Takeuchi, W., Komori, D., Oki, T. and Yasuoka, Y., 2006. An integrated approach on rice paddy irrigation pattern monitoring over Asia with MODIS and AMSR-E, in: Proceedings of the AGU. San francisco, USA.

Takeuchi, W., Gonzalez, L., 2009. Blending MODIS and AMSR-E to predict daily land surface water coverage, in: ISRS.

Temimi, M., Lacava, T., Lakhankar, T., Tramutoli, V., Ghedira, H., Ata, R., Khanbilvardi, R., 2011. A multi-temporal analysis of AMSR-E data for flood and discharge monitoring during the 2008 flood in Iowa. Hydrol. Process. 25, 2623–2634. doi:10.1002/hyp.8020

Temimi, M., Leconte, R., Brissette, F., Chaouch, N., 2007. Flood and soil wetness monitoring over the Mackenzie River Basin using AMSR-E 37 GHz brightness temperature. J. Hydrol. 333, 317–328. doi:10.1016/j.jhydrol.2006.09.002

Tobler, W., Deichmann, U., Gottsegen, J., Maloy, K., 1997. World population in a grid of spherical quadrilaterals. Int. J. Popul. Geogr. 3, 203–25. doi:10.1002/(SICI)1099-1220(199709)3:3<203::AID-IJPG68>3.0.CO;2-C

Toonen, W.H.J., 2015. Flood frequency analysis and discussion of non-stationarity of the Lower Rhine flooding regime (AD 1350-2011): Using discharge data, water level measurements, and historical records. J. Hydrol. 528, 490–502. doi:10.1016/j.jhydrol.2015.06.014

US Geological Survey (USGS) and US Department of the Interior. Normalized Difference Water Index (NDWI). Available online: http://deltas.usgs.gov/fm/data/data_ndwi.aspx (accessed on 3 May 2013)

Watts, J.D., Kimball, J.S., Jones, L.A., Schroeder, R., McDonald, K.C., 2012. Satellite Microwave remote sensing of contrasting surface water inundation changes within the Arctic-Boreal Region. Remote Sens. Environ. 127, 223–236. doi:10.1016/j.rse.2012.09.003

Zhang, G., Chen, S., Liao, J., 2011. Otsu image segmentation algorithm based on morphology and wavelet transformation, in: 2011 3rd International Conference on Computer Research and Development. IEEE, Shanghai, pp. 279–283. doi:10.1109/ICCRD.2011.5764020

Zhang, N., Tateishi, R., 2013. Integrated Use of Existing Global Land Cover Datasets for Producing a New Global Land Cover Dataset with a Higher Accuracy : A Case Study in Eurasia. Adv. Remote Sens. 2, 365–372.

Zhang, Y., Wang, C., Wu, J., Qi, J., Salas, W. a., 2014. Mapping paddy rice with multitemporal ALOS/PALSAR imagery in southeast China. Int. J. Remote Sens. 35, 6781–6798. doi:Doi 10.1080/01431161.2014.965282

Zheng, W., Liu, C., Xin, Z., Wang, Z., 2008. Flood and waterlogging monitoring over Huaihe River basin by AMSR-E data analysis. Chinese Geogr. Sci. 18, 262–267. doi:10.1007/s11769-008-0262-7